Electronic quantum transport in two-dimensional nanostructures: methods and applications

Tatiane Pereira dos Santos

Instituto de Física
Universidade Federal Fluminense

December 2018

Electronic quantum transport in two-dimensional nanostructures: methods and applications

Tatiane Pereira dos Santos

Advisor: Dr. Caio H. Lewenkopf

Instituto de Física
Universidade Federal Fluminense

A thesis submitted for the degree of
Doctor of Philosophy

December 2018

Ficha catalográfica automática - SDC/BIF
Gerada com informações fornecidas pelo autor

S237e Santos, Tatiane
Electronic quantum transport in two-dimensional nanostructures : methods and applications / Tatiane Santos ; Caio Lewenkopf, orientador. Niterói, 2018.
123 f. : il.

Tese (doutorado)-Universidade Federal Fluminense, Niterói, 2018.

DOI: http://dx.doi.org/10.22409/PPGF.2018.d.38896774870

1. Transporte eletrônico. 2. Sistemas nanoestruturados. 3. Métodos numéricos em transporte. 4. Sistemas bidimensionais. 5. Produção intelectual. I. Lewenkopf, Caio, orientador. II. Universidade Federal Fluminense. Instituto de Física. III. Título.

CDD -

Bibliotecário responsável: Mario Henrique de Oliveira Castro - CRB7/6155

INSTITUTO DE FÍSICA
Universidade Federal Fluminense
CURSO DE PÓS-GRADUAÇÃO EM FÍSICA
RUA GAL MILTON TAVARES DE SOUZA, SN
24210-346 – NITERÓI - RIO DE JANEIRO
TEL: (21)2629-5878 - FAX: 2629-5887
E-MAIL: cpg@ if.uff.br

Ata dos trabalhos finais da Comissão Examinadora da tese apresentada por **Tatiane Pereira dos Santos**. No vigésimo dia do mês de dezembro de dois mil e dezoito, às quatorze horas, reuniram-se no Instituto de Física da Universidade Federal Fluminense os membros da Comissão Examinadora constituída pelos professores doutores Caio Henrique Lewenkopf – IF/UFF, Andréa Brito Latgé – IF/UFF, Pedro Paulo de Mello Venezuela – IF/UFF, Daiara Fernandes de Faria – UERJ e Dario Andres Bahamon Ardila - Universidade Presbiteriana Mackenzie/SP, sob a presidência do primeiro, para prova pública de apresentação da tese intitulada ***"Electronic quantum transport in two-dimensional nanostructures: methods and applications"***, tendo em vista as exigências do Regulamento Específico do curso de Física relacionadas com a conclusão do Doutorado em Física pela Universidade Federal Fluminense. A tese foi elaborada sob a orientação do professor Caio Henrique Lewenkopf. Após a exposição do trabalho, a aluna respondeu às questões formuladas pelos integrantes da Comissão Examinadora, que apresentou parecer no sentido de aprová-la. Para constar, foi lavrada a presente ata, que vai assinada pelos membros da Comissão Examinadora e pela doutoranda.

Niterói, vinte de dezembro de dois mil e dezoito.

Dr. Caio Henrique Lewenkopf

Dra . Andréa Brito Latgé

Dr. Pedro Paulo de Mello Venezuela

Dra. Daiara Fernandes de Faria

Dr. Dario Andres Bahamon Ardila

Tatiane Pereira dos Santos

Acknowledgements

First of all, I would like to acknowledge my Ph.D. advisor Caio Lewenkopf for his insightful guidance throughout these four years and for all his clear efforts to teach me how to address valuable scientific questions. For presenting me such a roll of exciting and challenging research topics and for being such an example of high-quality research. Lastly, for sharing with me some of his experienced knowledge about academia during our meetings, I am very glad for these unique discussions.

Secondly, my very special gratitude goes to Leandro Lima, whose open-door policy and deep understanding of the research topics approached here have been crucial for the accomplishment of this thesis. Thank you.

Thirdly, I want to dedicate a paragraph more to acknowledge Leandro Lima again. This time, for always making me feel welcome in the workplace, both in the University and in our research group, since the first day of my Ph.D. Also, for being such a friendly and hilarious, and at the same time serious and accurate, mentor for this thesis.

I am also grateful to all the faculty and staff of the Physics Department in UFF, for giving me so many opportunities as a Ph.D. student, which undoubtedly opened the way to much more, even during such a dramatic financial and political period for the country. I am especially indebted to Professors Antonio Zelaquett, Malena Hor-Meyll, Nicim Zagury, and Wagner Tavares Buono for their intellectual support on the Qualification Exam and Professors Andrea Latgé, Pedro Venezuela, Marcos Sergio Figueira da Silva, Daiara Faria and Dario Bahamon for their careful reading of this thesis and professional guidance while part of the Pre-Thesis and Thesis Committee.

I would like to thank all the amazing people that I met in Niterói whose I nurtured admiration. In particular, my office mates Antonio Duarte Pereira, Dácio Souza, Paola Obando, Rodrigo Dias, and Arash Jafarizadeh, and my bandmates of Cat'O'Rama: Thabata Vieira (singer), Carol Velasco (bass) and Breno Dowsley (guitar).

During my stay in Grenoble, my internship advisor, Xavier Waintal was able to make me feel quickly integrated and functional in the group and in the CEA-INAC facilities, which was fundamental for the realization of part of this thesis. Thank you very much for that. I am also indebted to my co-workers, Thomas Kloss, and Benoît Rossignol. I want to thank my

colleagues in the department, Pacôme Armagnat, Stefan Ilic, Shuo Mi, Vincent Talbo and Corentin Bertrand and I could not forget to thank my dear friends in Grenoble, Mariana Alves Henrique, Rayssa Marques, Calink Indiara, Susi Savassa, Carla Polo and Natália Rodrigues, with whose I had extraordinary experiences of companionship while being far from home. Thank you.

I would like to express a sincere gratitude to other current and past members of the Nano research group that contributed to my personal enrichment of academic knowledge: Professors Roberto Bechara Muniz and Antonio Costa, and Bruno Max Melo, Emilia Ridolfi, Rhonald Burgos, Vladimir Miranda, Mariana Odashima, Marcone Sena Jr, Marcio Jorge da Costa, Marcos Moutinho, Jorge Correa, Luis Canonico, Carlos León and Vanessa Torres. It has been a pleasure to be part of this group.

Finally, I would like to thank my family, for supporting my career all this time. Especially, the two most important people of my life, my mother Miriam Pereira, for being my main inspiration, and my beloved partner, Bruno Marques, for standing by my side for anything and for all the obstacles that we overcame together. I also want to thank Bruno's family, that supported me indirectly.

Living these four years in Niterói has been a fantastic and rewarding journey that surely will bring me *saudades* wherever I go. Thank you!

This work was supported by CAPES, CNPq, and FAPERJ.

Abstract

This thesis studies the quantum transport properties of two-dimensional materials in different settings, both in the stationary and the time-dependent regimes. The presentation is divided into two main parts. The first one is devoted to the DC quantum transport, the stationary transport theory in the linear response regime. To this end, we provide a discussion about a numerical method for the efficient calculation of the stationary quantum transport properties of scattering systems in tight-binding representation. We present a self-contained description of the wave function matching (WFM) method to calculate electronic quantum transport properties of nanostructures using the Landauer-Büttiker approach. We demonstrate that the number of operations involved in computing the system conductance scales linearly with the number of sites of the system of interest, $\mathscr{O}(N)$. It also scales linearly with the number of conducting channels. We discuss two applications.

The first one is the study the effect of ripples on the weak-localization effect in the magnetoconductance of disordered graphene samples. We investigate two different types of disorder in graphene, namely, ripples and scalar random Gaussian disorder. The former has been predicted to originate random pseudomagnetic fields, which are expected to affect the phase coherence and the momentum relaxation times in conductivity measurements. The latter critically affects the sign of quantum correction to the conductivity at low external magnetic fields, making the magnetoconductivity crossover from the weak-localization to the anti-weak-localization regime, as a function of the disorder correlation length. We numerically demonstrate that ripples are responsible for the suppression of the weak-localization correction term as a result of the random pseudomagnetic field. We also analyze the in-plane deformations in graphene lattice considering the interaction with a substrate and the inclusion of in-plane magnetic field. These effects can be used as a probe for the underlying sources of disorder.

Our second application of the stationary WFM method is the investigation of the magnetotransport properties of disordered graphene samples in the quantum Hall (QH) regime. We study the effects of the disorder on the transition states between Hall plateaus, especially regarding scaling properties, which have not been addressed in graphene systems yet. Such transition states have been intensively studied in the context of two-dimensional electron

gases and found to exhibit universal scaling behavior. However, the situation is less clear in graphene, which displays an anomalous quantum Hall effect as a consequence of the valley degeneracy. To this end, we discuss how intervalley and intravalley scattering processes, modeled by different configurations of disorder, affect the QH transition states in graphene.

The second part of this thesis is devoted to a time-dependent study of the transport theory. We extend the WFM formalism of the first part of the thesis to the time-domain and discuss the inclusion of a time-dependent perturbation. Afterward, we present a review of a time-dependent method in the tight-binding approximation under the influence of a time-dependent drive. We introduce local operators under this regime as probes of transient effects. As an application to such formalism, we propose the model of a collider between two interacting electronic voltage pulses. The pulse is generated of electronic states of quasi-one-dimensional wires that function as guides to a perpendicular collision. We discuss the possibility of focusing the pulse trajectory using DC studies. Next, we include Coulomb interactions in the time-dependent Hartree-Fock approximation. When we compare the local quantities variations due to a relative time-delay between the pulses, we observe that the current deviation is maximal away from the synchronized collision.

Resumo

A presente tese aborda propriedades de transporte eletrônico quântico em materiais bidimensionais sob diferentes configurações, tanto nos regimes estacionário quanto dependente do tempo. A apresentação do conteúdo desta tese é dividida em duas partes principais. A primeira parte dedica-se ao transporte quântico em correntes DC no regime de resposta linear. Para este fim, apresentamos uma discussão sobre um método numericamente eficiente para o cálculo das propriedades de transporte em sistemas de espalhamento na representação *tight-binding*. Usando o formalismo de Landauer-Büttiker, descrevemos de forma auto-contida, o método da Correspondência de Função de Onda (*Wave Function Matching* - WFM), o qual permite calcular propriedades de transporte em nanoestruturas. Em seguida, demonstramos que o número de operações numéricas envolvidas na computação da condutância escala linearmente com o número de sítios discretos do sistema de interesse, $\mathscr{O}(N)$ e linearmente com o número de canais de condução, para um modelo realístico de uma nanoestrutura. Ainda na primeira parte desta tese, discutimos duas aplicações.

A primeira aplicação consiste no estudo do efeito de corrugações na localização fraca demonstrada através da magnetocondutância em amostras de grafeno desordenado. Para tanto, investigamos dois tipos diferentes de desordem: quiral e escalar. Sabe-se que o primeiro tipo é responsável por gerar campos pseudomagnéticos aleatórios, os quais devem afetar a coerência de fase e os tempos de relaxação de momento no sistema. O segundo tipo de desorder afeta criticamente o sinal da correção quântica na condutividade para campos magnéticos externos baixos, fazendo com que a magnetocondutividade transite entre a localização fraca e anti localização fraca, em função do comprimento de correlação das deformações. Demonsramos numericamente que as deformaccões em nanofitas de grafeno são responsáveis pela supressão do termo de correção de localização fraca como resultado da presença do campo pseudomagnético aleatório. Também analisamos as deformações que ocorrem paralelamente ao plano do grafeno de duas formas: considerando a interação da nanofita com um substrato e com a inclusão de um campo magnético paralelo. O total destes efeitos pode ser usado como uma fonte de medição das características dos possíveis tipos de desordem subjacentes.

Quanto à segunda aplicação do método WFM estacionério, investigamos as propriedades de magnetotransporte em amostras de grafeno desordenadas sob regime Hall quântico (*Quantum Hall* - QH). Estudamos o efeito da desordem em estados na região de transição entre plateaus Hall, especialmente quanto as propriedades de escala. Tais estados de transição são bem conhecidos no contexto de gases de elétrons bidimensionais e tem demonstrado um comportamento universal. Contudo, em grafeno, o qual exibe um efeito Hall quântico anômalo como conseqüência da degeneração de vale, os estados de transiçãção ainda não foram abordados. Portanto, discutimos como os processos de espalhamento inter-vales e intra-vales, modelados pelas diferentes configurações de desordem, afetam os estados de transição entre plateaus Hall no grafeno.

A segunda parte desta tese é dedicada ao estudo da teoria de transporte dependente do tempo. Para isso, estendemos o formalismo WFM, discutido na primeira parte da presente tese, para o domínio temporal, donde incluímos uma perturbação dependente do tempo. Em seguida, apresentamos uma revisão de um método dependente do tempo na aproximação *tight-binding* sob a influência de uma perturbação externa dependente do tempo. Introduzimos então operadores locais que funcionam como sondas de efeitos transitórios. Como aplicação a tal formalismo, propomos o modelo de um colisor de pulsos eletrônicos de tensão em regime interagente. O pulso é gerado por estados eletrônicos projetados em estados de fios quase unidimensionais, os quais funcionam como guias para uma colisão perpendicular. Usando estudos com correntes DC, discutimos possíveis configurações estacionárias as quais permitem criar um potencial focalizador de pulsos. Por último, incluímos interações Coulombianas utilizando a aproximação de Hartree-Fock dependente do tempo. Comparando as colisões em função de um atraso relativo entre a emissão dos pulsos, observamos que o desvio de corrente por interação de Coulomb é máximal fora da situação sincronizada.

FRAGILIDADE

"Este verso, apenas um arabesco
em torno do elemento essencial – inatingível.
Fogem nuvens de verão, passam aves, navios, ondas,
e teu rosto é quase um espelho onde brinca o incerto movimento,
ai! já brincou, e tudo se fez imóvel, quantidades e quantidades
de sono se depositam sobre a terra esfacelada.
Não mais o desejo de explicar, e múltiplas palavras em feixe
subindo, e o espírito que escolhe, o olho que visita, a música
feita de depurações e depurações, a delicada modelagem
de um cristal de mil suspiros límpidos e frígidos: não mais
que um arabesco, apenas um arabesco
abraça as coisas, sem reduzí-las."

– Carlos Drummond de Andrade, A Rosa do Povo.

Table of contents

List of figures

Chapter 1

Introduction

Advances in the fabrication of high-quality samples at the micro and nanoscale paved the way for the discovery of fascinating transport properties. In particular, the synthesis of new two-dimensional materials, such as graphene[1], phosphorene[2], transition metal dichalcogenides[3], among others has revealed a plethora of new phenomena that could offer interesting theoretical challenges[4–7]. As a consequence, the demand for numerical studies that realistically describe and provide insight on such systems on an atomistic/microscopic basis has dramatically increased.

1.1 The numerical approaches for large-scale transport problems

|

To have a computational method that comprises systems as general as possible, one can resort to a discrete representation. Typically, the most used discretization scheme in quantum transport theory is the tight-binding representation, which can describe either finite difference grids[8] or atomistic basis[9]. In any case, the tight-binding Hamiltonian usually yields a sparse matrix. Therefore, one may benefit from this fact by reducing unnecessary products with large blocks of zeros.

In this sense, one method - which is based on the Landauer-Büttiker formalism - that stands out is the Recursive Green's Function (RGF). The RGF method consists in cutting the system into slices and calculating the unperturbed Green's function of each slice. Then, a fully perturbed Green's function of the system is calculated from a recursive scheme based on the Dysons series. This method can reduce the sparsity of the linear problem and can

even support multiple probes - especially if one applies a strategical slicing scheme [10]. The RGF method has a simple implementation and has been used by numerous groups.

An alternative approach to the RGF is the Wave Function Matching (WFM) method. It is based on the matching of the wave-function of the scattering region with the system's boundary conditions. Both methods, RGF and WFM, have been successfully used to study the transport properties of large-scale systems [11, 12, 10, 13]. Moreover, it can be shown that they are equivalent to each other through the Fisher-Lee relations [14, 15]. For the WFM method, the way in which the matching conditions are built may prohibit the system to be sliced on the same fashion as the RGF method. Here we discuss an efficient implementation of the WFM method where this limitation is overcome, making the method easily applied to systems at the micron scale.

Several groups have put an enormous effort to provide computational frameworks that efficiently implements one or more of these methods[16–19, 19–35]. A particular implementation of the WFM method is coded in the Kwant package[21]. The package is boosted by the MUMPS libraries, a forefront package for sparse linear algebra[36] and that Kwant outperforms a C implementation of the RGF method in one order of magnitude, regarding the system size. In addition to the conductance, the Kwant package also has several tools to compute transport quantities such as conductance, local density, local current, shot noise, band structure, and so on. It is developed under a user-friendly platform coded in Python and has a cutting-edge scheme to handle general-shaped scattering regions, multiple orbitals and multiprobes[37].

Later on, an extension to the Kwant package to the time-domain has been joined[38]. Motivated by the recent advances in experimental techniques in electron dynamic devices, a set of numerical methods for the time-dependent transport theory has been developed by the group headed by Prof. Xavier Waintal [39–43]. It comprises in a framework time-dependent perturbations in the scattering problem in tight-binding approximation, ranging from propagating voltage pulses to AC current perturbations, and has been successfully applied to several problems up to the present[44–46, 43]. More recently, inside the T-Kwant package, a dedicated suit to the manybody physics has been developed[47] that handles electronic interactions in the time-dependent Hartree-Fock approximation[48]. Due to efficient implementation techniques, the method presents a linear scaling in time[44], which is also a novelty to the field. Together, Kwant and T-Kwant, they represent the state-of-the-art techniques for transport problems under the scattering formalism of the tight-binding approach. Understanding and applying such set of cutting-edge tools to interesting problems in condensed matter physics constitutes the main motivation behind this whole thesis.

1.2 Outline of this thesis

This thesis can be outlined as follows:

- **Chapter 2**: An investigation of the wave-function matching method, implemented in the Kwant package;
- **Chapter 3**: The effects of impurities and ripples on the weak-localization correction in the magnetoconductance in graphene;
- **Chapter 4**: The effects of disorder and temperature to the quantum phase transitions in graphene in the quantum Hall regime;
- **Chapter 5**: The time-dependent extension of the wave function matching formalism and its relation to the nonequilibrium Green's function formalism, and a review of the T-Kwant techniques;
- **Chapter 6**: A proposal for a plasmon-plasmon collider in 2DEG devices to study Coulomb interactions.
- **Chapter 7**: Summary of the results of this thesis and final remarks.

Part I

DC quantum transport

Chapter 2

Numerical methods for the calculation of DC electronic transport

In this chapter, we critically analyze the Wave Function Matching (WFM) method [21, 49, 13], whose numerical implementations allow to efficiently compute the quantum transport properties of electrons in nanostructures, modeling realistic sample sizes and non-trivial geometries.

Quantum electronic transport in mesoscopic systems is usually described by the Landauer-Büttiker approach [8], that gives a simple relation between the conductance and the quantum transmission coefficients of a single-particle scattering problem. In other words, the problem is reduced to solving a Schrödinger equation for an open quantum system. Here, we show in this chapter that the WFM method is one of the most efficient numerical tools for this task. The latter introduces a partition between a central or scattering region ("conductor") and the asymptotic one ("leads" or terminals) and, by matching the corresponding wave function at the partition boundaries, gives the system scattering matrix S [50].

Alternatively, transport properties in mesoscopic systems can be calculated using non-equilibrium Green's function (NEGF) techniques [8], the standard tools that has been used in our group. This formalism is widely used due to its successful combination with Density Function Theory [51, 20, 52, 17, 23, 30, 32]. At the single-particle level, NEGF is equivalent to the Landauer-Büttiker approach (see, for instance, Ref. [15]). The standard method to compute transport properties in large systems using NEGF is the Recursive Green's Function (RGF) method [53, 54, 10]. The latter takes advantage of the sparsity of the system Hamiltonian to partition the scattering region into conveniently chosen small domains [55, 56]. The corresponding Green's functions are recursively combined using the Dyson equation to obtain matrix elements of the full system Green's function that are relevant for

transport calculations. The RGF method is robust, accurate, has a simple implementation, and has been widely used [57, 58, 11, 18, 59, 12, 60].

A recent open source implementation of the WFM method, the Kwant package [21], has significantly increased its usage. Kwant is developed under a user-friendly platform coded in Python and handles general-shaped scattering regions, multiple orbitals, and multi-probes [37]. Furthermore, extensions to the Kwant package can be easily joined [38]. Kwant also explores the sparsity of the system Hamiltonian by using the MUMPS libraries, a forefront package for sparse linear algebra [36]. Ref. [21] shows that Kwant significantly outperforms the RGF method in a wide range of applications.

We show that the number of operations required by the WFM method to compute the conductance of a given system is much smaller than previously claimed [21]. To explain this finding, we first give a self-contained presentation of the method – whose documentation is scattered and scarce – critically analyzing its main features. Next, we numerically study a number of systems to corroborate our analytical findings.

This chapter is organized as follows: In Sec. 2.1 we provide a short review of the relation between quantum transport and the scattering theory. Next, we adapt the theory for the tight-binding approximation and cast the scattering problem as the solution of a linear system. In Sec. 2.2 we describe the WFM method and discuss its computational cost. In Sec. 2.3 we benchmark the WFM method comparing its CPU time, memory usage and precision with a standard RGF implementation.

2.1 Theoretical background

The WFM method is suited to calculate the scattering properties of a system with arbitrary geometry and dimension $d = 1, 2$, or 3. It is aimed to describe the non-interacting on-shell scattering processes in mesoscopic samples or crystalline structures coupled to multiple terminals.

Figure 2.1 illustrates a generic multi-terminal two-dimensional $(d = 2)$ system. A central scattering region is coupled to electrodes represented by semi-infinite leads labeled by $\alpha = 1, \cdots, \Lambda$, where incoming and outgoing electrons propagate coherently. Due to the transverse confinement, the leads states are quantized in open modes (scattering channels) labeled by $n = 1, \ldots, N_\alpha$. The index n labels both the transverse modes and the electron spin projection. The mesoscopic sample corresponds to the central or scattering region, while the leads are associated to the asymptotic domain.

Let us describe the system single-particle Hamiltonian by a tight-binding model. This approximation is suited to model both an atomistic system represented by a linear combination

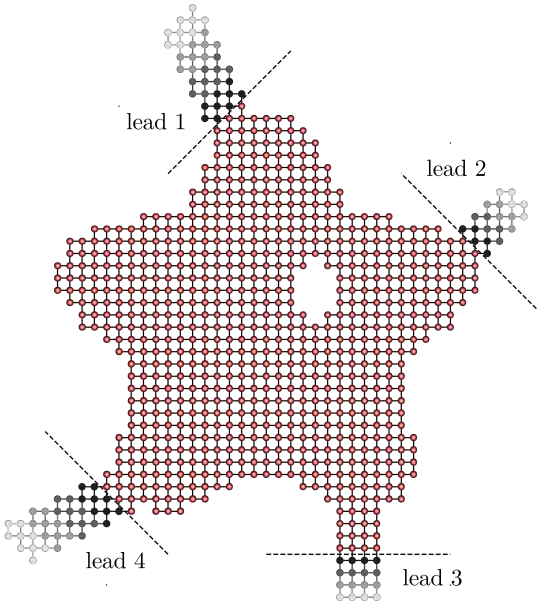

Fig. 2.1 Illustration of a generic multi-terminal two-dimensional system. The dashed lines indicate the partition between the scattering and the asymptotic regions. The latter is modelled by or semi-infinite periodic lattices.

of atomic orbitals and a continuous system in a finite element representation [8]. The system Hamiltonian is written as

$$H = \sum_{j,j'} H_{j,j'} |j\rangle\langle j'|, \tag{2.1}$$

where the index $j = (\boldsymbol{r}_i, \sigma)$ labels both the position in the lattice and the internal degrees of freedom σ such as spin, atomic orbital, etc., of the state $|j\rangle$.

2.1.1 Quantum transport and scattering theory

The Schrödinger equation of the scattering system reads

$$H \left|\Psi_m^{\pm}(E)\right\rangle = E \left|\Psi_m^{\pm}(E)\right\rangle, \tag{2.2}$$

where $|\Psi_m^{+}(E)\rangle$ ($|\Psi_m^{-}(E)\rangle$) stands for the outgoing (incoming) scattering state at channel m. Here m labels both α and n. The S-matrix is defined by the scattering amplitudes $\langle\Psi_m^{-}(E)|\Psi_{m'}^{+}(E)\rangle = S_{mm'}(E)\delta(E-E')$.

The scattering matrix S can be formally written in terms of projection operators that decompose the Hilbert space in the partition described by Fig. 2.1 [61]. Let us assume, for instance, normal boundary conditions at the interface $\mathscr{B}$ between the scattering and

asymptotic regions. One defines the projection operator

$$Q = \sum_{\mu} \left|\phi_{\mu}\right\rangle \left\langle\phi_{\mu}\right| \tag{2.3}$$

in terms of the complete set of discrete orthonormal states $\left\langle\phi_{\mu}\middle|\phi_{\mu'}\right\rangle = \delta_{\mu\mu'}$ defined in the scattering (or central) region and obeying the boundary conditions at $\mathscr{B}$. In turn, at the asymptotic region, one defines

$$P = \sum_{m\in\alpha} \int dE \left|\chi_m(E)\right\rangle \left\langle\chi_m(E)\right|, \tag{2.4}$$

where $|\chi_m(E)\rangle$ form a complete set of continuous orthogonal states, $\langle\chi_m(E)|\chi_{m'}(E')\rangle = \delta_{mm'}\delta(E-E')$, defined in the asymptotic (or leads) region. Since the asymptotic region is not compact, the projection operator P is continuous. By construction, P and Q span the system Hilbert space and, hence, $P+Q=1$.

The system Hamiltonian is conveniently decomposed into three pieces

$$H = H_{PP} + H_{QQ} + (H_{PQ} + H_{QP}), \tag{2.5}$$

where we introduced the notation $AHB = H_{AB}$ [1].

The projection operators allow one to write Eq. (2.2) as a Lippmann-Schwinger equation, namely

$$P\left|\Psi_m^{\pm}(E)\right\rangle = \left|\chi_m(E)\right\rangle + \frac{1}{E^{\pm} - H_{PP}} H_{QQ} Q \left|\Psi_m^{\pm}(E)\right\rangle \tag{2.6}$$

$$Q\left|\Psi_m^{\pm}(E)\right\rangle = \frac{1}{E^{\pm} - H_{QQ}} H_{QP} P \left|\Psi_m^{\pm}(E)\right\rangle, \tag{2.7}$$

where $E^{\pm} = E \pm i\eta$, with η an infinitesimal positive number. After some algebra, one writes the S-matrix as [61, 50]

$$S_{mm'}(E) = \delta_{mm'} - 2i\pi\rho_m^{1/2}(E) \sum_{\mu\mu'} [H_{PQ}]_{m\mu} \left[\frac{1}{E - H_{QQ} - \Sigma^{+}(E)}\right]_{\mu\mu'} [H_{QP}]_{\mu' m'} \rho_{m'}^{1/2}(E), \tag{2.8}$$

where $\Sigma^{\pm}(E) = H_{QP}(E^{\pm} - H_{PP})^{-1} H_{PQ}$ is the embedding self-energy, which accounts for coupling the to the continuum and describes the resonance processes, while $\rho_m(E)$ stands for the electronic density of states at the channel m. Here we explicitly neglect direct tunneling

[1] It is convenient to use as the channel basis in the asymptotic region the eigenfunctions of H_{PP}, namely, $H_{PP}\left|\chi_m(E)\right\rangle = E\left|\chi_m(E)\right\rangle$ with normal boundary conditions at $\mathscr{B}$.

processes between different electrodes [61, 50]. This approximation is accurate provided the central region is sufficiently large to prevent direct tunneling processes across the system. This condition is true for most mesoscopic systems, except for small molecular junctions (for more details, see, for instance, Ref. [62]).

The Landauer-Büttiker theory [8] relates the linear conductance of an electronic sample to the transmission probability as

$$\mathscr{G}_{\alpha\beta} = \frac{e^2}{h}\int_{-\infty}^{\infty} dE \left(-\frac{\partial f}{\partial E}\right) T_{\alpha\beta}(E), \tag{2.9}$$

where $f(E) = \left[1 + e^{(E-\mu)/kT}\right]^{-1}$ is the Fermi-Dirac distribution with μ and T giving the equilibrium chemical potential and temperature of the reservoirs [2] . The transmission $T_{\alpha\beta}(E)$ is given by

$$T_{\alpha\beta}(E) = \sum_{\substack{n\in\alpha \\ m\in\beta}} |S_{nm}(E)|^2, \tag{2.10}$$

where $S_{nm}(E)$ is given by Eq. (2.8). The WFM method also gives local properties such as local currents and the local density of states (LDOS), as discussed in Sec. 2.3.

2.1.2 The scattering problem in tight-binding approximation

Let us now write the system Hamiltonian in a suitable form to implement the WFM method. For the sake of simplicity, we discuss in detail the two-terminal case and, at the end, we generalize the results to the multi-terminal case.

Let us consider a mesoscopic system attached to semi-infinite leads, $\alpha = R, L$, as illustrated by Fig. 2.2a. Following the partition operators presented in the previous section, we introduce the standard matrix representation: (i) $H_{QQ} \leftrightarrow H_S$ for the scattering region Hamiltonian; (ii) $H_{PP} \leftrightarrow H_L + H_R$, for the leads Hamiltonian; (iii) $H_{QP} \leftrightarrow V_{SL} + V_{SR}$, for the coupling term connecting the mesoscopic system to the leads.

The full Hamiltonian is written in a block matrix form as

$$H = \begin{pmatrix} H_L & V_{LS} & 0 \\ V_{SL} & H_S & V_{SR} \\ 0 & V_{RS} & H_R \end{pmatrix}. \tag{2.11}$$

[2] In general, the reservoirs have different chemical potentials and temperatures, thus, $f_\alpha(E) = [1 + e^{(E-\mu_\alpha)/kT_\alpha}]^{-1}$. For simplicity we take all temperatures equal to T and since we restrict ourselves to linear response, the small differences between μ_α and the equilibrium μ lead to Eq. (2.9).

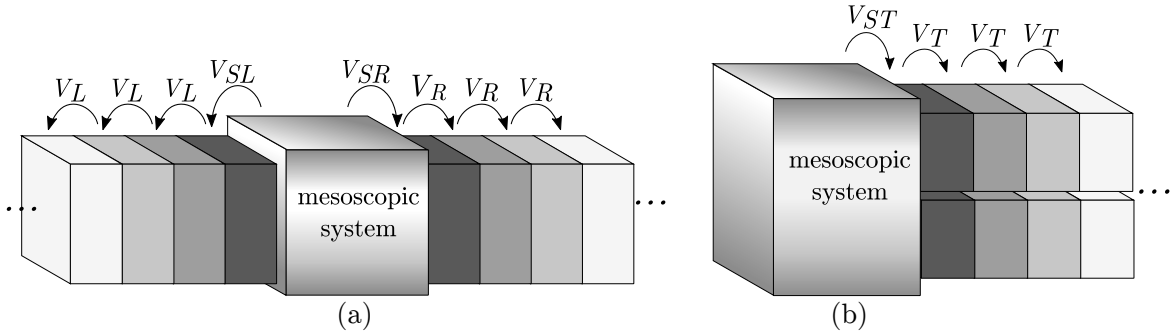

Fig. 2.2 (a) Sketch of a mesoscopic system (S) coupled to Left (L) and Right (R) semi-infinite leads with periodic lattice structure. (b) Equivalent system with the L and R terminal (in general, $\alpha = 1, \cdots \Lambda$) mapped into a single-lead.

H_L and H_R can be written in the block-diagonal structure

$$H_L = \begin{pmatrix} \ddots & \ddots & & \\ \ddots & H_l & V_l & \\ & V_l^\dagger & H_l & V_l \\ & & V_l^\dagger & H_l \end{pmatrix} \qquad H_R = \begin{pmatrix} H_r & V_r^\dagger & & \\ V_r & H_r & V_r^\dagger & \\ & V_r & H_r & \ddots \\ & & \ddots & \ddots \end{pmatrix}, \tag{2.12}$$

where $H_{l(r)}$ stands for suitable $L(R)$-lead unit cell Hamiltonian of dimension $M_{L(R)}$ (represented by boxes in Fig. 2.2). $V_{l(r)}$ are the hopping matrices between nearest-neighboring unit-cells and the unwritten matrix elements are identically zero.

It is advantageous to use the structure of the leads matrices H_L and H_R to group them into an effective single-lead with disjoint sections. The rearranged layout is depicted in Fig. 2.2b. The modified H reads

$$H = \left(\begin{array}{c|cc|cc} H_S - E & V_{SL}^\dagger & V_{SR}^\dagger & & \\ \hline V_{SL} & H_l - E & 0 & V_l^\dagger & 0 \\ V_{SR} & 0 & H_r - E & 0 & V_r^\dagger \\ \hline & V_l & 0 & H_l - E & 0 \\ & 0 & V_r & 0 & H_r - E \\ & & & & \end{array}\right) \begin{matrix} \\ \\ \\ \\ \ddots \\ \ddots \end{matrix} \begin{matrix} \\ \\ \\ \\ \ddots \\ \ddots \end{matrix}. \tag{2.13}$$

The effective lead, hereafter denoted by T, compacts the eigenvalue problem to a single semi-infinite partition, namely

$$\begin{pmatrix} H_S - E & V_{TS}^\dagger & & \\ V_{TS} & H_T - E & V_T^\dagger & \\ & V_T & H_T - E & \ddots \\ & & \ddots & \ddots \end{pmatrix} \begin{pmatrix} \psi_S \\ \psi_0 \\ \psi_1 \\ \vdots \end{pmatrix} = \begin{pmatrix} 0 \\ 0 \\ 0 \\ \vdots \end{pmatrix}, \tag{2.14}$$

where ψ_S corresponds to the scattering wave function at the central region and ψ_n, to the lead wave function at the n-th slice, with $n = 0,0,2,\ldots$ (see Fig. 2.2). The generalization to a multi-terminal setup is straightforward. In this case, H_T accounts for all H_α, with $\alpha = 1,\ldots,\Lambda$ and has dimension $M_T = \sum_{\alpha=1}^{\Lambda} M_\alpha$.

2.2 The wave function matching method

Let us now solve Eq. (2.14). For that purpose we introduce the eigenmode basis ϕ_n:

$$V_T\phi_{n-1} + (H_T - E)\phi_n + V_T^\dagger\phi_{n+1} = 0, \tag{2.15}$$

which corresponds to rows of Eq. (2.14) far from the scattering region. Due to translational symmetry, one can use Bloch's theorem to conveniently write ϕ_n as

$$\phi_n = \chi\lambda^n, \tag{2.16}$$

where χ is the lead unit cell eigenfunction (independent of n) and λ is a complex constant. Hence,

$$V_T\chi + (H_T - E)\chi\lambda + V_T^\dagger\chi\lambda^2 = 0. \tag{2.17}$$

The standard procedure to solve this quadratic eigenvalue problem (QEP) in λ is to introduce an auxiliary vector

$$\chi' \equiv \lambda^{-1}V_T\chi \tag{2.18}$$

and to linearize Eq. (2.17)[63] as

$$\begin{pmatrix} H_T - E & \hat{1} \\ V_T & \hat{0} \end{pmatrix} \begin{pmatrix} \chi \\ \chi' \end{pmatrix} = \lambda \begin{pmatrix} -V_T^\dagger & \hat{0} \\ \hat{0} & \hat{1} \end{pmatrix} \begin{pmatrix} \chi \\ \chi' \end{pmatrix}. \tag{2.19}$$

The advantage of casting Eq. (2.17) as a Generalized eigenvalue problem (GEP) is that one can calculate the eigenvalue λ, which is associated to the crystal momentum k (using $\lambda = e^{ika_\alpha}$, where a_α is the α-lead lattice constant), and the eigenvector χ as a function of the electronic energy E. The QEP is translated into a linear problem at the expense of doubling the equation dimension. Hence, the number of eigenvalues is twice the rank M_T of the matrices V_T and H_T.

One can solve the GEP in Eq. (2.19) by means of well-known numerical algorithms [63–66]. Given an electronic energy E, we calculate the eigenvectors (χ_p, χ'_p) and the corresponding eigenvalues λ_p, where $p = 1, \cdots, 2M_T$.

We can infer from the scattering problem that the $2M_T$ solutions correspond to M_T incoming modes and M_T outgoing modes, as depicted in Fig. 2.3. Since the terminals are uncoupled, the eigenstate χ_p has a block structure

$$\chi_p = \left(\cdots, 0, \chi_p^\alpha, 0, \cdots\right), \tag{2.20}$$

where each block χ_p^α describes the eigenstate of the α-lead with eigenvalue λ_p for $p = 1, \cdots, M_\alpha$ and $\alpha = 1, \cdots, \Lambda$.

The modes can be propagating $|\lambda_p| = 1$ or evanescent $|\lambda_p| < 1$ ($|\lambda_p| > 1$ gives a non-physical behavior). The probability current for the p-th propagating mode reads [67]

$$j_p = -\frac{2}{\hbar}\mathrm{Im}\left(\lambda_p \chi_p^\dagger V_T \chi_p\right). \tag{2.21}$$

The incoming modes correspond to $j_p > 0$ and the outgoing ones to $j_p < 0$. We label those two sets of solutions as $\lambda_p^\pm, \chi_p^\pm$ for $p = 1, \ldots, N_P$, where $\pm$ indicates the corresponding current direction and $N_P \leq M_T$ is the number of incoming/outgoing propagating channels at the electronic energy E. See Fig. 2.3. Since we are interested in transmission coefficients, we restrict ourselves to the analysis of the propagating modes. The evanescent modes ($j_p = 0$) can be treated straightforwardly as a generalization of this method.

Using the sets $\chi_p^\pm$ as basis, we write the wave functions ψ_n as

$$\psi_n = \sum_{q=1}^{N_P} A_q^- \chi_q^- (\lambda_q^-)^n + \sum_{p=1}^{N_P} A_p^+ \chi_p^+ (\lambda_p^+)^n, \tag{2.22}$$

where $n = 0, 1, \cdots$, and $A_p^\pm$ are unknown amplitudes.

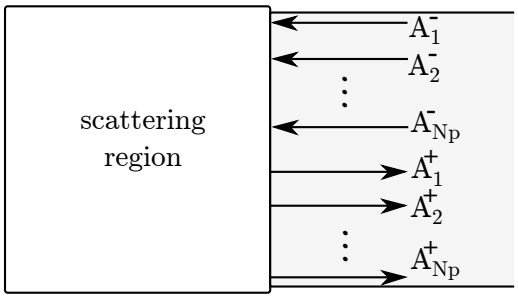

Fig. 2.3 Multi-mode representation of the scattering process of a single-lead with $M_T = \sum_{\alpha=1}^{\Lambda} M_\alpha$ modes. The sign $-$ $(+)$ indicates incoming (outgoing) modes with amplitude A_p^- (A_p^+), where $p = 1, 2, \cdots, N_P$.

One defines the scattering matrix $\tilde{S}$ that relates incoming with outgoing amplitudes as

$$\begin{pmatrix} A_1^+ \\ A_2^+ \\ \vdots \\ A_{N_P}^+ \end{pmatrix} = \tilde{S} \begin{pmatrix} A_1^- \\ A_2^- \\ \vdots \\ A_{N_P}^- \end{pmatrix}. \tag{2.23}$$

Since the eigenchannel basis used by the WFM method is not normalized as the one introduced in Sec. 2.1, the matrix $\tilde{S}$ does not preserve the flux. As we discuss below, S is obtained from $\tilde{S}$ by a simple relation.

To calculate the S-matrix, we consider the scattering process of a single incoming mode q, namely

$$\psi_{nq} = \chi_q^-(\lambda_q^-)^n + \sum_{p=1}^{N_P} \chi_p^+(\lambda_p^+)^n \tilde{S}_{pq}. \tag{2.24}$$

The corresponding S-matrix can be obtained by solving the first two lines of Eq. (2.14)

$$(H_S - E)\psi_{Sq} + V_{TS}^\dagger \psi_{0q} = 0, \tag{2.25}$$

$$V_{TS}\psi_{Sq} + (H_T - E)\psi_{0q} + V_T^\dagger \psi_{1q} = 0, \tag{2.26}$$

where ψ_{Sq} is the scattering region wave function upon injection from mode q. Substituting Eq. (2.24) into Eq. (2.26) and recalling that the basis functions $\chi_p^\pm$ satisfy Eq. (2.17), we find

$$V_{TS}\psi_{Sq} = V_T \psi_{-1q}, \tag{2.27}$$

where ψ_{-1q} is also given by Eq. (2.24). Note, however, that ψ_{-1q} has no physical meaning, since in Eq. (2.14) there is no slice defined for $n=-1$. Here, ψ_{-1q} is an auxiliary mathematical quantity designed to represent the contributions of the terms including ψ_{0q} and ψ_{1q} in Eq. (2.26).

Applying the definition of χ', Eq. (2.18), to each propagating mode as

$$\chi'^{\pm}_{q} = \left(\lambda_q^{\pm}\right)^{-1} V_T \chi_q^{\pm}, \tag{2.28}$$

Eq. (2.27) becomes

$$V_{TS}\psi_{Sq} = \chi'^{-}_{q} + \sum_{p=1}^{N_P} \chi'^{+}_{p}\tilde{S}_{pq} = \chi'^{-}_{q} + \chi'^{+}\tilde{S}_q, \tag{2.29}$$

where $\chi'^{\pm} \equiv (\chi'^{\pm}_1, \chi'^{\pm}_2, \cdots, \chi'^{\pm}_{N_P})$ with dimension $M_T \times N_P$ and $\tilde{S}_q$ is the column q of the S-matrix with dimension $N_P \times 1$. Analogously, using Eq. (2.24) we write ψ_{0q} as

$$\psi_{0q} = \chi_q^{-} + \chi^{+}\tilde{S}_q. \tag{2.30}$$

The linear system composed by Eqs. (2.25) and (2.29) reads

$$\begin{pmatrix} H_S - E & V_{TS}^{\dagger}\chi^{+} \\ V_{TS} & -\chi'^{+} \end{pmatrix} \begin{pmatrix} \psi_{Sq} \\ \tilde{S}_q \end{pmatrix} = \begin{pmatrix} -V_{TS}^{\dagger}\chi_q^{-} \\ \chi'^{-}_{q} \end{pmatrix}. \tag{2.31}$$

Let us now generalize Eq. (2.31) to account for different q-modes

$$\begin{pmatrix} H_S - E & V_{TS}^{\dagger}\chi^{+} \\ V_{TS} & -\chi'^{+} \end{pmatrix} \begin{pmatrix} \psi_{S1} & \psi_{S2} & \cdots & \psi_{SN_P} \\ \tilde{S}_1 & \tilde{S}_2 & \cdots & \tilde{S}_{N_P} \end{pmatrix} = \begin{pmatrix} -V_{TS}^{\dagger}\chi_1^{-} & -V_{TS}^{\dagger}\chi_2^{-} & \cdots & -V_{TS}^{\dagger}\chi_{N_P}^{-} \\ \chi'^{-}_{1} & \chi'^{-}_{2} & \cdots & \chi'^{-}_{N_P} \end{pmatrix}. \tag{2.32}$$

We cast this result into the compact form

$$\begin{pmatrix} H_S - E & V_{TS}^{\dagger}\chi^{+} \\ V_{TS} & -\chi'^{+} \end{pmatrix} \begin{pmatrix} \psi_S \\ \tilde{S} \end{pmatrix} = \begin{pmatrix} -V_{TS}^{\dagger}\chi^{-} \\ \chi'^{-} \end{pmatrix}, \tag{2.33}$$

where $\tilde{S}$ is the full S-matrix and $\psi_S = \begin{pmatrix} \psi_{S1} & \psi_{S2} & \cdots & \psi_{SN_P} \end{pmatrix}$ is the wave function of the scattering region. The S-matrix has dimension $N_P \times N_P$ while ψ_S has dimension $N_S \times N_P$, since it is defined for all the N_S sites in the central region upon injection from all the N_P channels.

Hence, the solution of Eq. (2.33) has a computational cost that depends on the number of propagating channels N_P at the electronic energy E. Due to the sparsity of H_S, we infer that CPU time required to compute a given system conductance scales as $N_S \times N_P$. In Sec. 2.3 we numerically verify that the WMF method indeed follows this prediction.

Note that Eq. (2.33) involves representations in different spaces, while the scattering wave function is given in the tight-binding basis, the S-matrix is expressed in eigenmode basis. The matrices $\chi^{\pm}$ give a connection between theses two basis [68]. For a sufficiently large system, H_S and V_{TS} are sparse matrices making the problem appropriate to the sparse solvers.

2.2.1 Connection to Green's functions

The coupling with leads gives a finite line-width to the resonances in the scattering region via a so-called self-energy. In the non-equilibrium Green's functions formalism (NEGF) (see, for instance, Refs. [8, 62]) the embedding self-energy modifies the scattering region Hamiltonian as $H_S \to H_S + \Sigma$. In what follows we demonstrate that Σ can be calculated from the presented equations.

Let us define the dual space states $\tilde{\chi}_p^{\pm}$, where

$$\left(\tilde{\chi}_p^{\pm}\right)^{\dagger} \chi_{p'}^{\pm} = \delta_{pp'}, \tag{2.34}$$

and identify the first and the second terms on the RHS of Eq. (2.24) with

$$\psi_{nq-} \equiv (\lambda_p^-)^n \chi_q^-, \quad \text{and} \quad \psi_{nq+} \equiv \sum_{p=1}^{N_P} (\lambda_p^+)^n \chi_p^+ \tilde{S}_{pq}. \tag{2.35}$$

Introducing the translation operator $F_{\pm}$ [13]

$$F_{\pm} \psi_{nq\pm} = \psi_{n+1,q\pm}, \tag{2.36}$$

where

$$F_{\pm} \equiv \sum_{p}^{N_P} \lambda_p^{\pm} \chi_p^{\pm} \left(\tilde{\chi}_p^{\pm}\right)^{\dagger}, \tag{2.37}$$

one can write ψ_{0q} and ψ_{1q}, respectively, as

$$\psi_{0q} = \psi_{0q-} + \psi_{0q+}, \tag{2.38}$$

$$\psi_{1q} = F_- \psi_{0q-} + F_+ \psi_{0q+} = (F_- - F_+)\chi_q^- + F_+ \psi_{0q}. \tag{2.39}$$

Substituting Eq. (2.39) into Eq. (2.26) and solving Eq. (2.25) for ψ_{Sq} we find

$$(E - H_S - \Sigma)\psi_{Sq} = Q_q^-, \tag{2.40}$$

where

$$Q_q^- \equiv V_{TS}^\dagger G_T V_T^\dagger (F_- - F_+)\chi_q^- \tag{2.41}$$

is a source term dependent of which channel q is injecting,

$$\Sigma = V_{TS}^\dagger G_T V_{TS} \tag{2.42}$$

is the embedding self-energy, and

$$G_T = \left(E - H_T - V_T^\dagger F_+\right)^{-1} \tag{2.43}$$

is the surface Green's function of the semi-infinite leads. Since Eq. (2.43) involves outgoing states F_+, G_T and Σ correspond to retarded Green's function and self-energy, respectively [8].

We stress that both Σ and G_T are independent of q and contain information about all the propagating modes at the energy E.

Notice that we can solve Eq. (2.40) for ψ_{Sq} as

$$\psi_{Sq} = G_S Q_q^-, \tag{2.44}$$

where G_S is the scattering region Green's function given by

$$G_S \equiv (E - H_S - \Sigma)^{-1}. \tag{2.45}$$

Thus, knowing the full Green's function matrix G_S, we can calculate ψ_{Sq} for any q using Eq. (2.44).

With the help of the dual vector $\tilde{\chi}_p^+$ defined in Eq. (2.34) and the definition of ψ_{0q+} given by Eq. (2.35), we calculate the amplitudes $\tilde{S}_{pq}$ as

$$\tilde{S}_{pq} = \left(\tilde{\chi}_p^+\right)^\dagger \psi_{0q+}. \tag{2.46}$$

The outgoing wave function ψ_{0q+} is a superposition of states χ_p^+ with amplitudes $\tilde{S}_{pq}$. Those states carry a probability current

$$j_{pq} = j_p \left|\tilde{S}_{pq}\right|^2. \tag{2.47}$$

Here j_{pq} depends on the injecting mode q and j_p is given by Eq. (2.21).

The transport coefficients P_{pq} defined as the ratio between the incoming probability current j_q and the outgoing probability current j_{pq} at mode p reads

$$P_{pq} = \frac{j_{pq}}{j_q} = \left|\sqrt{\frac{j_p}{j_q}}\tilde{S}_{pq}\right|^2 = \left|S_{pq}\right|^2, \tag{2.48}$$

where we defined the scattering amplitudes S_{pq} as [8]

$$S_{pq} \equiv \sqrt{\frac{j_p}{j_q}}\tilde{S}_{pq}. \tag{2.49}$$

where S is unitary and conserves the current probability [8].

2.2.2 The generalized Fisher-Lee relation

Let us use the WFM method elements introduced above to derive the relation between the transmission amplitudes as functions of the scattering region Green's functions.

First we write ψ_{0q+} in the RHS of Eq. (2.38) as a function of the scattering region wave function ψ_{Sq} using Eqs. (2.39) and Eq. (2.26), namely

$$\psi_{0q+} = G_T V_{TS} \psi_{Sq} + \left[G_T V_T^\dagger \left(F_- - F_+\right) - 1\right] \chi_q^-. \tag{2.50}$$

Hence, the scattering amplitude $S_{pq} = \sqrt{j_p/j_q}\tilde{S}_{pq}$ reads

$$S_{pq} = \sqrt{\frac{j_p}{j_q}} \left(\tilde{\chi}_p^+\right)^\dagger G_T V_{TS} G_S V_{ST} G_T V_T^\dagger (F_- - F_+) \chi_q^- + \left(\tilde{\chi}_p^+\right)^\dagger \left[G_T V_T^\dagger \left(F_- - F_+\right) - 1\right] \chi_q^-. \tag{2.51}$$

Here we used Eqs. (2.41) and (2.44) to substitute the dependence on ψ_{Sq} by a dependence on the scattering region Green's function G_S.

We assume that the modes q and p belong to different leads α and β, respectively. Due to the block structure of Eq. (2.20) and to the absence of coupling between the leads, the matrices G_T, $V_T^\dagger$ and $(F_- - F_+)$ are block diagonal in the leads subspace. The two-contacts Hamiltonian in Eq. (2.13) illustrates the diagonal block structure of $V_T^\dagger$, for instance. Thus, the second term in Eq. (2.51) identically vanishes.

In this case, the scattering amplitude in Eq. (2.51) becomes

$$t_{pq}^{\beta\alpha} = \sqrt{\frac{j_p}{j_q}} \left(\tilde{\chi}_p^+\right)^\dagger G_T V_{TS} G_S V_{ST} G_T V_T^\dagger (F_- - F_+) \chi_q^-, \tag{2.52}$$

where $t_{pq}^{\beta\alpha}$ is the current-normalized transmission amplitude for the scattering from mode q in the lead α to the mode p in the lead β.

Although one can calculate the transmission coefficients by means of G_S from Eq. (2.52), only few Green's functions matrix elements, such as the elements connecting sites belonging to the interface with the leads, are required to compute the transmission (see, for instance Ref. [10]). Therefore, a simplification of Eq. (2.52) is desirable. For that purpose we use a sub-block division of the scattering region similar to the one used in Ref. [10].

We divide the scattering region into $\Lambda + 1$ blocks, where C is the a central block, which has no connection with the leads, and α represents the α-interface, which is connected to C and only to the lead α, where $\alpha = 1, \cdots, \Lambda$. In this picture, G_S and V_{TS} read

$$G_S = \begin{pmatrix} [G_S]_{CC} & [G_S]_{C1} & \cdots & [G_S]_{C\Lambda} \\ [G_S]_{1C} & [G_S]_{11} & \cdots & [G_S]_{1\Lambda} \\ \vdots & \vdots & & \vdots \\ [G_S]_{\Lambda C} & [G_S]_{\Lambda 1} & \cdots & [G_S]_{\Lambda\Lambda} \end{pmatrix}, \tag{2.53}$$

$$V_{TS} = \begin{pmatrix} 0 & V_{11} & 0 & \cdots & 0 \\ 0 & 0 & V_{22} & \cdots & 0 \\ \vdots & \vdots & \vdots & & \vdots \\ 0 & 0 & 0 & \cdots & V_{\Lambda\Lambda} \end{pmatrix}. \tag{2.54}$$

Since $G_T V_T^\dagger (F_- - F_+)$ is diagonal, where:

$$[G_T]_{\alpha\beta} = \delta_{\alpha\beta} G_\alpha V_\alpha^\dagger \left(F_-^\alpha - F_+^\alpha\right) \tag{2.55}$$

and

$$F_{\pm}^{\alpha} \equiv \sum_{p\in\alpha}^{N_P} \lambda_p^{\pm} \chi_p^{\pm\alpha} \left(\tilde{\chi}_p^{\pm\alpha}\right)^{\dagger}, \tag{2.56}$$

and the states χ_q^- and $\tilde{\chi}_p^+$ have different non-vanishing blocks given by Eq. (2.20), we find

$$t_{pq}^{\beta\alpha} = \sqrt{\frac{j_p}{j_q}} \left(\tilde{\chi}_p^{+\beta}\right)^{\dagger} G_\beta V_{\beta\beta} \left[G_S\right]_{\beta\alpha} V_{\alpha\alpha} G_\alpha V_\alpha^{\dagger} (F_-^\alpha - F_+^\alpha) \chi_q^{-\alpha}, \tag{2.57}$$

which is the generalized Fisher-Lee expression [8].

2.3 A detailed benchmark study of the KWANT package

Let us now demonstrate the efficiency of the sparse solvers associated with the WFM method implemented in the Kwant package. To this end, we compare the processing time and memory usage of the WFM method with the standard RGF approach for a two-dimensional model system as a function of its size and aspect ratio. We conclude this section by discussing an application of the WFM method, namely, the calculation of longitudinal and transverse resistance of a realistic-sized graphene Hall bar.

As mentioned in the introduction, nowadays the RGF method is one of the most standard technique to compute the conductance of nanoscale systems. This method is designed to compute only the system full Green's function matrix elements related to transport properties [8]. For that purpose, the system is divided into partitions. The computational time necessary to calculate the transmission scales with the number of partitions times the cube of the typical number of sites within the partitions.

We recall that Ref. [21] draws conclusions by comparing the performance of the RGF and WFM methods for a square lattice system with $L \times L$ sites as a function of L. The authors [21] find that the CPU time required to compute the conductance using the RGF method scales with L^4, while the WFM implementation in Kwant scales with L^3. Here we explore more diverse situations to numerically verify that the WFM method is more efficient than L^3, as discussed in Sec. 2.2.

Let us begin considering a nearest neighbor (nn) tight-binding Hamiltonian in a two-dimension square-lattice of length L and width W in number of sites. We take W' as the width of the leads (see inset of Fig. 2.5a). We set $E = 0$. In this case, we recall that for semi-infinite square lattice leads the number of open channels at the left and right leads $N_L = N_R = W'$. This model stems for instance from a finite-difference discretization of the

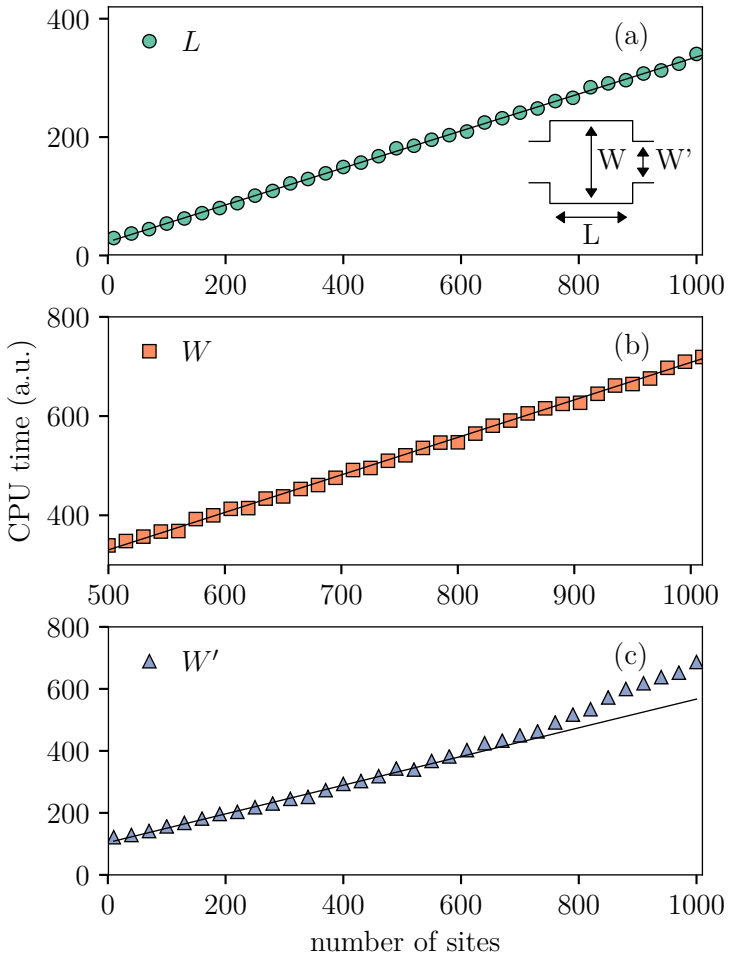

Fig. 2.4 CPU time for the computation of the conductance as a function for a square lattice system of (a) length L (for W and W' fixed), (b) width W (for L and W' fixed), and (c) lead width W' (for L and W constant). Since $E = 0$, $W' = N_R = N_L$. Solid lines indicate linear fittings.

Schrödinger equation of a mesoscopic two-dimensional electron gas (2DEG) [68, 8]. For this model, the optimal partition of the RGF consists of L partitions (slices) with W sites each.

Figure 2.4 gives the CPU time (in arbitrary units) necessary to compute the conductance of the system, Eq. (2.9), as a function of L, W, and W'. It should be emphasized that in both implementations, the linear algebra calculations are coded in lower level programming languages, making this comparison possible.

As discussed in Sec. 2.2 one has to solve N_P times the sparse linear system of dimension $N_S + M_T$, Eq.(2.32). Since the number of operations to solve a sparse system scales as $\mathscr{O}(N)$ [63] and here $M_T = 2W'$, the WFM is expected scale as $(LW + 2W')W'$. Figure 2.4a to 2.4c verify that this conjecture is indeed correct. As a consequence, the performance of the WFM

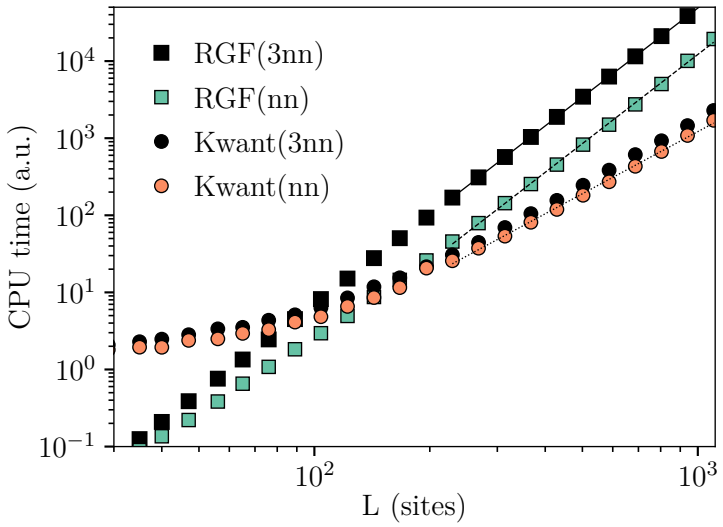

Fig. 2.5 CPU time as a function of the side of a $L \times L$ system. The lines correspond to the best aW^b fit. For Kwant (nn) $b \approx 2.7$ (dotted line), for RGF (nn) $b \approx 3.8$ (dashed line), and for RGF (3nn) (solid line). Kwant 3nn displayed the same trend as the corresponding nn.

method is much better than previously believed [21] for a realistic model of a nanostructure, $M_T = 2W' \ll W$.

Let us now examine a situation where $W = W'$. Figure 2.5 clearly shows that the CPU time of the RGF (nn) method scales with L^4, as expected by the matrix multiplication and diagonalization operations involved. In distinction, the WFM shows a much better CPU performance scaling as L^3 (here $L = W = W'$). However, the overall pre-factor is typically large, making the method clearly advantageous only for $W \gtrsim 10^2$ sites.

We use this setting to investigate the efficiency of the WFM method when dealing with tight-binding Hamiltonians that consider hopping matrix elements beyond nearest-neighbor sites. This is the case in tight-binding models based on Wannier wave functions [69], that are very practical and accurate tools to model large scale disorder systems. Let us consider a square lattice tight-binding Hamiltonian with up to the 3-rd nearest-neighbor (3nn) hopping terms. Since for the RGF method, only neighboring partitions should be connected in this model, one has to double the size of each slice, $W \to 2W$, reducing the total number of slices by half $L \to L/2$. Hence the CPU time grows by a factor of 4 (solid line of Fig. 2.5). In Fig. 2.5 we show that Kwant is practically insensitive to the coordination number of the lattice model, which represents a huge advantage over RGF.

Let us now analyze the memory usage of both methods. As already pointed out in Ref. [21], the memory usage in Kwant can be ten times larger than an RGF implementation which is a problem for computation of transport properties in large systems. In what follows

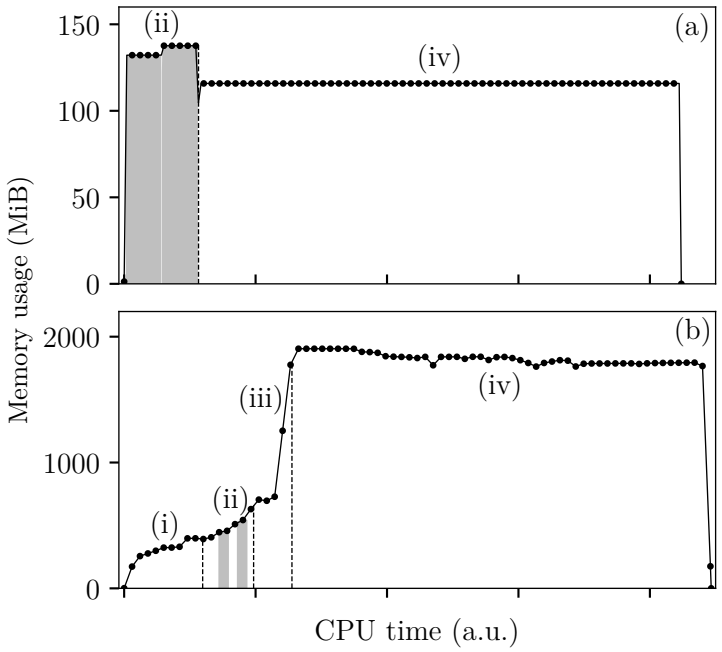

Fig. 2.6 Memory usage as a function of processing time in the calculation of the conductance for a nearest-neighbor tight-binding model of square lattice of dimensions $L = 1000$ and $W = 600$ for (a) the RGF and (b) the Kwant method. The different stages of the computation are indicated by (i) to (iv), see main text.

we study this issue in more detail, examining the intermediate processes, such as the leads eigenmodes calculation, the linear system construction and factorization, and the solving stage, regions (ii)-(iv) of Fig. 2.6, respectively. This stage-by-stage information of the memory usage gives a clear view of the method advantages and bottlenecks.

Figure 2.6 shows the memory usage in a conductance calculation for both the WFM and the RGF implementations. A huge difference can be noted between the maximum memory used for each method. In Kwant, a preliminary time is spent in reading the input parameters, stage (i), which is negligible in the RGF Fortran 90 implementation and it is not displayed. The next stage in both methods, indicated by (ii) in Fig. 2.6, is related to the computation of the lead contribution, namely, the lead surface Green's function in the RGF [8] and the eigenmode diagonalization in WFM. In both methods, this is done twice for our two-probe model and $\Lambda-$times in general systems. Kwant spends an extra time in the factorization of the linear system, Eq. (2.33).

At the solving stage, indicated by (iv) in Fig. 2.6, we observe that Kwant requires one order of magnitude more memory than the RGF method. This is the only feature where the RGF outperforms the WFM methods. We note however that WFM approach allows for

the computation of local operators (such as local currents and LDOS) with no significant additional cost, which is not the case for the RGF method.

Both methods are very robust and accurate. In our extensive tests, the computed conductances agree within the numerical precision. Even in the cases where the Green's function regularization factor η is known to require a special choice in RGF, suc as transmission by evanescent modes in graphene [70], the WFM method gives reliable results without any particular adjustment.

We conclude this chapter by mentioning that the WFM method allows for a straightforward generalization for multi-terminal systems with nontrivial sample geometries, while the RGF approach resorts on ingenious schemes to deal with such situations [11, 10]. In addition, the Kwant package also offers a set of implementation tools to facilitate the study of a wide range of settings, such as multi-orbital atomic states, general lattice connectivity and geometry, to name a few. Several of these tools are largely used throughout this thesis.

In the following chapter, we discuss two applications.

Chapter 3

Application I: Weak-localization in rippled disordered graphene sheets

Disorder is ubiquitous in graphene systems. The main sources of disorder in deposited graphene single crystal monolayers can be either intrinsic, such as vacancies, or extrinsic, such as adatoms and charge puddles. Vacancies are believed to give small contribution to the conductivity in exfoliated samples of graphene, strain fields can be the dominant scattering mechanism for high-quality samples by causing distortions over the lattice in the form of ripples [71]. It has been shown [72] that ripples in graphene can affect the mobility of charge carriers by two mechanisms. Ripples are deformations with typical lengths much larger than the lattice parameter smoothly changing the interatomic distance can be mapped into an effective pseudo-magnetic vector potential whose magnitude scales with lattice distortions. The other feature appears by applying an in-plane magnetic field to a rippled surface. The disordered local curvature of the graphene surface gives rise to a random magnetic field perpendicular to the sheet. It is known that competition between the two mechanisms generates a strong anisotropic conductivity tensor.

In this chapter we numerically study the weak localization (WL) and the weak anti-localization (WAL) effect, the leading quantum correction terms to the conductivity of disordered graphene systems. The available analysis of WAL and WL in disordered graphene uses a theory [73] based on a diagrammatic perturbation in powers of $(k_F l_e)^{-1}$. Close to the charge neutrality point $k_F l_e \to 0$, the problem becomes non-perturbative. Despite the importance of the problem, with few exceptions[74, 75], the previous theoretical approaches used to interpret WL and WAL in graphene are not quantitatively adequate[76]. Therefore, one needs to resort to numerical methods.

Hence, we study this problem by means of numerical calculation of the conductivity using the Kwant package, whose methods are documented in the previous chapter. Ripple disorder

is modeled by properly accounting for the hopping integrals between neighboring sites. We show that these types of disorder critically affects the sign of the quantum corrections to the conductivity at low external magnetic fields, causing a crossover of the magneto-conductivity from a weak-localization (WL) and an weak-anti-localization profile (WAL) as function of the disorder strength and range.

We also present a method to show the competition between the pseudomagnetic field effect due to rippled graphene and a geometric contribution comming from an external field. The motivation for this study is to show that the current models used in most strained-graphene simulations in literature can overestimate the pseudomagnetic field and neglects the geometric contribution of the ripples to the external field in some cases. By the end of the chapter, we draw a few conclusions.

3.1 Theoretical background

In the following section, we define the important transport length scales to discuss localization in the diffusive regime.

3.1.1 The characteristic lengths of the mesoscopic transport

The different mesoscopic regimes can be classified by using a few characteristic length scales, namely, the conductors size L, the Fermi wavelength λ_F, the elastic mean free path l_e adn the phase coherence length l_ϕ. The Fermi wavelength λ_F is the wavelength of conducting electrons of highest kinetic energies and defines the current wavelength. The electrons mean free path l_e is the average length an electron travels before its momentum is relaxed due to elastic disorder scatterings. The phase coherence length l_ϕ is the largest scale over which one can observe electrons phase interference phenomena. Inelastic scattering processes such as phonons and electron-electron interactions, destroy the single-particle electronic phase coherence. All these length scales are material-dependent and are strongly affected by temperature[8].

Macroscopic conductors of ohmic behavior are diffusive ($L \gg l_e$) and have a characteristic size much larger than the phase coherence length, $L \gg l_\phi > \lambda_F$. The quantum mechanical nature of the conductors charge carriers is lost causing the electronic current properties to be well-described by the classical Drude model, which predicts a conductivity of of $\sigma_D = 2e^2\tau/m$ where $\tau = l_e/v_F$, v_F is the Fermi velocity and m is the effective charge carrier mass. Within such regime, electrons can be scattered by impurities but interference effects between different scattering events are negligible.

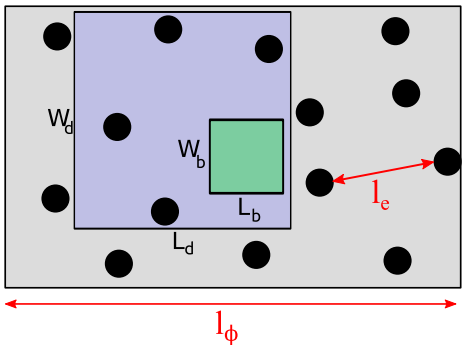

Fig. 3.1 Picture of characteristic transport scales exemplifying a ballistic device of size L_b, W_b (green region) and a diffusive device of size L_d, W_d (purple region).

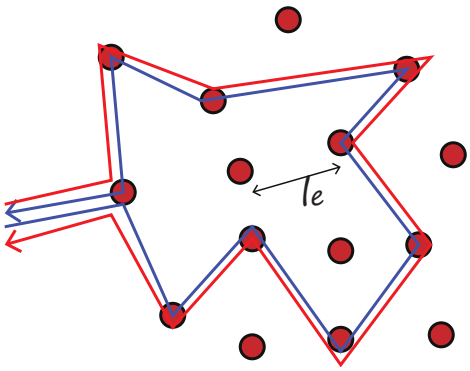

Fig. 3.2 Example of closed Feynman path (red) and its time-reversed counterpart (blue) that causes particle enhanced backscattering in the presence of quantum coherence.

In contrast, when the system size is smaller than electronic mean free path and the phase coherence length, such as $l_\phi > l_e > L > \lambda_F$, the charge transport is ballistic. In this case, the transport properties can be cast into boundary conditions problems (see Fig. 3.1).

There is also an intermediate regime where the system size is typically much larger than electrons mean free path but still smaller than the phase coherence length $l_\phi \gtrsim L > l_e > \lambda_F$, namely, the diffusive regime. In this case, electrons are frequently scattered by impurities but preserve their quantum coherence over the system length scale L. Therefore, quantum interference gives rise to significant quantum corrections to the Drude formula due to the presence of localization effects.

Electronic scatterings due to disorder tend to localize the wave-functions[77] in a finite region of length inversely proportional to the disorder strength. This led us to the definition of a localization length ξ, whose a small ξ defines a localized state while a large ξ defines an extended state.

A coherent conductor is said to be under the strong localization regime if the localization length is comparable to or smaller than the conductor's length ($L \gtrsim \xi$). In this case, electronic wave functions are predicted to decay exponentially in space and proportionally to the localization length. From the other hand, if the conductors' length is much smaller than the localization length ($L \ll \xi$), the system is in the weak localization regime, and a perturbation theory predicts the existence of disorder-dependent correction terms to Drude classical conductivity due to quantum interference.

From the other and, there is the weak localization regime in coherent conductors. The contributions from the quantum interference of weak localizations to electronic transport can be qualitatively understood as follows: in Feynman path approach, transport through a disordered media can be seen as the sum of all possible paths from source to drain. Disorder (see Fig.3.2)can originate backscattering, that is the scattering toward the same state i from which the particle comes. The set of all such paths contributes to the reflection coefficient R_{ii} associated to the current. According to Feynman theory, these paths form closed loops and their time-reversed counterparts also counts in the sum. By denoting a single path probability amplitude as A^+ and its time-reversed counterpart as A^-, the corresponding backscattering probability is given by:

$$R_{i\to i} = |A^+ + A^-|^2 = \underbrace{|A^+|^2 + |A^-|^2}_{\text{Drude}} + \underbrace{A^{+*}A^- + A^+A^{-*}}_{\text{quantum interference}} \tag{3.1}$$

We note that at zero magnetic field, $|A^+| = |A^-| = A$ and the reflection probability is $R_{i\to i} = 4|A|^2$, while a decoherent backscattering has a probability of reflection of $R_{Cl} = 2|A|^2$ due to the vanishing of the second term of Eq (3.1). The paths interference leads to the enhancement of the backscattering and consequently to an increased resistance in mesoscopic devices. This phenomenon is called weak localization.

The application of an external magnetic field adds an area-dependent Aharonov-Bohm (AB) phase to the scattering amplitudes, $A^\pm = Ae^{\pm i\phi_{AB}(S)}$. As a consequence, reflection has a parameterized interference term:

$$R_{i\to i} = 2|A|^2 + 2|A|^2 \cos\left[2\phi_{AB}(S)\right]. \tag{3.2}$$

If we now consider all possible paths corresponding to the $i \to i$ transition amplitude, the interference term has to be replaced by its average. For small values of the magnetic field, such that most paths correspond to $\phi_{AB} \ll \pi$, the correction is small. On the other hand, for sufficiently large N, ϕ_{AB} can be large and, on average, the cosine term vanishes. Hence:

$$R_{i\to i} = R_{Cl}, \tag{3.3}$$

which corresponds to the classical Drude term. Therefore, the quantum correction contribution to backscattering is maximal when $B = 0$. As the field is increased, one observes a suppression of backscattering and the quantum correction to the Drude conductivity disappears. Such weak-localization curve as a function of the magnetic field B has a dependence on the disorder characteristics by means of scattering rates [78].

3.1.2 General electronic aspects of graphene

Let us briefly review the general electronic aspects of pristine graphene to obtain the effective tight-binding model, suitable for the methods described in the previous section. Then, we proceed by discussing the Dirac model of the Hamiltonian near charge neutrality point until second order correction term. We show how the two kinds of disorder discussed in this chapter can be included under tight-binding representation and modify the onsite and hopping energies. Finally, we address an external magnetic field, included by Peierls substitution, and a pseudomagnetic strain field to the model, respectively.

Graphene is a sheet of carbon atoms arranged in honeycomb lattice. The carbons ordinary orbitals s, p_x and p_y of the outermost shell couple to form the sp^2 hybrid orbitals constituting the localized σ-bonds each carbon forms with its neighbors. The remaining p_z orbital is directed perpendicularly to the σ-bonds plane forming the delocalized π-bonds and are responsible for most of the transport phenomena observed[4]. The lattice can be seen as a triangular lattice with a two-atoms unit cell, from now on labeled as A and B. Each atom of the unit cell is bonded to its neighbors in a trigonal planar structure with reflection symmetry to each other. The primitive lattice vectors are:

$$\mathbf{a}_1 = \frac{a}{2}\left(\sqrt{3}, 1\right) \qquad \mathbf{a}_2 = a\,(0,1) \tag{3.4}$$

with a lattice parameter of $a = 2.46$Å. The vector connecting A to its neighbors are[1] (see picture 3.1.2):

$$\Delta_1 = \frac{a}{2}\left(\frac{\sqrt{3}}{3}, 1\right), \qquad \Delta_2 = \frac{a}{2}\left(\frac{\sqrt{3}}{3}, -1\right), \qquad \Delta_3 = -a\left(\frac{\sqrt{3}}{3}, 0\right) \tag{3.5}$$

[1] This is a convenient choice of reference system when one is interested in armchair cut pointed to x direction and zig-zag cut in y direction, as seen in picture 3.1.2. Other forms of orientation are also possible.

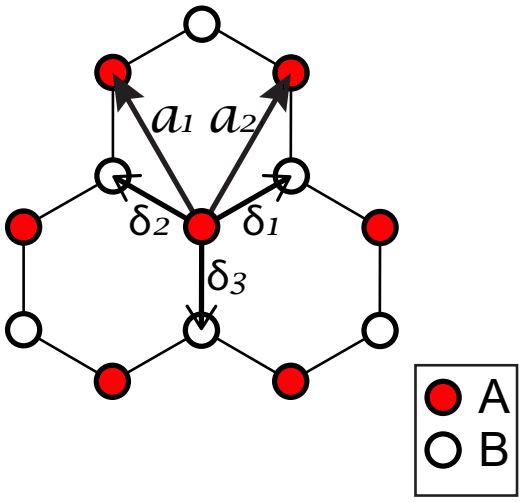

Fig. 3.3 Sublattices of the honeycomb lattice with example of basis vector and displacement vectors.

Position of atoms over the lattice are then given by the two Bravais lattices vectors:

$$\mathbf{R}^A = n\mathbf{a}_1 + m\mathbf{a}_2 \qquad \mathbf{R}^B = \mathbf{R}^A + \Delta_1 \tag{3.6}$$

where m and n are integer indices that run over the whole lattice. Now we are abled to write down the nearest-neighbors tight-binding Hamiltonian including the hopping $t(\mathbf{R},\Delta_i)$ and onsite $\varepsilon(\mathbf{R})$ energies to the p_z electrons:

$$\begin{aligned} H = & \sum_{\substack{\mathbf{R} \\ i=1,2,3}} \left[t(\mathbf{R},\Delta_i) a^\dagger(\mathbf{R}) b(\mathbf{R}+\Delta_i) + H.c. \right] \\ & + \sum_{\mathbf{R}} \left[\varepsilon^A(\mathbf{R}) a^\dagger(\mathbf{R}) a(\mathbf{R}) + \varepsilon^B(\mathbf{R}+\Delta_1) b^\dagger(\mathbf{R}+\Delta_1) b(\mathbf{R}+\Delta_1) \right] \end{aligned} \tag{3.7}$$

The position dependent hopping and onsite energies are useful for the inclusion of scalar and vector disorder models. This is the Hamiltonian model used in the numerical methods. From now on, we review the translational symmetric analytical model in momentum-space representation to formulate the foundations over which the disorder theory is based.

3.1.3 Pristine graphene near charge neutrality point

The flat graphene infinite sheet in the absence of disorder is translational invariant. The hopping amplitude for this situation is $2.7eV$[4]. The onsite energies are also space-independent

and should be taken as zero $\varepsilon^A = \varepsilon^B = 0$ once they contribute only for a constant shift in energy.In reciprocal space the basis operators read [9]:

$$a(\mathbf{R}) = \sum_{\mathbf{k}\in \mathrm{ZB}} e^{i\mathbf{k}\cdot\mathbf{R}} a(\mathbf{k}), \quad b(\mathbf{R}) = \sum_{\mathbf{k}\in \mathrm{ZB}} e^{i\mathbf{k}\cdot\mathbf{R}} b(\mathbf{k}) \tag{3.8}$$

The Hamiltonian (3.7) in momentum space becomes:

$$H = \sum_{\mathbf{k}\in \mathrm{ZB}} \left[a^\dagger(\mathbf{k}) f(\mathbf{k}) b(\mathbf{k}) + b^\dagger(\mathbf{k}) f^*(\mathbf{k}) a(\mathbf{k}) \right] \tag{3.9}$$

Where $f(\mathbf{k})$ reads:

$$f(\mathbf{k}) = -t(e^{-i\mathbf{k}\cdot\Delta_1} + e^{-i\mathbf{k}\cdot\Delta_2} + e^{-i\mathbf{k}\cdot\Delta_3}) \tag{3.10}$$

Writing down the Hamiltonian in matrix form, we have:

$$H = \begin{pmatrix} 0 & f(\mathbf{k}) \\ f^*(\mathbf{k}) & 0 \end{pmatrix} \tag{3.11}$$

whose eigenvalues are:

$$E_\pm(\mathbf{k}) = \pm|f(\mathbf{k})| = \pm t\sqrt{3 + 2\cos(k_y a) + 4\cos\left(\frac{k_y a}{2}\right)\cos\left(\frac{\sqrt{3}k_x a}{2}\right)} \tag{3.12}$$

The $\pm$ sign of equation (3.12) are represent the π bond and π^* anti-bond discussed previously. The bands have two nonequivalent high symmetry crystal points $\mathbf{K}$ of the Brillouin zone where the energy vanishes $f(\mathbf{K}) = 0$, labelled $\mathbf{K}(\mathbf{K}')$. To understand the electronic properties around $E \approx 0$, the Fermi energy in undoped regime, we expand $f(\mathbf{k})$ for $\mathbf{K}(\mathbf{K}') + \mathbf{q}$ where $|\mathbf{K}(\mathbf{K}')| \gg |\mathbf{q}|$ until second order gives:

$$\begin{aligned} f(\mathbf{K}^\pm + \mathbf{q}) &\approx f^{(0)}(\mathbf{q}) + f^{(1)}(\mathbf{q}) + f^{(2)}(\mathbf{q}) \\ &= -\frac{3ta}{2\sqrt{3}}(q_x \pm i q_y) - \frac{ta^2}{4}\left(q_x^2 - q_y^2 \pm i 2 q_x q_y\right) \end{aligned} \tag{3.13}$$

The Hamiltonian has four dimensions $(KA, KB, K'B, K'A)$ and can be expresses compactly using a set of Pauli matrices for each degree of freedom and substituting $\mathbf{q} \to \mathbf{k}$:

$$H = -v_F \zeta_z \otimes \sigma \cdot \mathbf{k} - \mu\left[\sigma_x(k_x^2 - k_y^2) - \sigma_y(k_x k_y)\right] \tag{3.14}$$

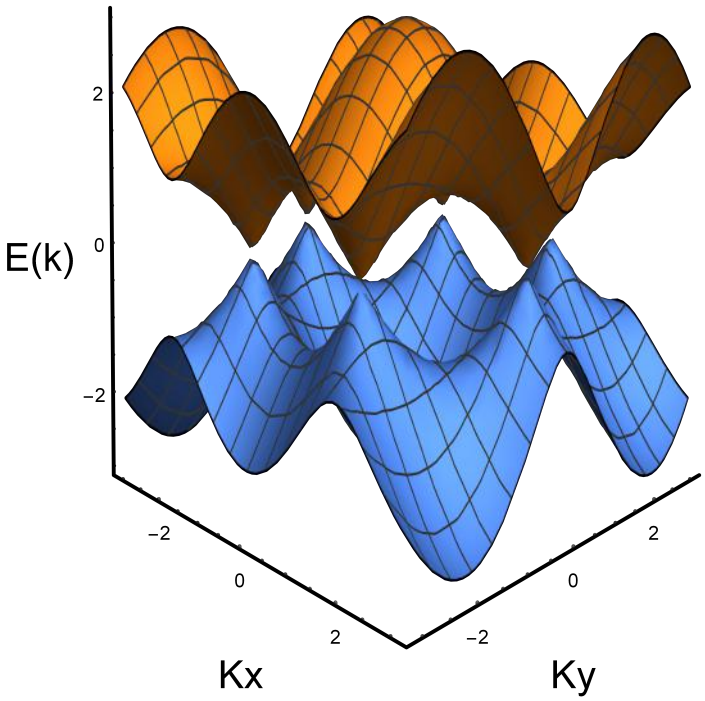

Fig. 3.4 Graphene band structure

The first term constitutes the Dirac-like term for a fermionic particle of velocity v_F. The second term gives the trigonal warping correction which is responsible for the rotational symmetry breaking of the Dirac cones.

According to McCann and co-workers[73], the weak localization effect captures the valley symmetry breaking caused by the warping term. To point out the associated isospin and pseudospin symmetry breaking, the set of 4×4 matrices $\Sigma_x,\Sigma_y,\Sigma_z$ and $\Lambda_x,\Lambda_y,\Lambda_z$ were introduced and are associated with the Pauli matrices by:

$$\begin{aligned} \Sigma_x &= \zeta_z \otimes \sigma_x, \qquad \Sigma_y = \zeta_z \otimes \sigma_y, \qquad \Sigma_z = \zeta_0 \otimes \sigma_z \\ \Lambda_x &= \zeta_x \otimes \sigma_z, \qquad \Lambda_y = \zeta_y \otimes \sigma_z, \qquad \Lambda_z = \zeta_z \otimes \sigma_0 \end{aligned} \tag{3.15}$$

They allow us to rewrite equation (3.13) in the convenient way[73]:

$$H = v_f(\Sigma\cdot\mathbf{k}) - \mu\Sigma_x(\Sigma\cdot\mathbf{k})\Lambda_z\Sigma_x(\Sigma\cdot\mathbf{k})\Sigma_x \tag{3.16}$$

Disorder can be included in the effective Hamiltonian by adding a general term of the form[75]:

$$H_{imp} = V_{0,0}(r) + \sum_{i,j=x,y,z} \Sigma_i\Lambda_j V_{i,j}(r) \tag{3.17}$$

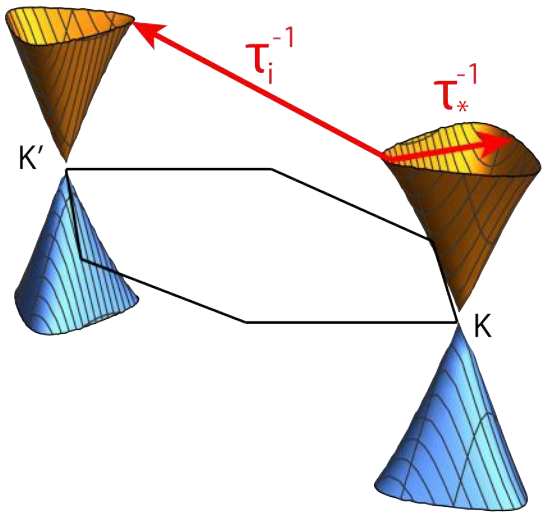

Fig. 3.5 Schematic picture of intervalley and intravalley scatterings and the respective scattering rates τ_i^{-1} and τ_*^{-1}. For energies sufficiently far from the charge neutrality point, the Dirac cones lose rotational symmetry and a warping correction of second order in momentum expansion have to be taken into account into the Hamiltonian.

the corresponding scattering rates in first Born approximation are then:

$$\tau_{ij}^{-1} = \frac{2\pi\nu}{\hbar} V_{i,j}^2 \tag{3.18}$$

where ν is the density of states.

Let us now discuss how the character of the disorder terms $V_{i,j}$ can influence transport properties in graphene.

3.1.4 Impurities in graphene: long range vs short range disorder

Applying the Fourier transform to the disorder elements, one obtains its momentum component[79]:

$$V_{\mathbf{k}}^A = \frac{\sqrt{3}a^2}{2} \sum V(\mathbf{R}) e^{-i\mathbf{k}\cdot\mathbf{R}} \tag{3.19}$$

$$V_{\mathbf{k}}^B = \frac{\sqrt{3}a^2}{2} \sum_{\mathbf{R}} V(\mathbf{R} - \Delta_1) e^{-\mathbf{k}\cdot\mathbf{R}} \tag{3.20}$$

Using the four components matrix form, $V_{\mathbf{k}}^{A,B}$ reads:

$$V_{\mathbf{K}}^{A} = \begin{pmatrix} V_0 & 0 & 0 & V_{\mathbf{k}_0} e^{-2i\mathbf{k}_0\cdot\mathbf{R}} \\ 0 & V_0' & 0 & 0 \\ 0 & 0 & V_0' & 0 \\ V_{\mathbf{k}_0} e^{2i\mathbf{k}_0\cdot\mathbf{R}} & 0 & 0 & V_0 \end{pmatrix} \tag{3.21}$$

$$V_{\mathbf{K}}^{B} = \begin{pmatrix} V_0 & 0 & 0 & 0 \\ 0 & V_0' & V_{\mathbf{k}_0} e^{-2i\mathbf{k}_0\cdot\mathbf{R}} & 0 \\ 0 & V_{\mathbf{k}_0} e^{2i\mathbf{k}_0\cdot\mathbf{R}} & V_0' & 0 \\ 0 & 0 & 0 & V_0 \end{pmatrix} \tag{3.22}$$

where k_0 is the distance between to inequivalent Dirac cones in k-space. For short-range impurities:

$$V_0 = V_{\mathbf{k}_0} = V, \qquad V_0' = V_{\mathbf{k}_0}' = 0 \tag{3.23}$$

electrons are scattered in the same sublattice, which is equivalent to a potential shift only at a particular position of the lattice. Similarly, for long-range impurities:

$$V_0 = V_0' = V/2, \qquad V_{\mathbf{k}_0} = V_{\mathbf{k}_0}' = 0 \tag{3.24}$$

impurities cause electrons to scatter in sublattices equally but within the same valley. The scattering length is dependent on correlation length of scatterers and are considered in the Gaussian impurity models discussed in the next sections.

3.2 Motivations

The theory of quantum corrections in diffusive disordered electronic systems is based on a diagrammatic perturbation theory in inverse powers of $k_F l_e$, where l_e is the characteristic electronic elastic mean free path. This theory has been used to interpret weak localization (WL) and weak anti-localization (WAL) regimes in graphene close to the charge neutrality point. However, in this regime, $k_F l \to 0$ which makes the perturbation theory questionable.

3.2.1 The conductivity correction term in graphene

Theory predicts that the conductivity in 2D metallic samples at mesoscopic scale shows quantum corrections due called weak localization (WL), that depend locarithmically on the

phase-coherence scattering rate τ_ϕ and elastic mean free time τ_e[80]:

$$\Delta\sigma = -\frac{e^2}{\pi h}\ln\left(\frac{\tau_\phi}{\tau_e}\right) \tag{3.25}$$

Weak localization corrections are ubiquitous in a number of experimental settings. Weak localization contributes to the decrease in the Drude conductivity due to enhanced backscattering caused by quantum interference of time-reversed closed paths. The dephasing time τ_ϕ accounts for inelastic processes that destroy quantum coherence. In the presence of external magnetic field, coherence phases are area-dependent and vanishes out at mesoscopic averages causing an increase in conductivity.

However, an increase in the conductivity was also observed for a class of mesoscopic materials, a phenomenon subsequently explained by strong spin-orbit interactions[81]. A conductivity correction formula was derived by diagrammatic technique containing extra terms logarithmically dependent on the characteristic spin-orbit scattering rates τ_{SO}.

Although graphene typically has a weak spin-orbit interaction[82], electrons in graphene have a chiral nature due to sublattice degree of freedom. Large momentum scattering due to short range impurities can give rise to an intravalley scattering rate τ_i. There is also another spin-like component associated with valey degeneracy that also results in an intervalley scattering rate τ_z. Ref. [73] gives an expression for the magnetoconductance in graphene, taking into account all these possible scattering processes, namely:

$$\Delta\sigma(B) = \frac{e^2}{\pi h}\left[F\left(\frac{\tau_B^{-1}}{\tau_\phi^{-1}}\right) - F\left(\frac{\tau_B^{-1}}{\tau_\phi^{-1}+2\tau_i^{-1}}\right) - 2F\left(\frac{\tau_B^{-1}}{\tau_\phi^{-1}+\tau_i^{-1}+\tau_*^{-1}}\right)\right] \tag{3.26}$$

where $\tau_* = \tau_z + \tau_w$ is incremented by an intravalley scattering rate τ_w due to the second order term in the expansion of the Hamiltonian for low energies, the warping term. Here $F(x) = \ln(x) + \psi\left(\frac{1}{x}+\frac{1}{2}\right)$ and $\psi(x)$ is a digamma function. Together, they account for intravalley and intervalley scattering but misses contributions from the pseudomagnetic field due to ripples. Also, an in-plane magnetic field could have an explicit contribution to this equation in the form of a perpendicular random field projected over the graphene sheet.

3.2.2 The suppression of the WL effect in parallel magnetic field

From the experimental side, WL effects have been extensively investigated motivated by the quest for a quantitative understanding of the scattering disorder processes in graphene. Along with conductance fluctuations, these scattering phenomena could act as a probe to nanoscopic characteristics due to its sensibility to the size and strength of impurities[83].

By means of magnetotransport measurements, one estimates scattering rates by fitting the weak localization behavior under the external magnetic field with the predicted curve Eq. 3.26. One can also include an external in-plane magnetic field sensible to the curvatures of graphene ripples[84].

It has been experimentally demonstrated that the application of a in-plane magnetic field $B_{||}$ to a graphene flake on SiO_2 substrate cooled to $40mK$ in a weak localization experiment is capable to suppress the weak localization effect where $B_{||}$ effectively decreases τ_ϕ. Also, a strong anisotropic magnetoconductance has been verified over the dependence of the direction of the applied in-plane field.

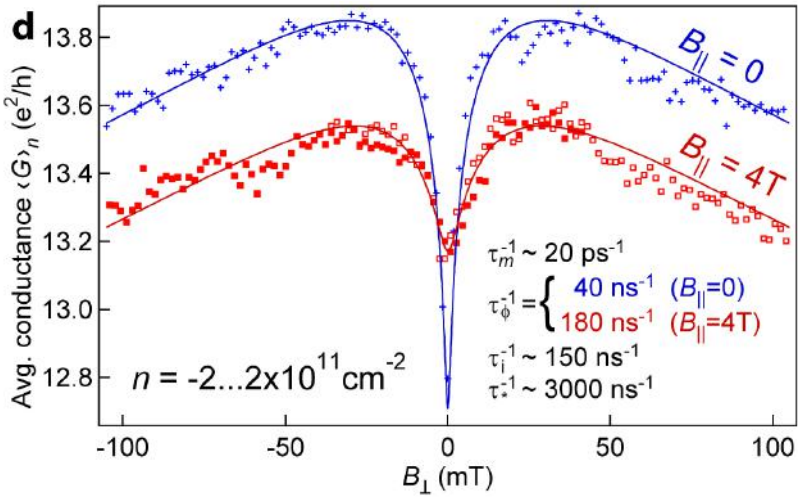

Fig. 3.6 The magnetic field dependence of mangetoconductance shows an increase of conductance and suppression of weak localization over the sample for a perpendicular field $B_\perp$ as expected from the break of coherent-phases of the increased back-scattering effect. Then, a parallel magnetic field was applied $B_{||}$ causing a smoothing to the whole curve, fact attributed to the dephasing of a random effective perpendicular gauge field $\delta B_\perp$.[84]

3.2.3 Ripples: random fields contributions to conductivity

An external in-plane magnetic field applied to a graphene sheet has been recently considered in the theoretical approach motivated by the Lundeberg-Folk experiments[84], among others[72].There, the effect of strain random fields on the Drude conductivity was addressed in the form of two mechanisms: (i) A pseudo magnetic-field is generated due to the strained bonds between the carbon atoms. (ii) A random effective field projected perpendicularly to the surface is obtained as the result of the applied in-plane field. An anisotropy due to the in-plane field was found due to the effective field while the strained pseudomagnetic field contributed isotropically to the conductivity[84, 72]. Although Ref. [84] successfully reproduces the measurements of anisotropy by introducing in the model surface roughness inferred by the AFM measurements, as mentioned in the introduction, the effective low-energy Hamiltonian is the result of an expansion taken near the charge neutrality point and the standard diagrammatic perturbative expansion that describes well the conductivity of a disordered graphene[85] considers the high doping regime, taking $(k_F l)^{-1}$ as its small parameters. Hence, a numerical investigation is in order for testing the a diagrammatic perturbation approach predictions.

3.3 The disorder models in tight-binding approximation

We describe the electronic dynamics in graphene using the tight-binding approximation described in section 3.1. The Kwant package also offers a suite of functionalities to facilitate the process of writing the Hamiltonian matrix. The user only needs to know the lattice primitive vectors and the system tight-binding values, i.e., the onsite and hopping energies.

Now we discuss how to include the two disorder models considered in this study, which describes both scalar and vector random disorder scattering processes.

3.3.1 The onsite disorder

We model the local scalar disorder as a Gaussian white-noise:

$$V(\mathbf{r}_i) = \sum_{n=1}^{N_{imp}} u_n e^{-|\mathbf{r}_i - \mathbf{R}_n|^2/2\sigma^2} \tag{3.27}$$

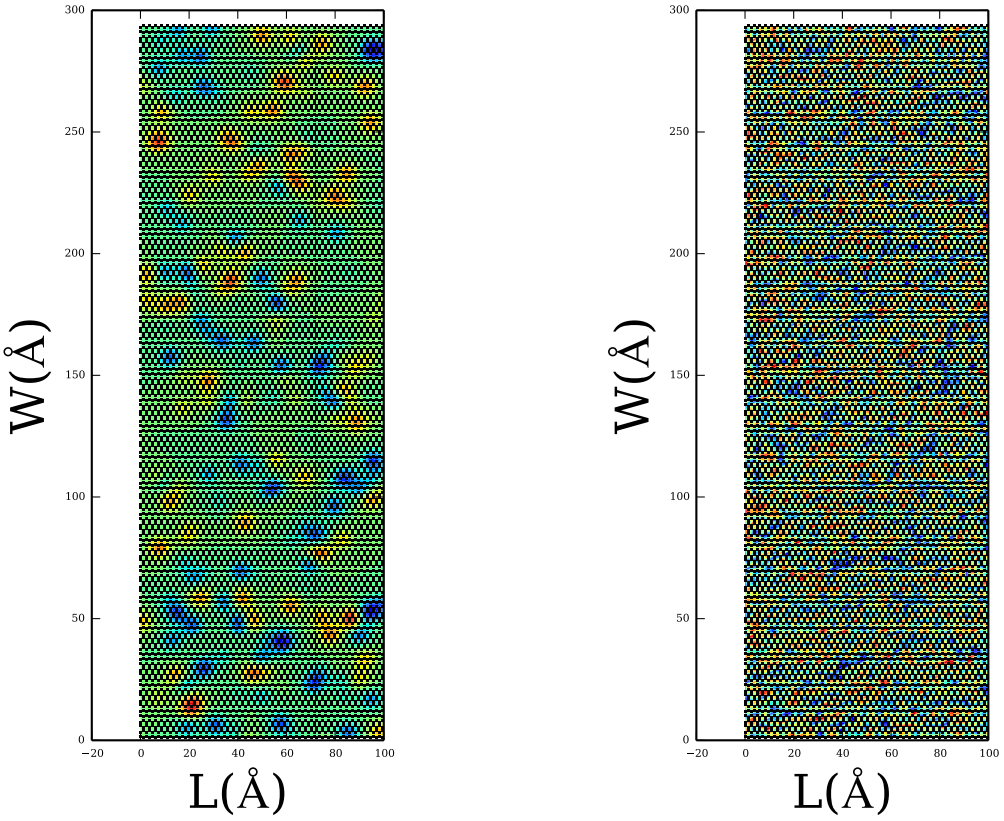

(a) Long-range (b) Short-range (Anderson)

Fig. 3.7 Examples of disorder realizations for $L = 40a$ and $W = 3L$ and $n_{imp} = 0.022$.

where $\mathbf{r}_i$ is the real-space coordinate of the lattice site[2]. $V(\mathbf{r}_i)$ is a sum of N_{imp} Gaussians with random amplitude uniformly distributed in the interval $u_n \in [-h_{max}, h_{max}]$ and centralized at random sites $\mathbf{R}_n = (X_n, Y_n) \in [0, L] \times [0, W]$. We keep the correlation length σ as a constant.

The total number of atoms in the sample is $N_{tot} = \frac{4\sqrt{3}}{3}\frac{LW}{a^2}$. For long range correlation lengths $\sigma \gg a$, we consider the diluted case of impurity density, $n_{imp} = N_{imp}/N_{tot}$. For the opposite case $\sigma \ll a$, we study the Anderson disordered model where $N_{imp} = N_{tot}$. A useful quantity to characterize the disorder strength is the dimensionless correlator is[83]:

$$K_0 = \frac{LW}{(\hbar v_F)^2 N_{tot}^2} \sum_{i=1}^{N_{tot}} \sum_{j=1}^{N_{tot}} \langle V(\mathbf{r}_i) V(\mathbf{r}_j) \rangle \tag{3.28}$$

For sufficiently large systems, taking the average value of 3000 realizations of the disordered onsite potential in graphene samples, we readily verified in our simulations the theoretically predicted limiting cases of K_0 for both regimes:

[2]In this part we do not distinguish between the sublattices A and B when referring to the lattice sites as this is a general formulation

$$K = \frac{\sqrt{3}}{9}\left(\frac{h_{max}}{t}\right)^2 \qquad \sigma \ll a \tag{3.29}$$

$$K = \frac{8\pi}{9}\left(\frac{h_{max}}{t}\right)^2 \left(\frac{\sigma}{a}\right)\frac{N_{imp}}{N_{tot}} \qquad \sigma \gg a \tag{3.30}$$

Figure 3.8 shows the dependence of the correlation strength on the maximum height squared ${h_{max}}^2$ which is preserved for both regimes so as the multiplicative term is convergent. The correlation strength is the one responsible to determine the mean free path in Born approximation when $k_F l \gg 1$.

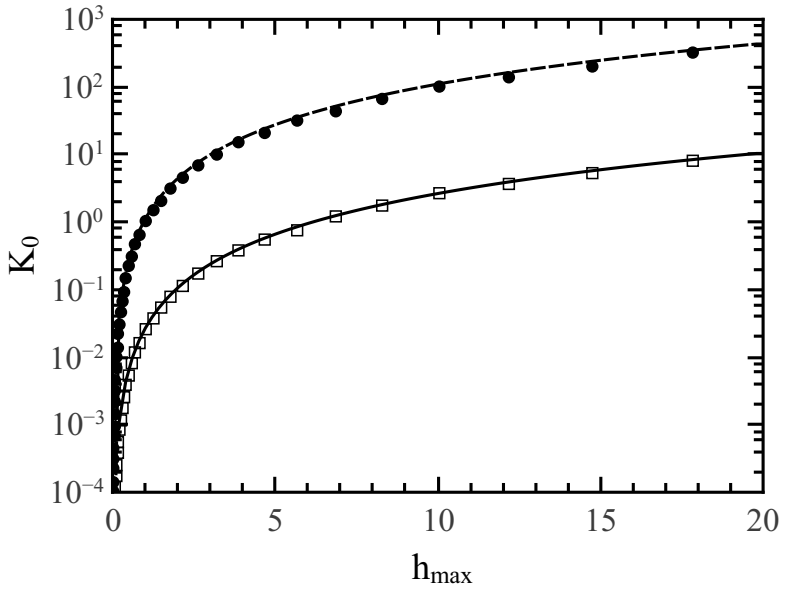

Fig. 3.8 Comparison of the curves with numerical data for the dependence of mean correlation strength with maximum intensity of potential for long range (black circles) and short range - Anderson (white squares) disorder models and respective curved

We calculate the conductance G using the methods described in the previous chapter using the Landauer formula $G = \frac{2e^2}{h}\mathrm{Tr}\{\mathbf{t}\mathbf{t}^\dagger\}$. The average conductance $\langle G\rangle$ and variance $\mathrm{Var}G = \langle G^2\rangle - \langle G\rangle^2$ are depicted in figure (3.3.1). They are in agreement with the results of [83] for both long range and short range regimes and evidence increased conductance fluctuations for the stronger disordered. One expects long ranged disorder to behave such as the Anderson disorder where conductance vanishes for large values. However, due to valley symmetry discussed previously, graphene presents increased mean conductance for stronger impurities when correlation is sufficiently large. More discussions regarding mean conductance in graphene can be found in ref. [83].

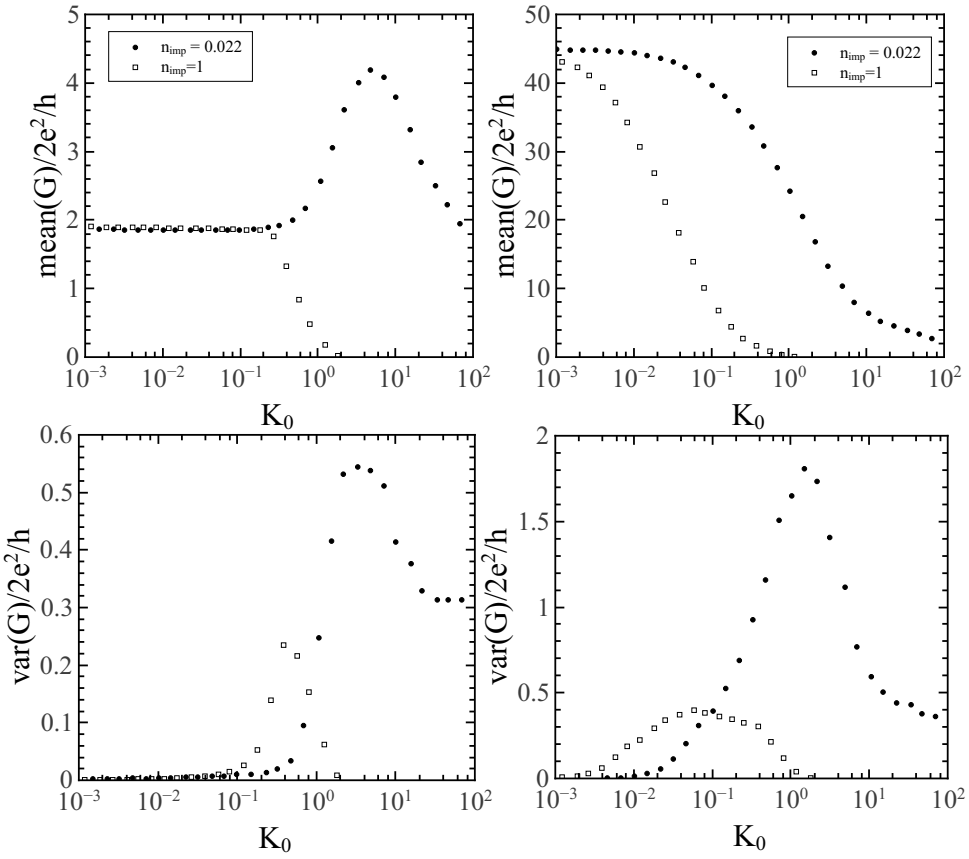

Fig. 3.9 Left pannels: mean and variance of the conductance of 3000 realizations of onsite disorder in graphene with increasing impurity strength K flutuating around the Dirac point (undopped regime). Right pannels: the same as the left pannels but with a small dopping of $t/2$. The correlation length used for the long range case where $n_{imp} = 0.022$ was $\xi = \sqrt{3}a$ while Anderson disorder $n_{imp} = 1$ have no spatial correlation $\xi = 0$.

This model of Gaussian disorder can be used for both electrostatic scalar potential due to charge inhomogeneities in the substrate as well as for long range random ripples in graphene which causes a random vector potential, as discussed later.

3.3.2 The hopping integrals disorder

Lattice deformations change the interatomic distances as well as the local orientation of the π orbitals with respect to the graphene plane. These effects change the value of hopping integrals in the tight-binding model. For small deformations, the hopping integral between two atoms can be successfully modelled by an exponentially decaying dependence on the interatomic distance[86]:

$$t_{ij} = t_0 e^{-\beta\left(\frac{d_{ij}}{a}-1\right)}, \tag{3.31}$$

where $d_{ij} = |\mathbf{r}_i - \mathbf{r}_j|$ is the distance between two neighboring carbon atoms and β is a material-dependent decaying rate that can be infered from experiments

3.4 The effects of magnetic field in a rippled graphene

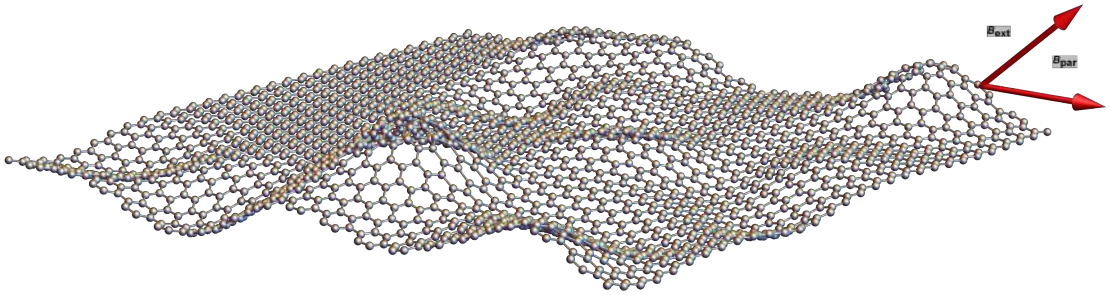

Fig. 3.10 Illustration of disordered ripples in graphene with applied parallel and effective perpendicular magnetic fields

3.4.1 The pseudomagnetic field due to strain

To construct a Gaussian model for ripples in graphene due to random surface deformation, we define the following displacement height field:

$$h(\mathbf{r}) = \sum_{n=1}^{\mathcal{N}_{rip}} h_n e^{-|\mathbf{r}-\mathbf{R}_n|^2/2\xi^2} \tag{3.32}$$

where, similarly, $h_n \in [-z_{max}, z_{max}]$ and $\mathbf{R}_n \in [0,L] \times [0,W]$. The typical displacement of the deformations in graphene are much smaller then the correlation length $\xi \gg z_{max}$ [86]. In this regime of small curvatures, where also $\xi \gg a$, several authors have used elements of the theory of elastic media in tight-binding model and discussed how the ripples $h(\mathbf{r})$ can modify the low-energy dynamics of electrons in graphene sheets.

The strain tensor components u_{ij} of a membrane can be associated to out-of-plane deformations $h(r)$ ad in-plane displacements $u(r)$ by[87]:

$$\begin{aligned} u_{xx}(\mathbf{r}) &= \frac{\partial u_x(\mathbf{r})}{\partial x} + \frac{1}{2}\left[\frac{\partial h(\mathbf{r})}{\partial x}\right]^2, \\ u_{yy}(\mathbf{r}) &= \frac{\partial u_y(\mathbf{r})}{\partial y} + \frac{1}{2}\left[\frac{\partial h(\mathbf{r})}{\partial y}\right]^2, \\ u_{xy}(\mathbf{r}) &= \frac{1}{2}\left[\frac{\partial u_x(\mathbf{r})}{\partial y} + \frac{\partial u_y(\mathbf{r})}{\partial x}\right] + \frac{1}{2}\frac{\partial h(\mathbf{r})}{\partial x}\frac{\partial h(\mathbf{r})}{\partial y}. \end{aligned} \tag{3.33}$$

Strain can be effectively accounted for in the low-energy electronic structure of graphene by introducing in the Hamiltonian a scalar potential V [88]:

$$V^{(0)}(\mathbf{r}) = g\left[u_{xx}(\mathbf{r}) + u_{yy}(\mathbf{r})\right], \tag{3.34}$$

and a vector gauge potential $\mathbf{A}(\mathbf{r}) = (A_x(\mathbf{r}), A_y(\mathbf{r}))$:

$$\begin{aligned} A_x(\mathbf{r}) &= \frac{\hbar\beta\kappa}{ea}[u_{xx}(\mathbf{r}) - u_{yy}(\mathbf{r})], \\ A_y(\mathbf{r}) &= -2\frac{\hbar\beta\kappa}{ea}u_{xy}(\mathbf{r}), \end{aligned} \tag{3.35}$$

for the K-valley and armchair crystallographic orientation along the x-axis. Here, e is the electron charge, t is the hopping integral and $g \approx 4$ eV, $\kappa \approx 1/3$, and $\beta = -\partial \log t/\partial \log a \approx 2$ are dimensionless material parameters that characterize the coupling between the graphene electrons with the lattice deformations.

When in-plane deformations are small, the u_x and u_y derivatives in Eq. (3.33) are negligible. Therefore, for a known deformation profile $h(\mathbf{r})$, the strain associated pseudomagnetic field $\mathbf{B} = \nabla \times \mathbf{A}$ can be estimated directly from $h(\mathbf{r})$. We can see from the vector potential Eqs. (3.35) that $\mathbf{B}$ points in the z direction. Its intensity is shown in Fig. 3.11.

It was found that the spatial autocorrelation function of the field B_{int} has a six-fold symmetry in absence of in-plane deformations exihibiting the graphene hexagonal lattice characteristics survives disorder averaging[72]. There is still room for the inclusion of in-plane deformations in these studies and will be addressed in this work in the future.

3.4.2 The effective field due to strain

The external magnetic field can be accounted for in the tight-binding model by Peierls substitution[8]. Let us consider first the case of a general external $3D$ magnetic field $\mathbf{B} =$

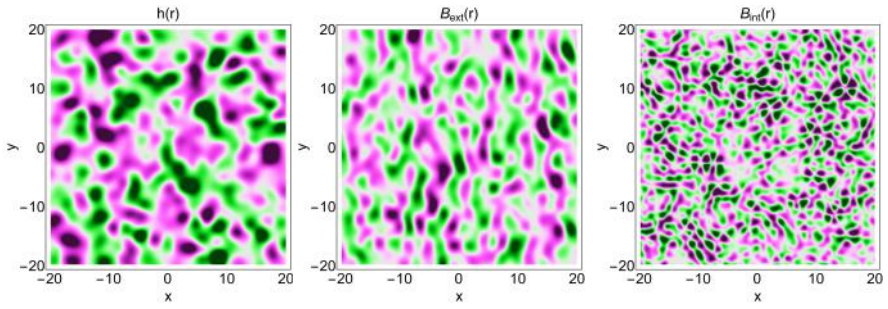

Fig. 3.11 An example of realization of the deformations $z = h(r)$ and the resulting intrinsic pseudomagnetic field B_{int} neglecting in-plane deformations. The extrinsic effective perpendicular field B_{ext} due to the applied parallel field.

(B_x, B_y, B_z) applied to a rippled graphene sheet placed along the xy-plane with arbitrary deformations. For a uniform magnetic field $\mathbf{B}$, the vector potential can be written as[89]:

$$\mathbf{A}(\mathbf{r}) = \frac{1}{2}\mathbf{B} \times \mathbf{r}. \tag{3.36}$$

which can be read as a linear combination of several possible gauges. Choosing the more convenient one, $\mathbf{A}(\mathbf{r}) = (B_y z, B_z x, B_x y)$ from where one can readily verify that $\mathbf{B} = \nabla \times \mathbf{A}$, we calculate the hopping complex phase between sites k, k', that is $t_{k,k'} = t_0 e^{i\phi_{k,k'}}$ using the Peierls substitution formula[8]:

$$\phi_{k,k'} = \frac{e}{\hbar}\int_k^{k'} \mathbf{A}(\mathbf{r}) \cdot d\mathbf{r}. \tag{3.37}$$

To integrate, we consider the magnetic flux path integral over an arbitrary straight path $\mathbf{r}(t) = \mathbf{r}_k + t(\mathbf{r}_{k'} - \mathbf{r}_k)$ where $\mathbf{r}(t) = (x(t), y(t), z(t))$ and $t \in [0,1]$. The resulting Peierls phase is:

$$\phi_{k,k'} = \frac{e}{\hbar}\left\{ B_y(x_k - x_{k'})\frac{(z_{k'} + z_k)}{2} + B_z(y_k - y_{k'})\frac{(x_{k'} + x_k)}{2} + B_x(z_k - z_{k'})\frac{(y_{k'} + y_k)}{2} \right\}. \tag{3.38}$$

For a uniform field in z direction $\mathbf{B} = B_z\hat{\mathbf{z}}$, the magnetic phase $\phi_{k,k'}$ is independent of the z component of sites positions, namely:

$$\phi_{k,k'}(\mathbf{B} = B_z\hat{\mathbf{z}}) = \frac{eB_z}{\hbar}(y_k - y_{k'})\frac{(x_{k'} + x_k)}{2} \tag{3.39}$$

This means that for the model of z displaced atomic positions, given in Eq. (3.32), the magnetic field is not affected by the deformations as expected from a Lorentz force. Thus, to account for the effect of deformations on an external field as a whole, one needs to resolute to

(i) include components of the external field other than B_z and/or (ii) find the correct in-plane displacement of atoms. Next, we discuss the two cases.

The in-plane magnetic field

Now, let us consider an external magnetic field $\mathbf{B}_{\parallel}$ parallel to the plane $z = 0$ over which the graphene sheet is deposited.

Due to ripples, the local magnetic field component perpendicular to the surface is:

$$B_{ext}(\mathbf{r}) = -\mathbf{B}_{\parallel} \cdot \hat{\mathbf{n}}(\mathbf{r}) \tag{3.40}$$

where $\hat{\mathbf{n}}(r)$ is the field of normal vectors perpendicular to the surface of atoms. In a discrete surface of equation $f(x_i, y_i, z_i) = C$, each point $\mathbf{r}_i$ has N_i neighboring points $\mathbf{r}_{i_1}, r_{i_2}, \cdots, \mathbf{r}_{i_{N_i}}$. We are interested in the differences $\Delta\mathbf{r}_{i,j} = \mathbf{r}_i - \mathbf{r}_{i_j}$ of each point with its neighbors $\Delta\mathbf{r}_{i,1}, \cdots, \Delta\mathbf{r}_{i,N_i}$. Making sure that the neighbors are indexed in the counterclockwise order, the normal vector $\mathbf{n}_{ij}$ to the surface spanned by each trio of vector positions $\mathbf{r}_i, \mathbf{r}_{i_j}, \mathbf{r}_{i_{j+1}}$ is given by:

$$\mathbf{n}_{ij} = \frac{\Delta\mathbf{r}_{i,j+1} \times \Delta\mathbf{r}_{i,j}}{|\Delta\mathbf{r}_{i,j+1} \times \Delta\mathbf{r}_{i,j}|} \tag{3.41}$$

where j should vary cyclically through the set $1, \cdots, N_i$. Finally, the normal vector to the surface at each point $\mathbf{r}_i$ will be the average of all individual normals of surface-trios:

$$\mathbf{n}_i = \frac{1}{N_i} \sum_{j=1}^{N_i} \mathbf{n}_{ij} \tag{3.42}$$

Then, the magnetic field is projected over this normal vector field using equation (3.40) and the components obtained in the normal direction can be inserted in the general equation (3.38). This method of normal vectors could be improved using an interpolation algorithm for the surface of points.

In-plane deformations of a graphene membrane deposited on a substrate

For the weak localization theory to work as probe for the deformations in the disordered graphene we need to specify the parameters of disorder such as correlation strength ξ and maximum height z_{max}. Accordingly, the in-plane deformations of the graphene surface should preserve well-defined values for this quantities to compare the numerical simulations with the theoretical predictions.

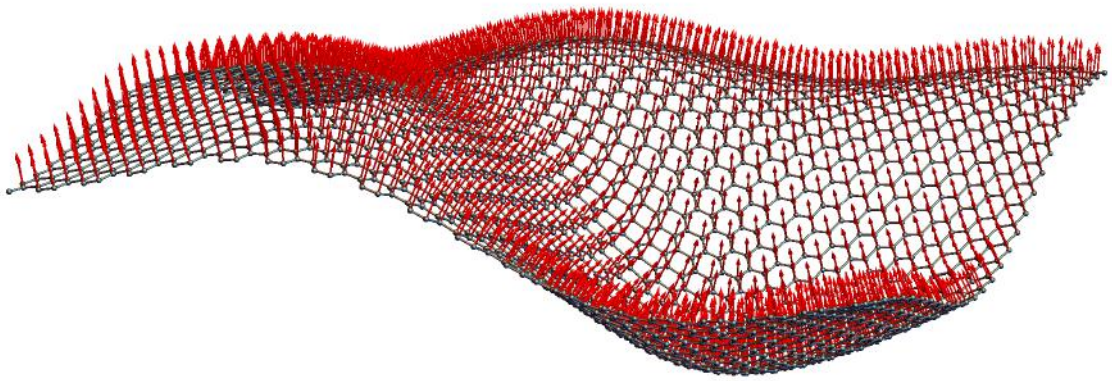

Fig. 3.12 Example of a normal vector field calculated for a rippled graphene.

To this end, we consider the model of a graphene layer $h(\mathbf{r})$ deposited over a rough substrate of a give shape $h_0(\mathbf{r})$ specified by the pair of parameters (z_{max}, ξ) but separated from the surface by a distance $d(\mathbf{r}) = h(\mathbf{r}) - h_0(\mathbf{r})$. In such case, the interaction of the membrane with the substrate competes with the carbon-carbon bonds.

The Hamiltonian that comprises the graphene deformations and interaction with the substrate is given by[87]:

$$\begin{aligned} H = & \frac{g}{2}\int d^2\mathbf{r}\,[h(\mathbf{r}) - h_0(\mathbf{r})]^2 \\ & + \frac{\kappa}{2}\int d^2\mathbf{r}\left[\nabla^2 h(\mathbf{r})\right]^2 + \int d^2\mathbf{r}\left\{\frac{\lambda}{2}\left[\sum_i u_{ii}(\mathbf{r})\right]^2 + \mu\sum_{ij}\left[u_{ij}(\mathbf{r})\right]^2\right\} \end{aligned} \tag{3.43}$$

with the material dependent bending rigidity $\kappa \approx 1eV$ and in-plane elastic constants $\mu, \lambda \approx 1eV$ of graphene[87]. The first term accounts for the graphene sheet substrate interaction and the two terms regard surface strain with the strain tensor components given by (3.33). The value of the coupling membrane-substrate g is less understood. It comprehends to different sorts of interactions between the surfaces. One could resort on an estimation of the parameters of Van der Waals interaction between graphene with an specific substrate. However, any quantity at mesoscopic scale needs to be averaged over thousands of disorder realizations and this could be a difficult practical task.

To make the model more computationally feasible, we assume this interaction as an electrostatic spring-like potential between the graphene surface $h(\mathbf{r})$ and the substrate $h_0(\mathbf{r})$ where g as the spring constant. The interaction between atoms with the surface can be

estimated by minimizing a pair-wise interaction energy between carbon atoms with the constraint that they can only move when compensating the substrate spring force. This is achievable using Molecular Dynamics energy minimization framework which would find the position of carbon atoms of minimum energy considering a parameterized pair-wise potential between carbon atoms under a fictitious external attractive force. A similar approach has been successfully applied to a suspended graphene kirigami stretched in one direction where the authors estimated the conductance for different values of a parameterized deformation[90].

3.5 Results and Discussions

We used the Kwant package to built lattice Hamiltonians according to the disorder models presented in the previous sections and calculate the magnetoconductance using the Landauer formula $G = \frac{2e^2}{h} Tr\left\{\mathbf{t}^\dagger \mathbf{t}\right\}$. We consider graphene samples of width and length $W \approx L \approx 70a$ for our tests. The sample is connected to two semi-infinite leads of square lattice representing discretized metallic contacts similarly to quantum wires of a bi-dimensional electron gas. They are coupled to the zig-zag edges of graphene following the contact model provided in the literature[91]. This scheme allow us to compare our results with previous weak localization studies present in the literature[75]. The hopping and lattice parameters considered are $t = 2.7eV$ and $a = 2.46$Å. We consider the presence of an external magnetic field B perpendicular to the sample accounted by the Peierls substitution formula (3.39). The magnitude of B is expressed in terms of the magnetic flux taken through the whole sample area in units of magnetic flux quantum ϕ_0. In order to account for the effect of the magnetic field to the metallic leads, we choose a gauge that increases in y but is x-independent, and include Peierls substitution also in the leads hopping integrals.

3.5.1 Magnetic field intensity decaying in leads region

We consider a set of samples of same size in that the calculated conductance is taken from a point away from the central region subjected to a magnetic field with intensity decaying in the lead region as $|\mathbf{B}| = |\mathbf{B}_0| e^{-(x-x_0)^2/2\sigma_B^2}$ where $x_0 = \pm L/2$ is the positions of the interfaces between lead and graphene sample (see Fig. 3.14). We can verify in figure 3.15 that the tail inclination is changing with the field range σ_B over the leads region.

Now, we consider onsite disordered graphene nanoribbon with an applied perpendicular field B_z without ripples. We used the dimensionless disorder strength of $K = 4$ and Gaussian correlation length of $\sigma = a$ which can be considered as a short ranged disorder. Differently from Anderson model of section 3.3, we use a small impurity density $n_{imp} = 0.03$, that is,

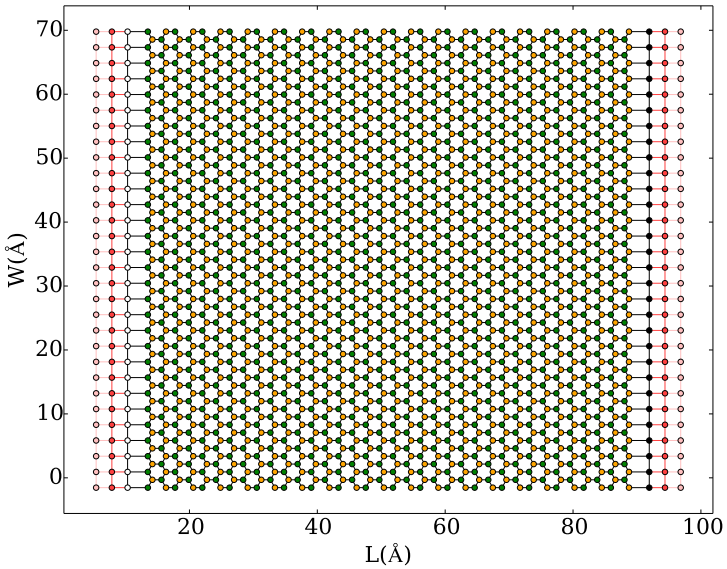

Fig. 3.13 Example of a graphene nanoribbon with armchair edges coupled to square lattice leads.

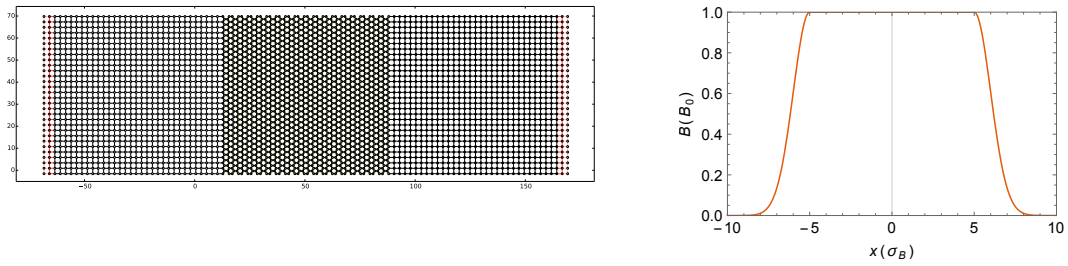

(a) (b)

Fig. 3.14 (a)System considered to the inclusion of a decaying magnetic field at the leads region (black square lattice for right lead and white square lattice for left lead). Leads are of the same size as he central region. (b) Example of the profile of the $B(x)$ curve for a region of length $L/\sigma = 10$.

3% of the total number of sites contains a localized impurity. We observe a typical weak localization curve for this set of parameters (see figure 3.5.1).

We note that it is possible to fit the data with the predicted curve presented in Eq. (3.26) for a class of parameters. A careful analysis of the fitted parameters is still under development. We can observe that the curve has a non-monotonic behavior in agreement with experimental results[84].

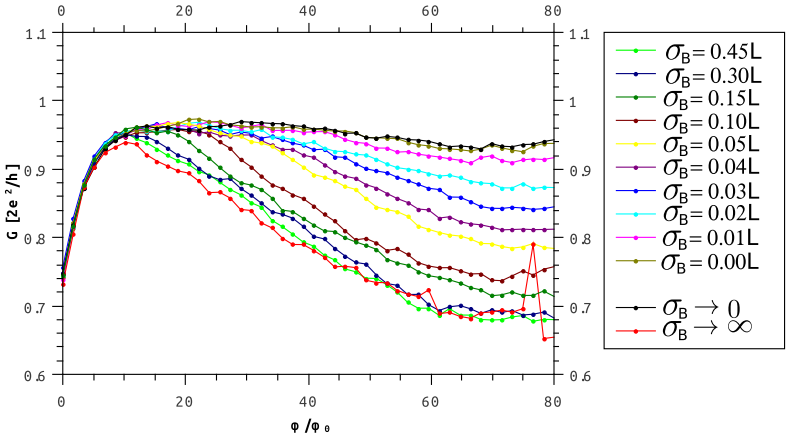

Fig. 3.15 Magnetoconductance with decaying magnetic field at the edges for different correlation lengths σ_B as funcion of L

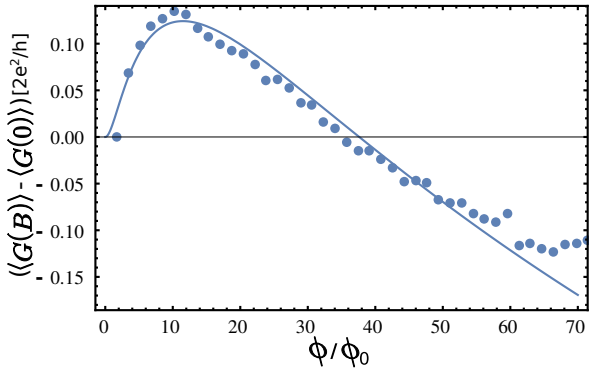

Fig. 3.16 Magnetoconductance for a graphene nanoribbon with only onsite disorder with a fitted curve. Parameters used are mentioned in the text.

3.5.2 WL-WAL crossover in the absence of strain

Now, we show the magnetoconductance calculated for different values of disorder strength ranging from $K = 0.5$ to $K = 4$ for two values of correlation length of $\sigma = 1.33a$ and $\sigma = 2.58a$. We verify a WL-WAL crossover for this set of disorder strengths. We see that an increase in the correlation length leads to greater values of WAL quantum corrections at zero B. The curves shows a tendency of converging the same conductance until the half of the curve but start to get separated after this points. This increasing difference between curves for fields higher than $\approx 15\phi_0$ is under discussion.

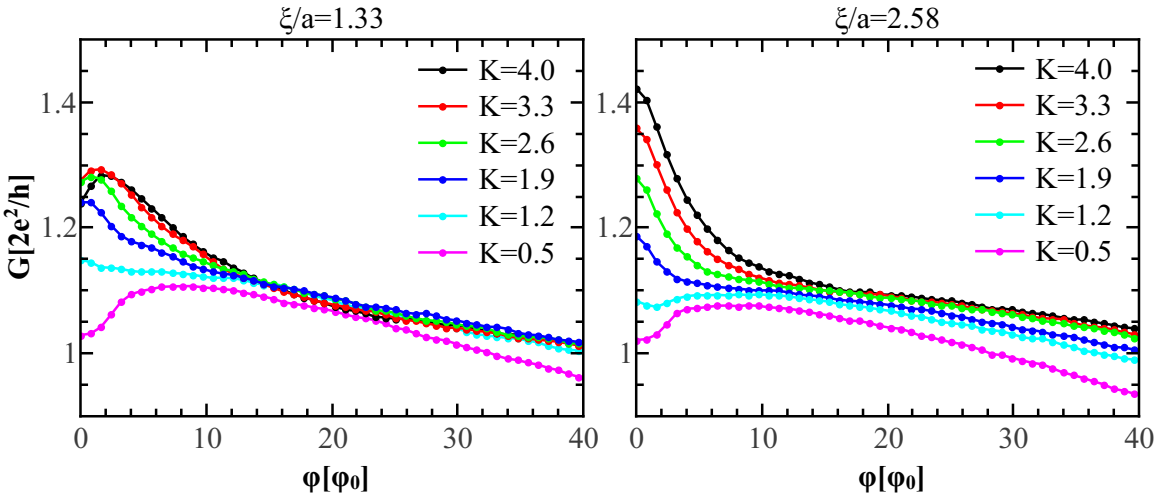

Fig. 3.17 Magnetoconductance for different values fo onsite disorder strength K and two correlation lengths $\sigma = 1.33a$ (left) and $\sigma = 2.58a$ (right).

3.5.3 The effect of an in-plane magnetic field on the WL curve

To simulate ripples, we consider the maximum height as $z_{max} = 3a$ while a correlation length of $\xi = 10a$ which means that $z_{max}/\xi = 30\%$. The ripple density considered is also $n_{imp} = 0.03$. The onsite disorder is also present and has the same values for $\sigma = 1$ and $K = 4$ as considered in the calculations of conductances of figure 3.5.1.

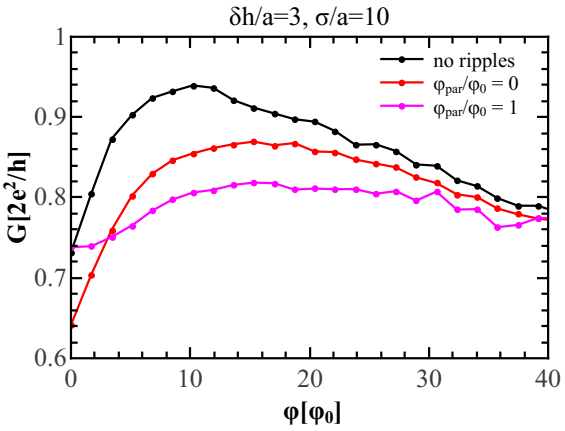

Fig. 3.18 Magnetoconductance for a graphene sample with only onsite disorder (black), with ripples (red) and with ripples and a parallel magnetic field (pink).

Including rippling, wee see that the whole curve is decreased at zero magnetic field until its maximum value but converges to the same value as the perpendicular field is increased.

Now, we study ripples in graphene by the inclusion of an in-plane magnetic field using the methods described in last section. For now, units of the parallel magnetic flux are for a different normalized magnetic flux quantum φ_0 and will be quantitatively discussed later. We can see that the inclusion of ripples causes a smoothing in the conductance (see black and red curves of picture 3.18) in a similar way as observed in experiments (figure 3.6). The in-plane magnetic field causes a phase oscillation over the surface that is proportional to the height of the deformations and causes a phase coherence breaking that suppress quantum interference contributions. In-plane magnetic field is suppressing the weak-localization effect by breaking coherent phases even for small values of the perpendicular magnetic field. Another example can be verified in smaller Gaussians of height $z_{max} = 1a$ pictured in (3.19). As a next step, we should investigate the effect quantitatively and the angular dependence of this suppression and verify anisotropic effects compared to theoretical models[72].

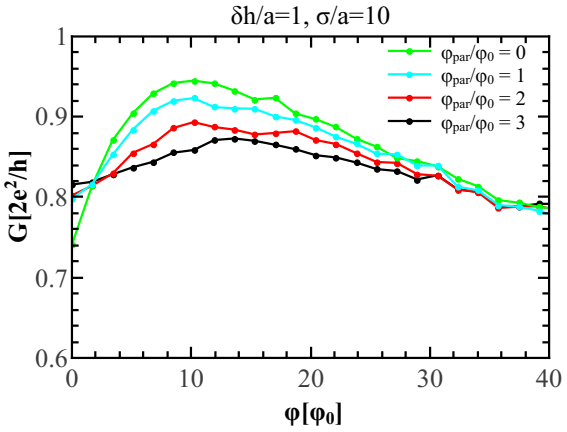

Fig. 3.19 Magnetoconductance for some values of in-plane magnetic field in units of φ_0.

3.6 Conclusions

We discussed the problem of weak localization curves of a graphene nanoribbon coupled to metallic leads for two kinds of disorder, onsite and hopping integral disorder. The former has been shown that for long range correlation length, conductance increases even for the stronger disorders as a result of the weak anti-localization mechanism. The latter cause a suppression to the conductance due to the pseudomagnetic field generated by the strain. More calculations are necessary to quantify the effects.

Additionally, we discussed the effects of ripples in the model and how the application of an in-plane field could be added to the problem to probe effects of graphene deformations to the weak localization curve. We also considered the study of in-plane relaxations in graphene

considering the interaction with a substrate. The in-plane relaxations could account for more realistic deformations in graphene surfaces. We expect that the inclusion of in-plane deformations makes rippled graphene samples to be affected by perpendicular magnetic field and also account for more precise pseudomagnetic field contributions. In some situations, the pseudomagnetic field could be overestimated in the absence of in-plane relaxations due to highly sloped regions on the surface. This could be a drawback to the modeling of highly sensible quantities extracted from strained surfaces such as the weak localization.

Chapter 4

Application II: Quantum phase transitions in the anomalous quantum Hall effect of graphene

One of the most interesting features reported in the first seminal graphene papers [92–94, 1] is the anomalous Quantum Hal effect. As discussed in the previous chapter, graphene has a unique band structure whose charge carrier wave-function can be effectively represented by a four-component relativistic-like spinorial behavior. As a consequence, the quantum Hall effect in graphene shows unusual features. Due to graphene sublattice pseudospin degree of freedom, current in graphene allows for transport of both electrons and holes causing quantized Hall conductance for negative and positive charges. When sublattice symmetry is preserved, the quantum Hall effect is also electron-hole symmetric. Graphene valley isospin degree of freedom causes the Hall conductivity quantum to be four-fold degenerated, two from the electron intrinsic spin and two from the K and K' degeneracy. Such degeneracy has been associated with graphene's momentum inversion symmetry[73].

In the past decade, triggered by the discovery of the anomalous quantum Hall effect in graphene[92], several theoretical studies have been devoted to understand the graphene quantum Hall physics. In particular, it has been predicted that the disorder plays a central role in the transport characteristics of graphene in the quantum Hall regime [95]. In summary, theory predicts that the quantized Hall plateaus could be affected in two main categories: (i) the anomalous Hall effect could transit to the normal Hall effect by displaying steps of two-fold spin degenerated Landau levels and (ii) a plateau at zero energy could emerge. Despite some evidences of level splittings and a plateau at zero Hall conductivity have been found experimentally, an explanation for such remains incomplete. In Ref.[96], the emergence of new plateaus has been attributed to Zeeman splitting, despite this effect being known as weak

in graphene. Alternatively, Ref.[97] argued that electron-electron interaction are responsible for degeneracy breaking and, as a consequence, for the level splitting observed in graphene in the quantum Hall regime[98]. However, due to the lack of information about which kind of disorder scatterings is the dominant one, it is difficult to attribute such findings to the particular cases of disorder symmetries discussed in literature[79].

It has been established that the quantum Hall effect in two-dimensional electron gas (2DEG) systems implies in localization effects. In the quantum Hall regime, the density of states is characterized by discrete peaks called Landau Levels (LL). These peaks are broaden by the disorder. The states that are in the tails of the LL are localized in the bulk and the ones close to the center of the LL peak are fully delocalized, displaying critical behavior[99]. At zero temperature, when the Fermi energy is tuned through the critical energies, the system undergoes a quantum phase transition[100]. The set of disorder-driven quantum phase transition are known as Anderson transitions, where the localization length at the critical points E_c is characterized by the power-law divergence $\xi \sim |E - E_c|^{-\nu}$, with a critical exponent ν. This exponent is not directly assessed by transport experiments, however, it can be related to the temperature dependence of the phase coherence length $l_\phi \sim T^{-p/2}$ where $p = 2$ for graphene[101]. According to finite size scaling theory[102], the power-law behavior of the magneto-conductivity tensor at this transition has also the parameter scaling:

$$\sigma_{\alpha\beta} \sim l_{eff}^{1/\nu}(B - B_c) \tag{4.1}$$

where B_c is the critical magnetic field and l_{eff} is the effective system size. At zero temperature $l_{eff} \to L$ and at nonzero temperatures $l_{eff} \to l_\phi$[103]. Therefore, one can write the temperature dependence of the critical behavior of the conductivity tensor as:

$$\max\left(\frac{d\sigma_{xy}}{dB}\right) \sim T^{-\kappa}, \qquad \Delta\sigma_{xx} \sim T^{-\kappa} \tag{4.2}$$

where $\kappa = -p/2\nu$. Indeed, the diagram of σ_{xy} versus σ_{xx} as function of temperature shows universal features for $2DEG$ systems under quantum Hall regime[104]. It was shown that σ_{xy} and σ_{xx} are not independent and follow a scaling behavior over one parameter changing. Also, a temperature-driven flow diagram towards $(\sigma_{xx}, \sigma_{xy}) = (0, n)e^2/h$ where n is an integer has been observed[105]. However, there is an experimental difficulty to obtain reliable flow diagrams close to the transition region between Hall plateaus due to the sensitivity of delocalized states to sample inhomogeneities. A detailed analysis has demonstrated that Hall plateaus follows mathematical phase diagrams with modular symmetry[106] and at quantum critical points, where states are delocalized, corresponds to unstable fixed points

while plateau states are represented by stable fixed points of the flow. The Renormalization Group (RG) flow obtained from the nonlinear σ model [104] is able to explain the flow stability, but falls short on providing quantitative predictions. Therefore, a numerical analysis is the most promising tool to associate the flow diagrams to disorder.

In graphene, a σ model taking into account isospin degeneracies and nonzero magnetic field containing two independent sectors corresponding to two valleys has been derived[95]. It was shown that for decoupled and weakly mixed valleys, the flow diagrams displays very different features from 2DEG systems (see Fig. 4.1). As discussed in chapter 3, the coupling between sublattices ad valleys can be tuned by the disorder properties. Despite the importance of such class of systems, few numerical studies have addressed the longitudinal and transverse resistances in Hall bar geometries due to the lack of an efficient multi-terminal electronic transport code.

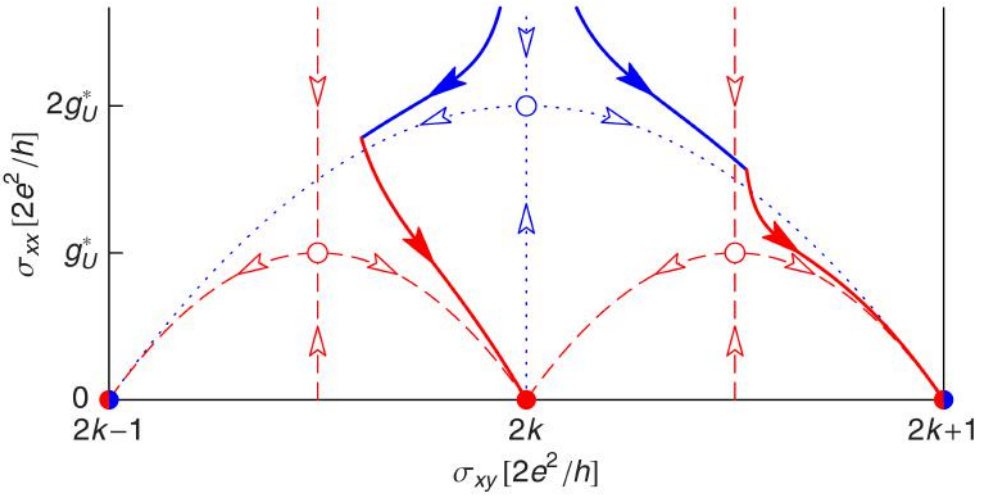

Fig. 4.1 Theoretical Renormalization Group flow of the σ_{xx} and σ_{xy} diagram for graphene with (red) and without (blue) valley mixing. The unstable fixed points (open circles) correspond to transition states between Hall plateaus. Stable points (closed circles) correspond to the Hall plateaus states. Solid lines are transition between different Hall regimes in graphene as predicted in Ref. [95]. $g^*{}_U$ is the longitudinal conductivity for the quantum Hall effect in an ordinary material. Figure adapted from Ref. [95].

In this chapter, we numerically study the longitudinal and Hall conductivities of disordered graphene samples for both chiral and scalar disorder. To this end, in section 4.1, we revise the theory of the quantum Hall effect in disordered graphene systems at low energy. In section 4.2, we derive the conductivity and resistivity tensors at nonzero temperature for a six-terminal system. In section 4.3, we discuss the effect of temperature on the conductivity

curves and display the numerically obtained temperature-driven flow diagrams for graphene. In section 4.4, we draw our conclusions.

4.1 Theoretical background

Here, we review the theory of the anomalous quantum Hall effect in graphene in the continuum limit. Next, we address the effect of disorder in the quantum Hall regime in the context of localization theory. Finally, we discuss the effect of different types of disorder scattering to the anomalous Hall effect in graphene.

4.1.1 The anomalous quantum Hall effect

The quantum Hall effect is universally characterized by quantized plateaux in the transverse conductivity in multiples of e^2/h. The key ingredient to differentiate the quantum Hall effect in graphene from the usual effect in $2DEG$ samples is the relativistic-like nature of the charge carriers close to charge neutrality point. In this section, we discuss the continuum model for the graphene electronic band structure under a strong magnetic field and low doping, where one can successfully describe the electrons by Dirac Hamiltonian for massless particles.

We start this derivation by considering the Hamiltonian of a pristine graphene near the charge neutrality point, Eq. (3.11):

$$H = -\hbar v_F \zeta_z \otimes \boldsymbol{\sigma} \cdot \mathbf{k} \tag{4.3}$$

where only the linear term is taken into account. The coupling of the electrons to a perpendicular magnetic field can be accounted for by the substitution[107]:

$$\boldsymbol{\Pi}/\hbar = \mathbf{k} + e\mathbf{A}/\hbar \tag{4.4}$$

which is valid always that the characteristic magnetic length $l_B = \sqrt{\hbar/eB}$ is much larger than the lattice spacing a and $\mathbf{A}$ is sufficiently smooth, such that the Dirac Hamiltonian (continuum limit) is a meaningful approximation.

Substituting $\boldsymbol{\Pi}$ into Eq.(4.3), it is convenient to write the Hamiltonian in terms of a pair of conjugate operators[108]:

$$\hat{a} = \frac{l_B}{\sqrt{2}\hbar}\left(\Pi_x - i\Pi_y\right), \qquad \hat{a}^\dagger = \frac{l_B}{\sqrt{2}\hbar}\left(\Pi_x + i\Pi_y\right) \tag{4.5}$$

which satisfies the normalized commutation relation:

$$[\hat{a}, \hat{a}^\dagger] = 1. \tag{4.6}$$

The low-energy Hamiltonian under magnetic field becomes:

$$H_B = \frac{\sqrt{2}\hbar v_F}{l_B} \zeta_z \otimes \begin{pmatrix} 0 & \hat{a} \\ \hat{a}^\dagger & 0 \end{pmatrix} \tag{4.7}$$

In the subspace of each valley, the eigenproblem $H_B \psi_n = \varepsilon_n \psi_n$ with $\psi_n = (u_n, v_n)^T$ becomes a set of two coupled equations:

$$\hat{a} v_n = \frac{l_b}{\sqrt{2}\hbar v_F} \varepsilon_n u_n \tag{4.8}$$

$$\hat{a}^\dagger u_n = \frac{l_b}{\sqrt{2}\hbar v_F} \varepsilon_n v_n. \tag{4.9}$$

Each one can be transformed into an one-dimensional harmonic oscillator problem whose eigenvalues can be readily obtained:

$$\varepsilon_n^\pm = \pm \frac{\hbar v_F}{l_B} \sqrt{2n} \tag{4.10}$$

where $\pm$ stands for two possible solutions, a positive and a negative, for each n. The eigenenergies $\varepsilon_n^\pm$ correspond to the quantized Landau energy levels for the Dirac Hamiltonian under a magnetic field. Due to the two-fold degenerated valley spectrum, the level density acquires a global factor of 2. Also, another factor of 2 must be taken into account for sufficiently low magnetic fields, when Zeeman splittings are negligible. It is worth mentioning how the dispersion relation in graphene $\varepsilon_n \sim \sqrt{Bn}$ differs from the quantum Hall effect in standard 2D electron systems, namely $\varepsilon_n \sim Bn$. Due to the linear dependence in the latter case, energy intervals ΔE are independent of n (for a review, see Refs. [109, 110]).

The corresponding eigenvectors are:

$$\psi_n^\pm = \frac{1}{\sqrt{2}} \begin{pmatrix} |n-1\rangle \\ \pm |n\rangle \end{pmatrix} \tag{4.11}$$

whose components follow the usual harmonic oscillator properties $\hat{a}|n\rangle = \sqrt{n}|n-1\rangle$ and $\hat{a}^\dagger|n\rangle = \sqrt{n+1}|n+1\rangle$ for $n > 1$. An extra attention should be given to the ground state

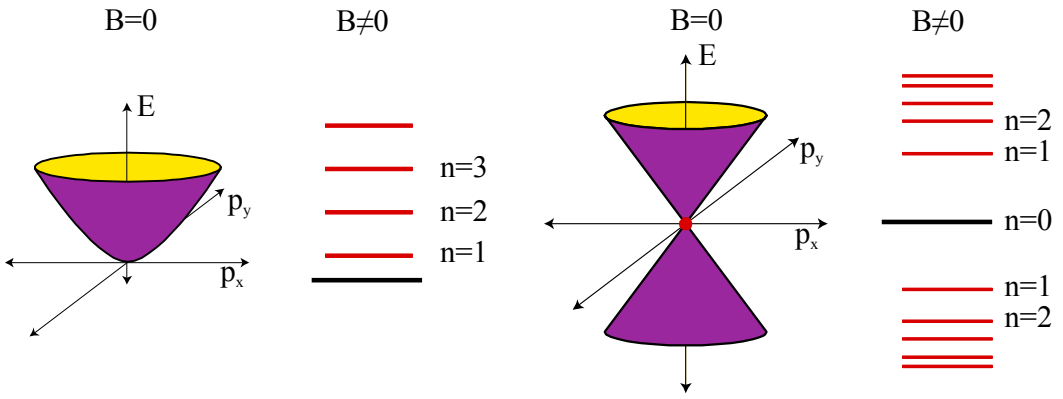

Fig. 4.2 Comparison of band structure and Landau level spacings for a semiconductor (left) and graphene (right)

$n = 0$, where $\hat{a}|0\rangle = 0$ and $\varepsilon_0 = 0$. In this case, the spinor ψ_0 becomes:

$$\psi_0 = \begin{pmatrix} 0 \\ |0\rangle \end{pmatrix} \tag{4.12}$$

The nonzero term correspond to the A sublattice in the K valley and to the B sublattice in the K' valley. In this case, scalar disorder is ineffective to cause intervalley mixing, making the scattering purely intravalley to this state, as verified in Ref. [111]. Also, as noted in Ref.[112], the Landau levels at energy ε_0 are independent of the magnetic field intensity.

The $k-$independence of the Landau levels leads to another degeneracy: there are $= n_B A$ states for each n, where $n_B \equiv 1/2\pi l_B^2$, which comprehends to ratio between the irreducible area of a single Landau level $1/n_B$ and the area of the sample A. Also, $n_B A = \phi_A/\phi_0$, where $\phi_A = BA$ is the magnetic flux over the area A and ϕ_0 is the magnetic flux quantum. The area n_B^{-1} is independent of n and any particle will contribute to the same area. Therefore, an electronic density of n_e should give a filling factor of $\nu = \frac{n_e}{n_B}$. One can compare graphene's filling factor to the usual quantum Hall effect (see Fig. 4.5a). By filling the available states in the conducting band of a 2DEG, the filling factor becomes $\nu_{2DEG} = 2n$, where 2 stands for spin degeneracy, while graphene, which comprehends to available states also in the valence , the filling factor is given by $\nu_G = 2(2n+1)$ where the second factor of 2 stands for valley degeneracy. Therefore, at $n = 0$, there is exactly one Landau level with 2 states, one spin-up and one spin-down.

The quantum Hall effect is a macroscopic manifestation of Landau level degeneracy. From the classical mechanics point of view, one can calculate the conductivity tensor of a 2D conductor of length L and width W under an electric field $\mathbf{E} = E\hat{\mathbf{x}}$ and magnetic field $B = B\hat{\mathbf{z}}$ (see Fig. 4.3). The field $\mathbf{E}$ accelerates the charges on the plane along the x direction

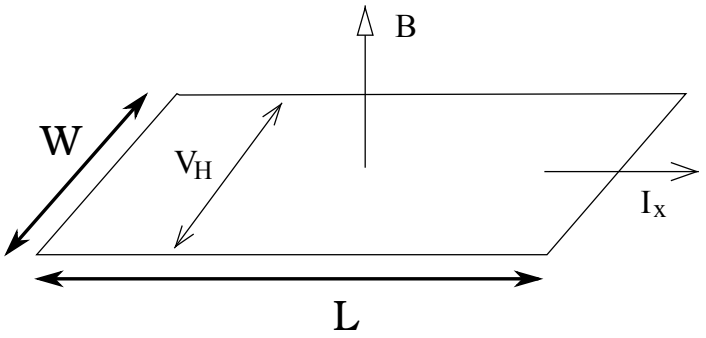

Fig. 4.3 Schematics of the Hall effect. An electric current I_x is passing through a 2D conductor of length L and width W with a perpendicular magnetic field B.

resulting in the current I_x. The magnetic field $\mathbf{B}$ bends the current towards the y direction due to the Lorentz force causing a voltage drop of V_H which can be associated to a perpendicular component of the electric field $E_y = V_H/W$. In the Drude model, charges are deaccelerated by a linear friction term $m\mathbf{v}/\tau$, where m is the electronic mass, τ is the mean free time. Therefore:

$$m\frac{d\mathbf{v}}{dt} = -e\mathbf{E} - e\mathbf{v}\times\mathbf{B} - \frac{m\mathbf{v}}{\tau}. \tag{4.13}$$

The equilibrium solution $\left(\frac{d\mathbf{v}}{dt} = 0\right)$ gives:

$$\mathbf{E} = \frac{m}{\tau n e^2}\begin{pmatrix} 1 & \tau\frac{eB}{m} \\ -\tau\frac{eB}{m} & 1 \end{pmatrix}\mathbf{J}. \tag{4.14}$$

Using Ohm's law $\mathbf{E} = \rho\mathbf{J}$, one obtains the resistivity components:

$$\rho_{xx} = \frac{m}{\tau n_e e^2}, \qquad \rho_{xy} = \frac{B}{n_e e}. \tag{4.15}$$

From the resistivity tensor in the classical Hall regime, one can observe that ρ_{xy} is insensitive to the scattering processes that causes τ, while $\rho_{xx} \to 0$ when $\tau \to \infty$ (see Fig. 4.4). From the quantum mechanics point of view, the charge density n_e is filled with particles that occupy an incompressible area n_B^{-1}. Hence, when a gate voltage causing a carrier density n_e electrons in graphene, if n_e is an integer multiple of n_B, than the conductance is suddenly increased by an integer factor responsible to the observed conductance quantization in the Hall effect.

From graphene's filling factor $n_e = 2(2n+1)n_B$, we obtain the quantized Hall transverse resistance in graphene:

$$\rho_{xy} = \frac{h}{2e^2}\frac{1}{2n+1} \tag{4.16}$$

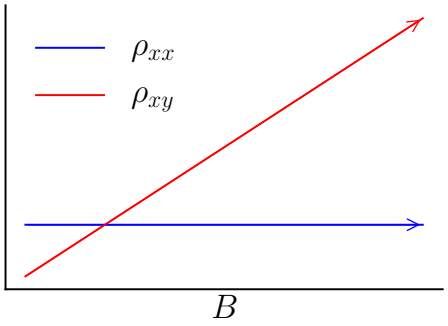

Fig. 4.4 Classical longitudinal ρ_{xx} and transverse ρ_{xy} resistivity derived from Drude model.

i.e., the inverse of odd multiples of the conductance quantum $g = 2e^2/h$, as observed experimentally (see Fig. 4.5b). Note that, differently from the classical picture, the quantum Hall conductivity is independent of the magnetic field.

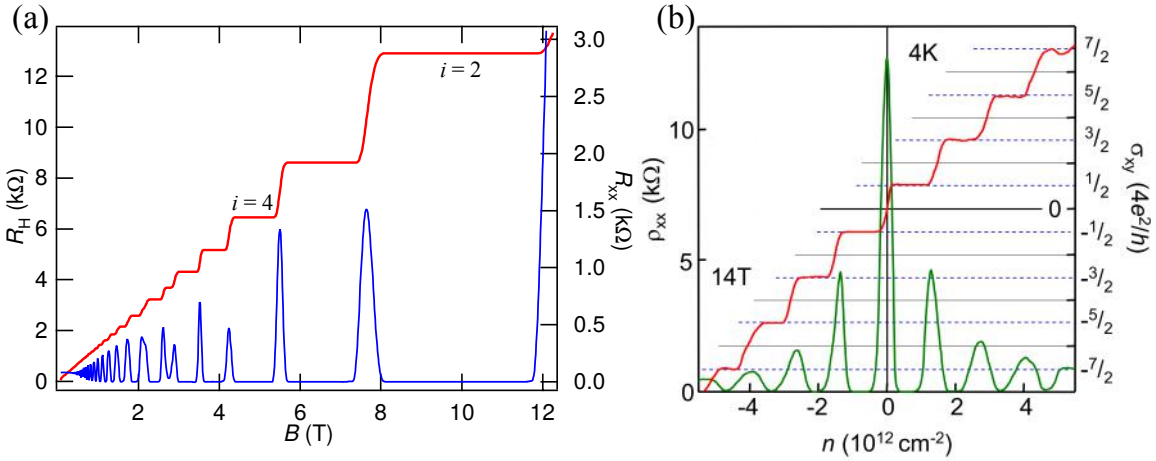

Fig. 4.5 (a) Integer quantum Hall effect: experimental measurements of Hall and longitudinal resistances as function of the magnetic field B for a 2DEG at the interface of a GaAs/AlGaAs heterostructure at temperature $0.1K$. Adapted figure from Ref.[113]. (b) Anomalous quantum Hall effect: experimental Hall conductivity σ_{xy} and longitudinal resistivity $\rho_{x}x$ in graphene as a function of charge concentration n for $B = 14T$. σ is calculated from measurements of the tensor ρ. Adapted figure from Ref.[93].

In the longitudinal resistance, the Drude's scattering term is not adequate to model coherent scattering processes and would lead us to $\rho_{xx} \to 0$. In the next section, we discuss the effects of disorder in the quantum Hall effect in the diffusive regime.

4.1.2 The effect of disorder on the Landau Levels

To the quantum Hall effect take place, the translational invariance symmetry has to be broken[108]. The translational symmetry in Hall bar geometries can be broken even by impurity scattering or by the sample finiteness. In particular, disorder breaks levels degeneracy by causing spatial-dependent fluctuations to n_B^{-1} and causes a finite width to the levels density, associated to the disorder intensity (see Fig. 4.6).

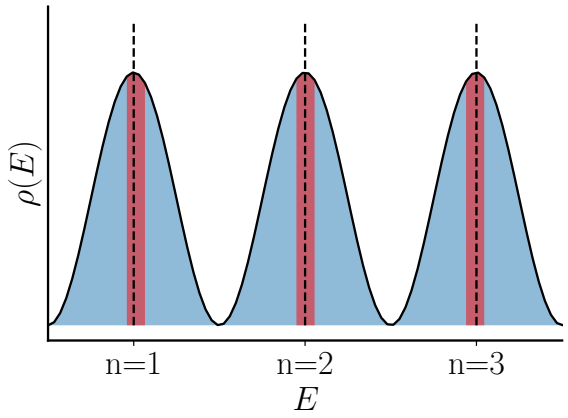

Fig. 4.6 Density of states of Landau Levels broaden by disorder. Bue region The peaks displays levels broaden by disorder (blue). The vertical dashed lines are the respective energies E_n of the levels. Vertical bars (red) shows the energy intervals of extended states.

For a two-dimensional conductor in diffusive regime, the scaling theory of localization predicts that all systems behave as insulating - vanishing of conductivity while lowering temperature - as a consequence of interference effects. However, since the magnetic field breaks the time-reversal symmetry, due to disorder the area-dependent coherent phases tends to average out. Therefore, under a strong magnetic field, the conditions for applying the standard localization theory are violated and a nonzero current are usually observed. This is the case for the quantum Hall effect in disordered samples, where both insulating-conducting phases coexist. In the insulating phase, where $\sigma_{xx} = 0$, all electronic states are localized and the filling factor is far from the Landau levels. From the other hand, in the conducting phase $\sigma_{xx} \neq 0$ and all states are extended, while the filling factor is at the top of a Landau level. The critical energy associated to the filling factor value that separates the extended states from the localized ones is defined as mobility edge. The existence of a metal-insulator transition at a critical energy with mobility edges characterizes the quantum Hall effect as a disorder-driven quantum phase transition and universal critical properties are expected.

As demonstrated in the previous chapter, the different sources of disorder in graphene couple isospin and pseudospin degrees of freedom in several ways. While the observed

$\sigma_{xy} = 0$ in graphene is due to preserved sublattice symmetry, the anomalous Hall quantization accounts for a disorder that preserves valley symmetry.

In this sense, several theoretical models have been proposed to explain the anomalous Hall quantization and predict different kinds of symmetry breaking. Here, we discuss what has been predicted in literature and propose numerical tests to verify four special cases: the chiral long-range disorder, the chiral short-range disorder, the scalar long-range disorder and the scalar short-range disorder.

4.1.3 Intervalley *vs* intravalley scatterings in the QHE of graphene

Here we discuss the short and long range, scalar and chiral disorder effects in graphene in the quantum Hall regime (see discussion in section 3.1.4).

The short-range scalar disorder causes intra-lattice scatterings. In the four-component (AK, BK, BK', AK') matrix notation, the associated matrix to a scatterer on a site of sublattice A located at $\mathbf{R}_A$ is given by [79]:

$$V^A = \begin{pmatrix} V_0 & 0 & 0 & V_0 e^{-2i\mathbf{k}_0\cdot\mathbf{R}_A} \\ 0 & 0 & 0 & 0 \\ 0 & 0 & 0 & 0 \\ V_0 e^{2i\mathbf{k}_0\cdot\mathbf{R}_A} & 0 & 0 & V_0 \end{pmatrix} \tag{4.17}$$

while a scatterer on B at $\mathbf{R}_B$ gives:

$$V^B = \begin{pmatrix} 0 & 0 & 0 & 0 \\ 0 & V_0 & V_0 e^{-2i\mathbf{k}_0\cdot\mathbf{R}_B} & 0 \\ 0 & V_0 e^{2i\mathbf{k}_0\cdot\mathbf{R}_B} & V_0 & 0 \\ 0 & 0 & 0 & 0 \end{pmatrix} \tag{4.18}$$

where $\mathbf{k}_0 = \mathbf{K} - \mathbf{K}'$. Regarding chiral disorder, the hopping integral that couples inter-lattice scatterings from a site at $\mathbf{R}_A$ to another one at $\mathbf{R}_B$ is associated to the matrix[111]:

$$V^{AB} = \begin{pmatrix} 0 & z_A^* z_B & z_A^* z'_B & 0 \\ z_B^* z_A & 0 & 0 & z_B^* z'_A \\ z'^*_B z_A & 0 & 0 & z'^*_B z'_A \\ 0 & z'^*_A z_B & z'^*_A z'_B & 0 \end{pmatrix} \tag{4.19}$$

where $z_A = \delta t e^{i\mathbf{K}\cdot\mathbf{R}_A}$, $z_B = \delta t e^{i\mathbf{K}\cdot\mathbf{R}_B}$, $z'_A = \delta t e^{i\mathbf{K}'\cdot\mathbf{R}_A}$ and $z'_B = \delta t e^{i\mathbf{K}'\cdot\mathbf{R}_B}$ and δt is the hopping linear distortion term. Note that matrices (4.17), (4.18) and (4.19) complements each other.

Using the graphene quantum Hall wave functions derived in the previous section, Ref. [111] calculated the matrix elements of the quantum Hall states coupled by disorder, namely, $\psi_n^\dagger V^X \psi_n$, where $X = A, B, AB$.

The authors shown that, fr $n = 0$, where the wave function amplitudes are localized in one of the sublattices per valley, pure onsite disorder should give intravalley scatterings and pure hopping disorder should give intervalley scatterings in the short-range limit. For $n \neq 0$, both kinds of disorder should contribute to intervalley scatterings.

Another approach to the effects of the different types of disorder to the quantum Hall effect in graphene has been demonstrated in Ref.[95]. The authors attributed the disorder-driven localizations in the quantum Hall effect in graphene to the disorder symmetry and considered it as fundamental for the effect to take place. Using a self-consistent Born approximation (SCBA) and a nonlinear sigma model, they concluded that while long-range scalar disorder causes the anomalous quantum Hall effect, short-range disorder allows intervalley scattering and ordinary quantum Hall effect should be observed in this case. Moreover, a crossover from the anomalous to the ordinary effect should occur at a critical temperature. Chiral disorder should lead to a linear dependence of σ_{xy} with the charge density n_e, similar to the classical effect Eq. (4.15), around the charge neutrality point.

It should be emphasized that the Self-consistent Born approximation is based on a diagrammatic approach and, as was the case in the previous chapter, is valid when $k_F l_e \gg 1$, far from the charge neutrality point. The considerations on the $N = 0$ level of Ref. [95] based on the SCBA are speculations and, even for qualitative estimates, should be considered carefully.

In the next section, we present our methodology to study this problem numerically and compare our findings with the ones discussed above.

4.2 The conductivity tensor at nonzero temperature

In this section, we derive the conductivity tensor equations at nonzero temperature for a Hall bar geometry.

To observe the longitudinal and transverse conductivities from a given experimental setup, one needs at least four electric contacts [77]. However, in experiments using a Hall bar geometry (six-terminals), the current can be driven in two contacts while other two contacts, working as voltage probes, are places longitudinally to the current. The remaining other two contacts are perpendicularly placed. Together, the six contacts guarantee the performance of both transverse and longitudinal measurements in a noninvasive manner (see Fig. 4.7).

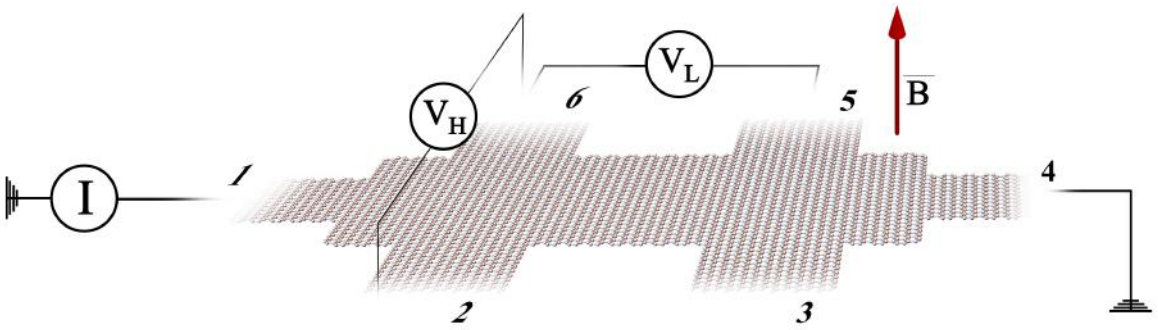

Fig. 4.7 Schematics of the description of a Hall bar. The system is considered to be in the xy plane and a magnetic field is applied in the z direction. A current I along the x axis is induced between the horizontal contacts 1 and 4, while the voltage probes at the contacts $2,6,5$ measures potential differences V_H and V_L that are used to calculate the longitudinal and transverse resistance through the relation $V = RI$.

In the linear response theory, the conductance in a multi-terminal setup can be calculated via the Landauer-Büttiker formalism. The relation between the electronic current I_α that passes through terminal α and the voltages V_β applied in terminal β is given by:

$$I_\alpha = \sum_{\beta=1}^{6} G_{\alpha\beta}(V_\alpha - V_\beta). \tag{4.20}$$

The conductance $G_{\alpha\beta}$ is obtained from the scattering matrix coefficients discussed in chapter 2. Considering electrons reservoirs with a nonzero temperature T and chemical potential μ, the conductance is related to transmission probability as:

$$G_{\alpha\beta} = \frac{2e^2}{h}\int_{-\infty}^{\infty} dE \left(-\frac{\partial f}{\partial E}\right) T_{\alpha\beta}(E), \tag{4.21}$$

where $f(E) = [1 + e^(E-\mu)/k_B T]^{-1}$ is the Fermi-Dirac distribution. Equation (4.20) gives a set of six coupled equations. We consider the case of a current applied between terminals 1 and 4, which makes $I_2 = I_3 = I_5 = I_6$ and $I_1 = -I_4 = I$, as depicted in Fig.4.7. If the magnetic field is sufficiently strong in such way that the edge states localization width is smaller than the width of the terminals bar, the Lorentz force completely deviates the electrons from a terminal to the neighboring terminalThe sense of the bending depends on the charge of the particles. leading to the vanishing of the all conductances, except the following ones:

$$G_{21} = G_{32} = G_{43} = G_{54} = G_{65} = G_{16} \equiv \bar{G} \tag{4.22}$$

where $\bar{G}$ is some conductance value. Therefore, in matrix notation, the Landauer-Büttiker reads:

$$\begin{pmatrix} I \\ 0 \\ 0 \\ -I \\ 0 \\ 0 \end{pmatrix} = \begin{pmatrix} \bar{G} & 0 & 0 & 0 & 0 & -\bar{G} \\ -\bar{G} & \bar{G} & 0 & 0 & 0 & 0 \\ 0 & -\bar{G} & \bar{G} & 0 & 0 & 0 \\ 0 & 0 & -\bar{G} & \bar{G} & 0 & 0 \\ 0 & 0 & 0 & -\bar{G} & \bar{G} & 0 \\ 0 & 0 & 0 & 0 & -\bar{G} & \bar{G} \end{pmatrix} \begin{pmatrix} V_1 \\ V_2 \\ V_3 \\ V_4 \\ V_5 \\ V_6 \end{pmatrix} \tag{4.23}$$

whose solutions are:

$$V_1 = V_2 = V_3, \quad V_4 = V_5 = V_6, \quad I = \bar{G}(V_1 - V_6), \quad I = \bar{G}(V_4 - V_3) \tag{4.24}$$

From this model, one can theoretically predict the resistance values in the quantum Hall regime. The resistances $R_{\alpha\beta,\gamma\delta}$ between contacts α and β with a current between γ and δ read:

$$R_{xy} \equiv R_{26,14} = R_{35,14} = \bar{G}^{-1} \qquad R_{xx} \equiv R_{65,14} = R_{32,14} = 0 \tag{4.25}$$

At zero temperature, $\bar{G} \to \frac{e^2}{h}\nu$ where ν is the Hall filling factor. Therefore, the transverse resistances R_{xy} display the expected quantized Hall value $R_H = \frac{h}{e^2}\frac{1}{\nu}$ while the longitudinal resistances R_{xx} vanish, as observed experimentally[77].

In the numerical calculations, one is interested in the calculation of the voltages V_α as the outputs and currents I_β as the inputs and a dense conductance matrix ahousl be considered. To this end, we define the voltages and currents as column vectors $\mathbf{V} = (V_1, V_2, V_3, V_4, V_5, V_6)$ and $\mathbf{I} = (I_1, I_2, I_3, I_4, I_5, I_6)$, respectively. In order to obtain the solution for the voltages instead of the currents, one needs to invert the conductance matrix $\mathbf{G}^{-1} \equiv \mathbf{F}$. However, due to conservation laws, the equations are linearly dependent, which means that $\mathbf{G}$ is not invertible. Hence, we skip the line and column in the conductance matrix regarding the terminal that the current leaves, say terminal δ, and solve the linear system $\widetilde{\boldsymbol{V}} = \widetilde{\boldsymbol{F}} \cdot \widetilde{\boldsymbol{I}}$ for a 5×5 matrix $\widetilde{\boldsymbol{F}}$. The solution for a current injected in terminal γ that leaves from terminal δ for $\alpha \neq \delta \neq \beta \neq \gamma$ reads:

$$R_{\alpha\beta,\gamma\delta} = \widetilde{F}_{\alpha-\Theta(\alpha-\delta),\gamma} - \widetilde{F}_{\beta-\Theta(\beta-\delta),\gamma}. \tag{4.26}$$

Here, $\Theta(x)$ denotes the discrete step function and is necessary to account for the fact that the resistance ath the left hand side considers all the terminals, and the matrix at the right hand side has one missing terminal.

It should be emphasized that, at stage of the matrix inversion, the elements of matrix **G** already carry the temperature dependence. That is to say that the thermal average Eq. (4.21) should be taken before Eq. (4.20) and, because temperature can affect the transport probabilities and change the result of the inversion, they do not commute.

4.2.1 The conductivity/resistivity tensor

As resistance and conductance are geometry-dependent, we calculate the resistivity and conductivity tensors. The resistivity tensor of a 2D system is obtained from the relation between the electric field and the linear current density:

$$E_k = \sum_{l=x,y} \rho_{kl} j_l, \qquad k = x, y \tag{4.27}$$

We consider a rectangular central region of width W and length L coupled to 6 terminals (see Fig.4.7). The linear current density due to a current driven along the x direction is $j_x = I_x/W$ while $j_y = 0$. The electric field components are associated to the voltages as $E_x = V_L/L$ and $E_y = V_H/W$. Therefore, the resistivities $\rho_{xx} = \rho_L$ and $\rho_{xy} = \rho_H$ are:

$$\rho_L = \frac{V_L}{I}\frac{W}{L} = R_{xx}\frac{W}{L} \qquad \rho_H = \frac{V_H}{I} = R_{xy} \tag{4.28}$$

which shows that there is no system size dependence in the Hall resistance while the longitudinal resistance depends on an aspect ratio of the system W/L, as its classical analog. In this case, the system size should influence the height of the resistivity peaks ρ_{xx}. From the inverse relation of (4.28), we obtain the conductivity tensor components:

$$\sigma_{xy} = \frac{-\rho_{xy}}{\rho_{xx}^2 + \rho_{xy}^2} \qquad \sigma_{xx} = \frac{\rho_{xx}}{\rho_{xx}^2 + \rho_{xy}^2} \tag{4.29}$$

In the Hall regime, $\sigma_{xx} \to 0$ while $\sigma_{xy} \to 1/\rho_{xy}$. Both representations should be able to display the main features of the quantum Hall effect and can be used in a complementary manner. Due to the equivalence of dimensionality, resistance and resistivity, conductance and conductivity can be found being used interchangeably in the literature.

Following the procedure described in this section on a tight-binding lattice with a perpendicular magnetic field, one can numerically obtain the conductivity tensor, a geometry-independent variable, starting from the calculation of the scattering matrix coefficients.

4.2.2 The nonuniform gauge trick for multiterminal setups

To properly account for the magnetic field effect on the semi-infinite terminals of a Hall bar geometry (Fig.4.7) in the tight-binding approximation, one needs to consider a translational invariant gauge that is x-independent in terminals 1 and 4 and y-independent in terminals $2,3,5,6$. To this end, we resort to a smoothly changing vector potential that acquires translational symmetries at the terminals region, as proposed in Refs.[114, 60]. It is worth noting that alternative schemes have been proposed to handle the same problem [10, 115]. While Ref. [10] distorts the horizontal terminals to the vertical direction, building all the semi-infinite terminals along the y direction, Ref.[115] proposes a rotation to the vector potential in the region of the leads. The method that we discuss here was firstly proposed in Ref. [114] and can be computationally cheaper than [10], in the sense that it requires less extra sites to be implemented, and does not causes discontinuities to the magnetic field, as in [115]. In both cases, the gauge scheme could cause spurious scattering processes that could highly affect the extended localization of the transition states of the quantum Hall regime and, therefore, it could deform the resistivity tensor profile in the transition region between plateaus, a highly sensible curve (see discussion in the next section). Here, we demonstrate that, as long as gauge invariance is preserved, spurious scattering events are successfully avoided.

Starting from the general gauge (3.36) discussed in the previous chapter, one can choose an x-independent and a y-independent gauge as, respectively:

$$\mathbf{A}_x = -By\hat{\mathbf{x}} \qquad \mathbf{A}_y = Bx\hat{\mathbf{y}}. \tag{4.30}$$

A smooth transition between the both terms has to obey the gauge transformation condition:

$$\mathbf{A} = \mathbf{A}_x + \nabla f(x,y) \tag{4.31}$$

which is insensitive to the magnetic field $\mathbf{B} = \nabla \times \mathbf{A}$. As proposed in Ref. [114], it is convenient that:

$$f(x,y) = W(x)v(x,y), \qquad v(x,y) = Bxy \tag{4.32}$$

The function $W(x)$ is a smooth step function that is 0 in leads 1 and 4 and 1 in the region comprising the leads $2,3,5,6$. We choose the function:

$$W(x) = \frac{1}{2}\left[\tanh\left(\frac{x-x_1}{d_x}\right) - \tanh\left(\frac{x-x_4}{d_x}\right)\right] \tag{4.33}$$

where x_i is the geometric center of terminal i along the x axis and d_x is the smoothness of the step. The explicit form of the vector potential can be written as:

$$\mathbf{A} = B\frac{d}{dx}\left[(W(x)-1)x\right]y\hat{\mathbf{x}} + BW(x)x\hat{\mathbf{y}} \tag{4.34}$$

which can be integrated in Eq. (3.37) with the appropriate techniques. Fig. 4.8 displays the real part of $t_{k,k} = t_0 e^{i\phi_{k,k'}}$ as a color map for a strong magnetic field (a short range scalar disorder is also included, which gives the noisy aspect of the figure). One can see that the periodicity of the phase is vertical in the central region and smoothly changes to an horizontal periodicity in the lateral terminals.

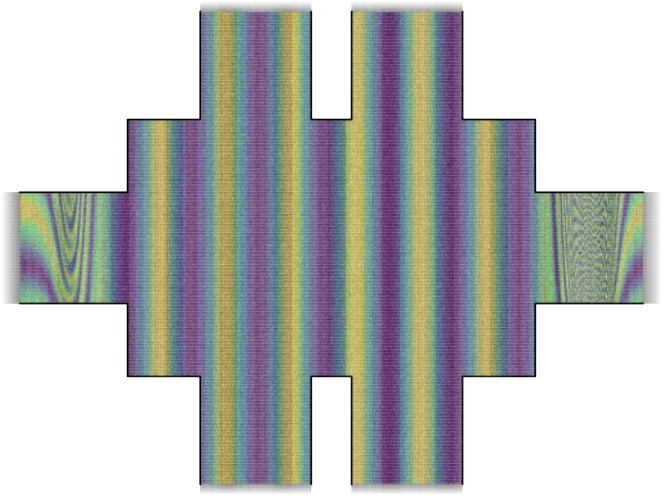

Fig. 4.8 Color map of Re $\left[t_{k,k'}\right]/t_0$ in a disordered graphene Hall bar coupled do six semi-infinite leads (shaded regions). The intensity of the color map goes from -1 (darker color) to 1 (lighter color).

The only region of concern is where the vector potential changes from one gauge to the other, that is when $W'(x) \neq 0$ (the nonuniform region in Fig.4.8). As long as d_x is chosen such that the vector potential varies smoothly when compared to the lattice spacing, namely, $d_x \gg a$, descontinuities are avoided.

Note that the same result could not be achieved through the gauge scheme $\mathbf{A} = B(\beta - 1)y\hat{\mathbf{x}} + B\beta x\hat{\mathbf{y}}$ for $0 < \beta < 1$, known in the literature. Even if β changes smoothly, such scheme would keep the magnetic field as constant, but the gauge invariance when $\beta \to \beta(x)$ would be violated.

In Ref. [114], a more general approach is discussed for multiterminal setups whose terminals are oriented to arbitrary directions.

4.3 Results and discussions

We consider a disordered graphene sheet in a Hall bar geometry under a strong magnetic field, as depicted in Fig. 4.7. The graphene sheet is described by the tight-binding model, as shown in chapter 3. The disorder models are also accounted for as specified in the previous chapter, using a sum of randomly distributed Gaussians in case of long-range disorder and uncorrelated random onsite energies in case of short-range disorder. The horizontally coupled leads, 1 and 4, have armchair edges and, to keep the continuity along the lattice, the vertical leads, $2,3,5,6$ have zigzag edges. The magnetic field is included using the scheme described in the previous section and is also considered in the leads semi-infinite portion.

We calculate the system longitudinal and transverse resistances using the Landauer-Büttiker formula, Eq. (2.9), considering the terminals $\alpha = 2,3,5,6$ as voltage probes, that is, $I_2 = I_3 = I_5 = I_6 = 0$ (see inset of Fig. 4.9b). In this setting, $I_1 = -I_4 = I$. Hence, we aim to numerically obtain the resistances $R_{xx} = R_{23,14} = R_{56,14}$ and $R_{xy} = R_{26,14} = R_{35,14}$, as discussed in the previous section. Due to the possibility to measure the longitudinal and transverse resistance in two uncoupled ways, an average of the equivalent resistances can be used to smooth the fluctuation effects caused by disorder.

We start our discussion by presenting our general findings based on single disorder realization simulations of a graphene Hall bar containing $\sim 10^6$ sites and the longest distance in the system (from the left to the right arm) is $\sim 0.246\mu m$. The onsite short-range disorder is randomly chosen in the interval $[-\delta W, \delta W]$ where $\delta W = 0.8t$. Fig.4.9 displays the obtained resistances as a function of the Fermi energy E_F (upper Figure) and the magnetic flux ϕ in units of the magnetic flux quantum $\phi_0 = h/e$. The results for R_{xy} and R_{xx} correspond to typical quantum Hall resistance curves for graphene samples [108]. The quantized Hall plateaus are located at $R_{xy} = \frac{h}{2e^2}\frac{1}{2n+1}$ for integer values of n while a zero longitudinal resistance R_{xx} is observed at the R_{xy} plateau region. In the plateau-plateau transition intervals, the longitudinal resistance displays nonzero fluctuations due to the single-disorder realization that fluctuates with the changing of the respective field. Experimentally, such fluctuations are averaged out by temperature effects and the self-averaging of the electronic current in large samples.

It has been argued in the literature that the experimental results of Hall quantization are robust and can be probed even in relatively dirty (strongly disordered) samples and at high temperatures. This feature is also present in numerical simulations where subtle discontinuities in the magnetic field or in the system edge are difficult to be detected by resistances due to the robustness of the quantum Hall effect. Despite the fact that the Hall plateaus are, to some extend, insentitive to small disorder scatterings, the transition regions are highly sensitive, and could distort the quantum phase transition properties that we are interested.

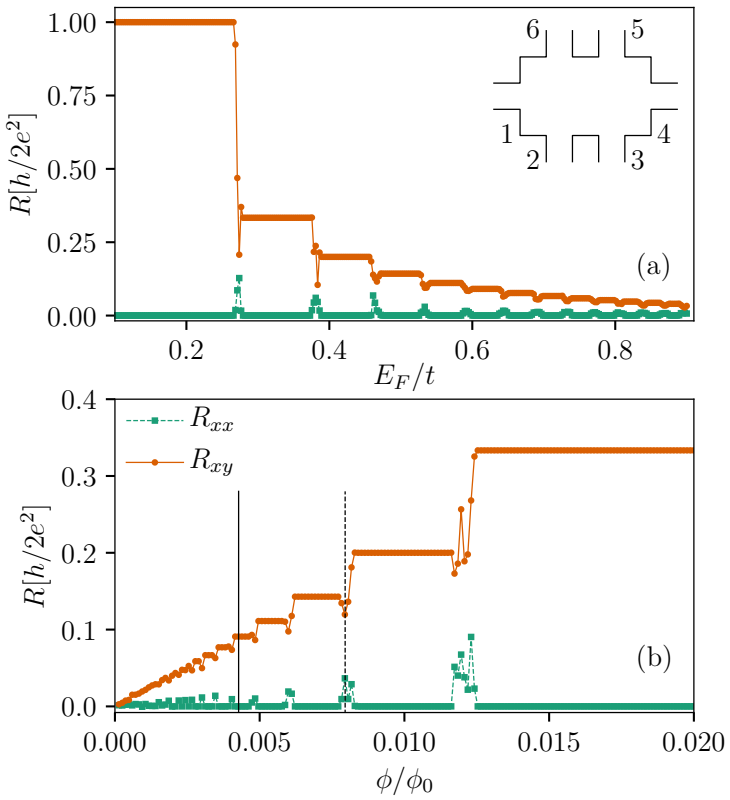

Fig. 4.9 Graphene Hall bar longitudinal R_{xx} and transverse R_{xy} resistance for a single disorder realization (10^6 atoms and $T = 0$) as a function of (a) E_F/t for $\phi/\phi_0 = 0.007$ and (b) ϕ/ϕ_0 for $E_F/t = 0.5$.

We calculate the local density of states (LDOS) and local current as auxiliary tools to detect localizations due to the possible sources of scattering processes. Figures 4.10.a and 4.10.b display LDOS of the single short-range disorder realization for edge states along the sample in the plateau region and an extended state in the transition region between two plateaus (solid and dashed vertical lines of Fig. 4.9), respectively. The local current corresponding to the edge states of Fig. 4.10a is displayed in Fig. 4.10c, where the vector field associated to the current direction of propagation is shown as stream lines on top of nonzero current intensities.

From the LDOS at the edge states, it can be verified that the magnetic length is a good estimative to the localization length at the edge states (vertical red trace in Figure 4.10b).

It should be emphasized the advantages of the WFM method discussed in chapter 2 to compute such set of QHE properties. The linear dependence of the cpu time the system dimensions W, W' and L makes the WFM method convenient to large central areas, where

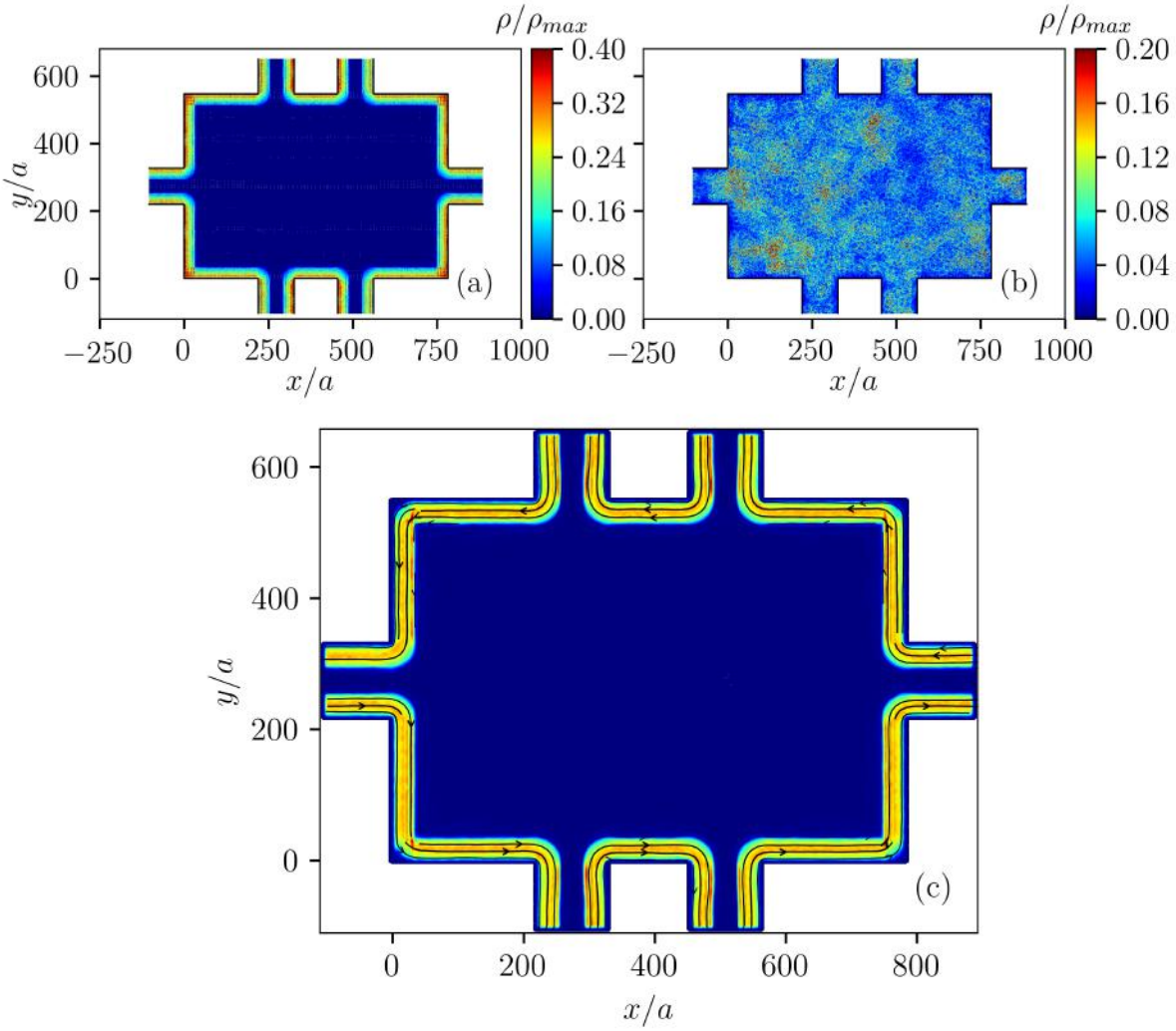

Fig. 4.10 Local density of states at $E_F = 0.5t$ and a magnetic flux of (a) $\phi = 0.004\phi_0$ (plateau state) and (b) $\phi = 0.008\phi_0$ (transition state). (c) Local current at $E_F = 0.5t$ and $\phi = 0.004\phi_0$ (plateau state).

more complex scatterers with long range correlations can be addressed. For the results here, the cpu time to calculate a single energy resistance point was about 60 seconds using one core of an Intel®Xeon®X5650 processor, much smaller than what one could achieved with other quantum transport methods, such as the RGF. Another important feature of the WFM is the direction of propagation of the current, which can be naturally captured from the velocities of the leads eigenmodes basis. As a consequence, negative resistances are directly obtained when negative Fermi energy values, corresponding to a negative current, are applied. Moreover, the QHE observed in graphene could be easily extended to other materials whose

a localized basis description requires more orbitals per site. Such basis complexity could be included with almost no cost by using the Kwant sparse solvers.

4.3.1 The case $T = 0$: Disorder-driven phase transitions

Let us now discuss the transport properties in a graphene Hall bar under strong magnetic field $\phi = 0.007\phi_0$ for disorder-averaged results. To obtain a suffiently smooth conductance, we consider samples of $\sim 10^5$ sites and calculate the average of the transmission matrix for 100 disorder realizations.

We consider the four types of disorder, short-range onsite, short-range chiral, long-range onsite, long-range chiral, as discussed in the previous chapter. For practical reasons, we summarize in this section the definition of the scalar and chiral disorder models as follows:

- **Short-range scalar disorder**: randomly chosen onsite energies ε_i from an uniform distribution $\varepsilon_i \in [-\delta W, \delta W]$;
- **Short-range chiral disorder**: randomly chosen carbon atoms heights z_i from an uniform distribution $z_i \in [-z_{max}, z_{max}]$, respectively;
- **Long-range scalar disorder**: sum of randomly distributed Gaussians over the onsite energies:

$$\varepsilon(\mathbf{r}_i) = \sum_{n=0}^{M_{max}} u_n e^{-|\mathbf{r}_i - \mathbf{R}_n|^2/2\xi^2}; \tag{4.35}$$

- **Long-range chiral disorder**: sum of randomly distributed Gaussians over the (carbon lattice site atoms) heights:

$$z(\mathbf{r}_i) = \sum_{n=0}^{N_{max}} z_n e^{-|\mathbf{r}_i - \mathbf{R}_n|^2/2\zeta^2}. \tag{4.36}$$

In Fig. 4.11, the conductivities for the short-range disorder-averages are displayed. The standard error of the mean is displayed as error bars. In both cases, onsite and chiral short-range disorder, fluctuations are concentrated only in the transition regions between plateaus and, despite the smoothness of the averaged curve σ_{xx} for the peaks of $n \neq 0$, fluctuations are strong around the LL $n = 0$ and even seem to not converge.

Despite the quantum Hall effect of graphene containing short-range disorder having been numerically obtained[11, 10], comparisons with the literature for the different disorder types has never been discussed. It has been argued [95, 111] that the anomalous nature of the quantum Hall effect in graphene requires the K and K' valley to be uncoupled, which is not the

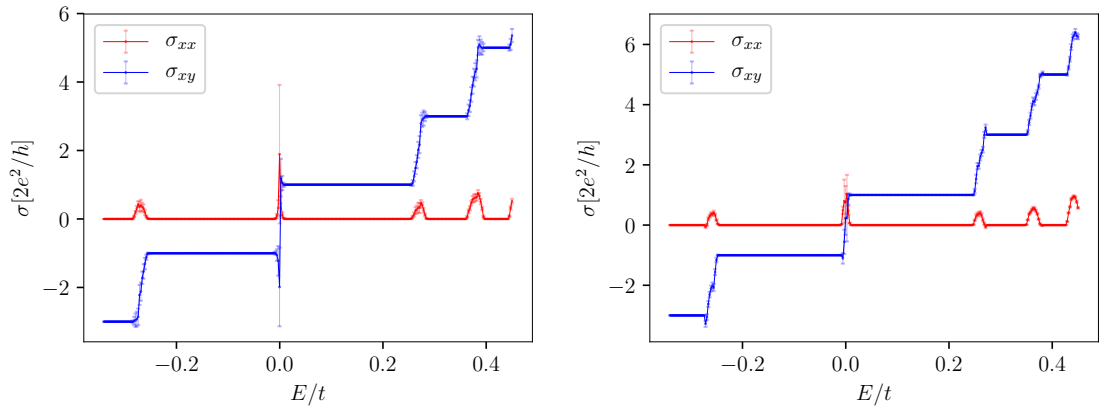

Fig. 4.11 Transverse σ_{xy} and longitudinal σ_{xx} conductivity around the Dirac point for short-range disorder. Result is the average of 100 realizations and magnetic flux $\phi = 0.007\phi_0$. (a) Onsite disorder for $\delta W = 0.2t$. (b) Hopping disorder for $z_{max} = 0.2a$.

case for short-range disorder, as discussed in the previous section. IThe latter was predicted [95] to cause the lifting of the degenerated valleys, which could be evidenced by extra plateaus in the even multiples of $2e^2/h$. However, such splitting due to short-range onsite disorder has never been observed and Fig.4.11a is also an evidence that, despite the valley coupling to be taking place, the symmetry is preserved. It should be mentioned that, in the previous chapter, simulations using similar disorder configurations on a graphene nanorribon were capable to detect the WL-WAL transitions as an evidence of a valley-coupling switch as a function of the disorder strength.

The transverse and longitudinal conductivities for the case of hopping disorder is shown in Fig. 4.11b. Similar quantized plateaus at the predicted values $\frac{2e^2}{h}(2n+1)$ are also demonstrated. However, there are two interesting features to be discussed. First, due to the lattice deformations used in the model, only extensions between neighboring carbon atoms are present, where a realistic model should account for squeezed deformations also. The main effect of such one-sided deformation is a shift to the magnetic field $B \to B + \delta B_{strain}$ where δB_{strain} is a pseudomagnetic field overall effect. It could shift the energy centers $E_n \sim \sqrt{Bn}$ an increase in the positions of the LL along the calculated Fermi energies.

Despite no clear degeneracy lifting has being observed, a subtle level splitting pattern seems to be taking place in all plateaus transitions. In case of the $n = 0$ level, the fluctuations are strong and such effect remains unclear. A similar result has been observed in Ref.[111], where the existence of degeneracy breaking between valleys due to a short-range hopping disorder has been demonstrated and a subtle splitting has been observed with numerical calculations using the Kubo formalism. A zoom in the energy range at the transition region

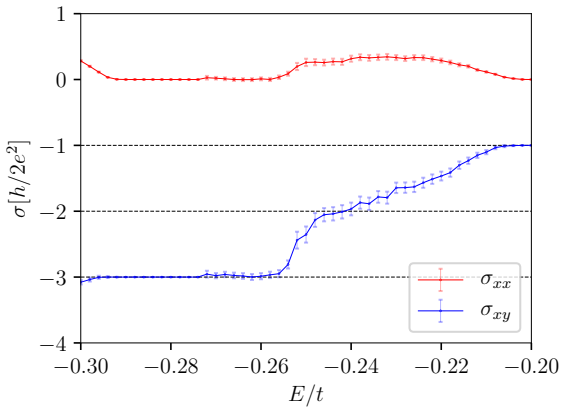

Fig. 4.12 Zoom at the plateau transition of level $n = -1$ where a subtle protuberance seems to be forming around $E_F = 0.25t$

($n = -1$) indicates a possible level splitting, see Fig.4.12. This is not a clear evidence because, in case of formation of an intermediate plateau, a change in the fluctuation should also be observed, which is not the case. Such result requires a focused investigation.

Regarding the long-range disorder cases, results are pictured in Fig.4.13. In both cases, the peaks width along the σ_{xx} curve are relatively smaller than their short-range counterparts. This is mainly due to the robustness of the Hall localization of edge states which tend to be formed right away the critical energy points. Note that the disorder strengths are relatively small as compared to the short-range disorder. This is due to the possibility of the formations nanobubbles which may confine LL inside a single Gaussian when the magnetic length is of the order of the Gaussian effective radius. When the system has such nanobubbles, fluctuations due to the spatial confinements were observed in the conductivity tensor at the plateau regions and also in the LDOS (not shown in this thesis).

The quantization values are the same as in the case of the short-range disorder. Due to the lack of coupling between the K and K' valleys, the observed degeneracy do agree with the general theory of the anomalous quantum Hall effect.

The case of long-range hopping disorder shows another interesting result. Differently from all the other cases, there is no peak at the σ_{xx} around the LL $n = 0$ evidencing that such level is insensitive to the present disorder. This is a case of complete localization of the underlying LL, $\sigma_{xx} = \sigma xy = 0$ at $E = 0$.

4.3.2 The case $T \neq 0$: Temperature diagrams and universal power laws

In this section, we discuss the temperature effects on the conductivity tensor in graphene in the quantum Hall regime. Since our calculations do not account for decoherence processes, i.e.

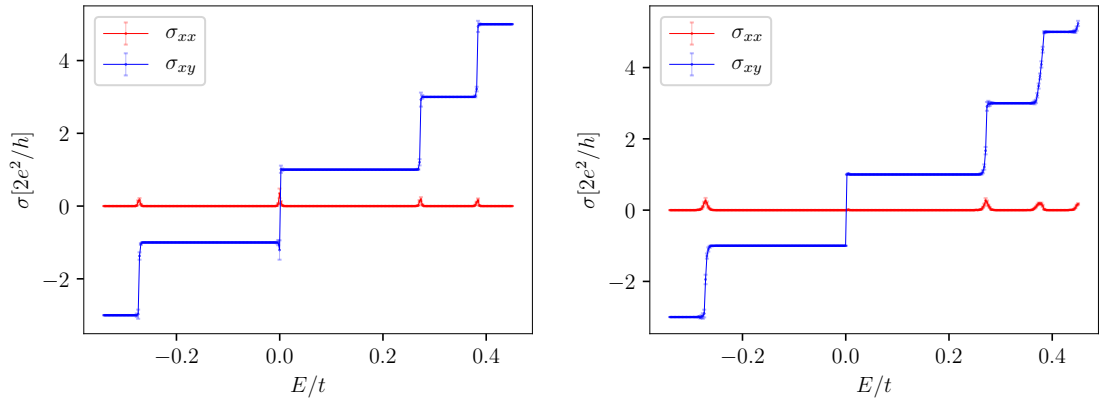

Fig. 4.13 Same as Fig.4.11 for long-range disorder realizations. (a) Onsite disorder: $u_{max} = 0.016t$, $\xi = 4a$. (b) Hopping disorder: $z_{max} = a$, $\zeta = 5a$.

$l_\phi \to \infty$, temperature smears the Fermi surface and effectively introduce an average over the Fermi energy E_F. Due to the numerical discreteness of the energy data, the temperature has a lower bound T_{min} given by the width of energy step δE which corresponds to $k_B T_{min} \gg \delta E$, where k_B is the Boltzmann constant. At the other limit, the maximum temperature has to be smaller than the width of the Hall plateaux being analysed $k_B T_{max} \ll \Delta E_{N,N\pm1}$.

We follow the same order of discussion of the $T = 0$ case. First, we present the general results for the short-range onsite disorder and we compare the different types of disorder. Fig. 4.14a presents the resistance as a function of the Fermi energy for different temperatures, ranging from $k_B T = 10^{-3}t$ to $k_B T = 10^{-2}t$, where $t \approx 2.7eV$ in graphene. One can see the increasing of the smoothness of the curves along with the destruction of the plateaus to a monotonic curve. The high temperature situation tends to the classical resistance behavior, which is linearly dependent on the inverse of charge density n_e as the temperature smears the Hall plateaux.

The $n = 0$ LL always displays special features regarding temperature effects. First of all, our simulations shows that it is robust against temperatures, as observed in Ref. [116]. Secondly, the temperature effect over the ρ_{xx} and ρ_{xy} components manifest individually different despite being coupled by the unitarity of the conductance matrix. While the longitudinal resistivity maximum point is increased by temperature close to the charge neutrality point, the maximum at the other levels are decreased (see Fig. 4.14b). The Hall resistivity also presents an very particular behavior at $n = 0$, it is almost independent on the temperature at the transition region from $-1h/2e^2$ to $1h/2e^2$. In the flow diagrams, Fig. 4.14b, we observe the flow of the resistivity components against temperature, the maximum

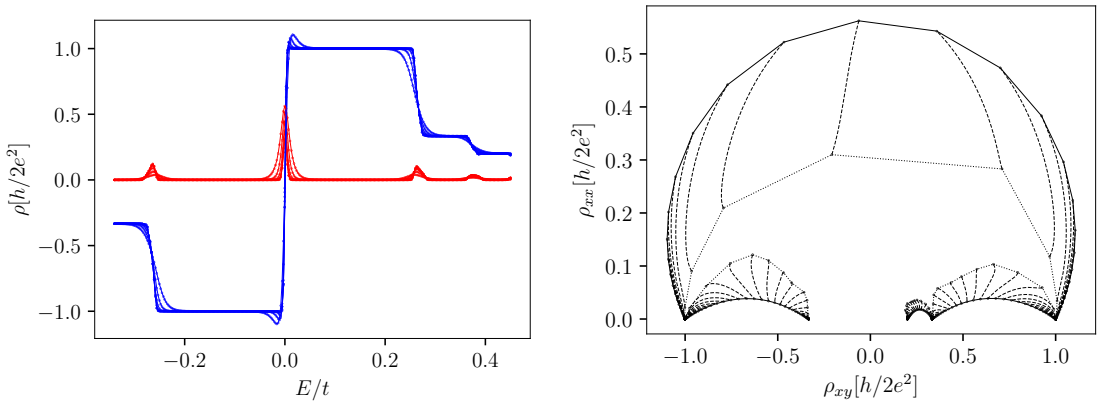

(a) (b)

Fig. 4.14 (a) Isothermal resistivity curves as a function of the Fermi energy for an onsite short-range disordered graphene with disorder amplitude $\delta W = 0.2t$. Result is shown for the average of 100 disorder realizations. Temperature range is from $K_BT = 0.001t$ to $K_Bt = 0.01t$, and magnetic flux of $\phi = 0.007\phi_0$. (b) The corresponding flow diagram (ρ_{xx}, ρ_{xy}). The solid line is the coolest curve and the dotted line is the hottest one. The dashed ines are the isonergetic curves $(\rho_{xx,E_F}(T), \rho_{xy,E_F}(T))$ as function of the temperature and are guide to the eye for the flow evolution.

temperature is denoted by solid line and the minimum one by the doted line, dashed lines are isoenergetic curves.

A scaling dependence of temperature of the peaks width in both E_F and B parameters is displayed in Fig.4.15. As previously argued, there is a scaling parameter that has been observed for other materials at the quantum Hall regime, given by the width of the σ_{xx} peaks as function of the magnetic field at half maximum $\Delta B \sim T^{\kappa}$ and the unversal value of $\kappa = 0.42$ has been verified[105]. We note a discrepancy with the exponent that we find in our simulations $\kappa = 0.33$ as considerably smaller than the universal one. It has been discussed in the literature that in presence of a spin-orbit coupling, the scaling parameter should be diminished[102].

The phase diagram and the isothermal resistivity curves for the short-range hopping disorder are displayed in Fig. 4.16.a. As opposed to the short-range onsite case, the resistivity peak ρ_{xx} in the $n = 0$ level tends to decrease with temperature, similarly to the $n \neq 0$ cases. Also, we note that the respective flow diagram seems to be not well behaved. We also note that there is an increase in the Hall resistivity around $n = 0$ to values greater than $|h/2e^2|$ and causes the horizontal distortions to the diagrams. In the case of the hopping disorder, such distortion is veri strong.

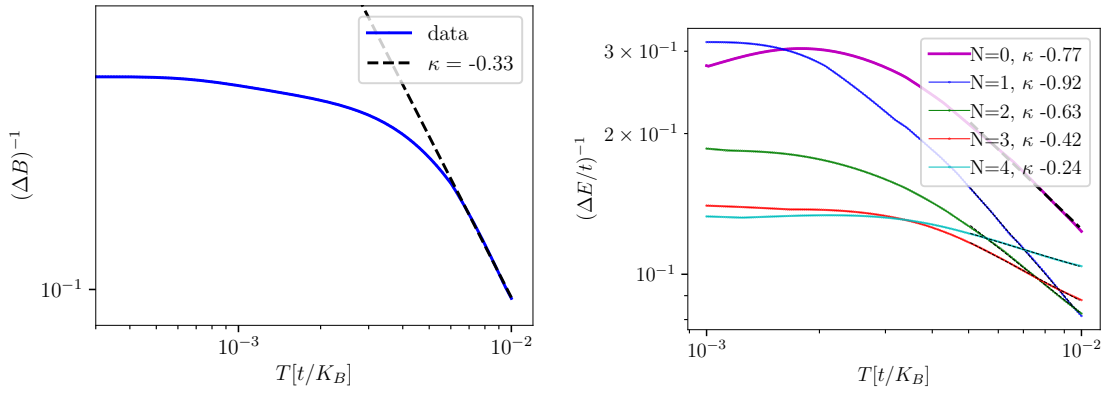

(a) (b)

Fig. 4.15 (a) Scaling parameters of transition state by varying B. (b) Scaling parameters of several transition states by varying E_F.

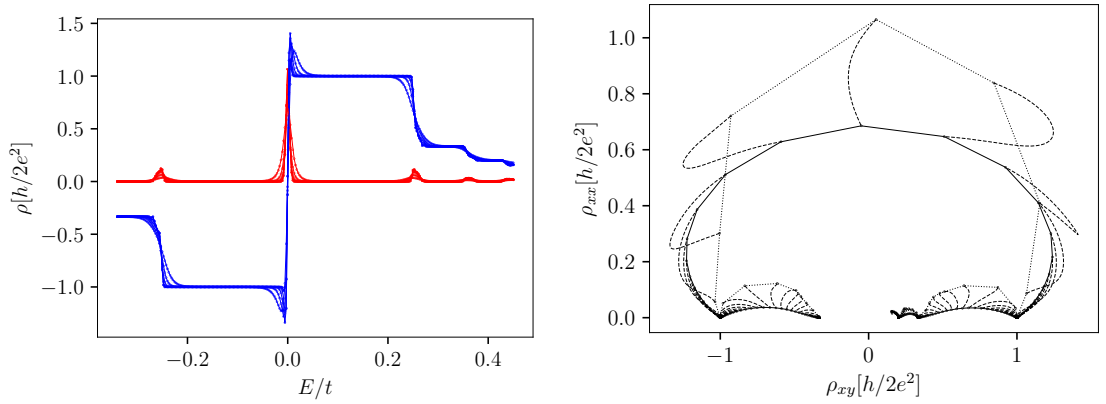

(a) (b)

Fig. 4.16 Same as Fig. 4.14 but for te short-range hopping disorder.

Moreover, despite the difference in the peaks heights, there is no significant difference when $n \neq 0$ between the two short-range disorder cases.

The long-range onsite disorder is very similar to the short-range onsite disorder and is not displayed. In the long-range hopping disorder case, the state $n = 0$ did not shown a peak around $n = 0$ and the respective diagram is not displayed here.

4.4 Conclusions

In this chapter we presented a numerical study of the longitudinal and Hall resistivities of in a disordered graphene Hall bar in the strong magnetic field/quantum Hall regime. We analysed two kinds of disorder, scalar and chiral, in the short-range and in the long-range limit. To this end, we revised the theory of the anomalous Hall effect in the clean and in the disordered case [108, 79, 111, 95]. We also discussed how to calculate the resistivity and conductivity tensor starting from the scattering matrix in the case of a Hall bar geometry.

We observed the conductivity tensor as a function of the Fermi energy and compared the result for different disorder regimes. We observed that the long-range disorder effect are much smaller than the long-range ones as a demonstration of the robustness of the quantum Hall effect in the absence of backscattering (long-range case). We also observed the absence of a peak in the charge neutrality point when only long-range hopping disorder is present.

In the nonzero temperature case, we discussed the $\rho_{xx} \times \rho_{xy}$ diagrams for each disorder kind and compared the temperature dependence of the resistivity arcs. We showed that while both the short-range and the long-range onsite disorder the longitudinal resistivity peak at $n = 0$ increase with temperature, the short-range hopping disorder decreases. For the long-range hopping disorder case, we observed divergence with temperature in the $n = 0$ LL. For the $n \neq 0$ case, the result is similar for all observed disorder types, displaying peaks height decreasing with temperature.

The absence of level splittings and the consequent of extra plateaus in even integers of the conductance quantum was not observed, even in the case of valley coupling, contradicting the predictions of the literature [95]. In the case of short-hopping disorder, we find a subtle protuberance indicating a possible plateau, which corroborates Ref.[111]. However, a deeper investigation is required, as the plateau shape is not clear.

Part II

Time-dependent quantum transport

Chapter 5

Numerical methods of time-dependent quantum transport

Experiments and theory on real-time quantum electron dynamics reveal fascinating new properties that go unnoticed in the stationary physics. Several recent experiments considering driven systems, such as quantum pump [117], dynamical generation of spin currents [118] and single-shot electron injection [119], call for numerical methods to address time-dependent quantum electron transport. When the electronic time of flight τ_F is shorter than the phase relaxation time τ_ϕ, dynamical interference effects can emerge [44]. When the characteristic times of the experiment are shorter than the Ehrenfest time, particle-like effects dominate the dynamics and, under appropriate apparatus, can be observed.

Nowadays, the realization of such dynamics are made possible within great precision. As a result, the confinement and manipulation of single electron sources has being explored for solid state devices applications such as nanowires and quantum dots[119]. The possibility to fully control individual electrons coherently enables the realization of several optical analogs experiments such as interferometers[45], beam-splitters[120], collimating lenses[121], and so on. When compared to photons, the advantage of performing "quantum optics" on electronic pulses is the presence of the Coulomb coupling, which allows for exploring the manipulation of information a step further, by coding inside the coupling of quantum states, the current elementary building blocks of quantum information of two-qubits operations.

In this chapter, we introduce the time-dependent methods of the scattering problem under the tight-binding approximation. Differently from the chapter 2, where our main motivation has been to discuss the stationary methods due to the lack of a devoted literature, the time-dependent methods used by T-Kwant package are documented along several references [41, 38–40], including implementations tips and benchmarks. However, due to the complete discussion of the stationary methods present in chapter 2, in this thesis we are able to present

a time-dependent extension of the wave-function matching and compare the results with the T-Kwant methods. We also present the main formalism behind the time-dependent scattering problem.

In section 5.1, we discuss the wave-function matching in the time-domain and with a time-dependent perturbation, from where we obtain the nonequilibrium Green's function equations, similarly to chapter 2. In section 5.2, we review the T-Kwant methods and demonstrate that the time-dependent Schrödinger equation can be written as a differential equation with a source term. We also discuss the inclusion of electron-electron interactions in the time-dependent Hartree-Fock approximation. This chapter constitutes a basis for the discussions of the following chapter, where we provide an application developed with T-Kwant.

5.1 Theoretical background

Here, we present a discussion to the stationary wave function matching equations after the inclusion of a time-perturbation. Moreover, we demonstrate a set of useful equations for the discussions presented in the following chapter.

Let us define a time-independent mesoscopic region coupled to semi-infinte multiple terminals, which are described in chapter 2. Here, the stationary Hamiltonian is denoted by H_0. We consider a time-dependent perturbation using the Heisenberg picture:

$$H(t) = H_0 + W(t), \qquad W(t \leq 0) = 0 \tag{5.1}$$

Introducing the projection operators, Q and P represent the central and the asymptotic region, respectively (see Fig.2.1), we can consider an arbitrary time perturbation as the diagonal operator:

$$W(t) = W_{QQ}(t) + W_{PP}(t) \tag{5.2}$$

To preserve translational symmetry in the leads, we consider $W_{PP}(t)$ as an homogeneous time-perturbation. By applying a proper unitary rotation $U(t) = \mathbb{I}_{QQ} + U_P(t)$, where $U_P(t) = e^{-\frac{i}{\hbar}\int_{-\infty}^{t} dt' W_{PP}(t')}$, we obtain:

$$H(t) = H_{QQ}(t) + H_{PP} + H'_{QP}(t) + H'^{\dagger}_{QP}(t), \tag{5.3}$$

where $H_{QQ}(t) = H_{QQ} + W_{QQ}(t)$, $H'_{QP}(t) = H_{QP}U_P(t)$ and $H'^{\dagger}_{QP}(t) = U_P^{\dagger}(t)H_{PQ}$ are the interface Hamiltonians that carry a time-dependence getting rid of any perturbation in the asymptotic region.

One should note that the time-dependent Schrödinger equation:

$$H(t)\,|\psi(t)\rangle = i\hbar\frac{\partial}{\partial t}\,|\psi(t)\rangle \tag{5.4}$$

gives us the time-evolution operator, written in the interaction picture, as:

$$\langle f|\,U_I(t,t_0)\,|i\rangle = \delta_{i,j} - \frac{i}{\hbar}\sum_m \int_{t_0}^{t} dt' e^{-i(E_f-E_m)t'/\hbar} W_{fm}(t')\,\langle m|\,U_I(t',t_0)\,|i\rangle \tag{5.5}$$

where $|\psi(t)\rangle = U_I(t,t_0)\,|\psi(t_0)\rangle$. The left hand side of Eq. (5.5) gives us the scattering matrix element in time space for the scattering between the asymptotic states $i \to f$, namely [122]:

$$S_{fi} \equiv \lim_{t\to\infty} \langle f|\,U(t,-\infty)\,|i\rangle \tag{5.6}$$

The right hand side of Eq. (5.5) also gives us an interesting information. The term $W_{fm}(t')$ allows for energy transitions. Due to possible energy gains and lost during transitions over the states and to the openness of the system system, the inelastic scattering matrix in energy space representation becomes $S_{mm'}(E,E')$ with a two-fold continuous dependence in energy, namely, E and E'.

5.1.1 The wave function matching in time-domain

In this section, we describe how the scattering matrix formalism, derived in chapter 2, is generalized to the time-domain. For this purpose, we include the time perturbation to the Hamiltonian and present the corresponding wave function matching equations in the tight-binding approximation. At the end, one is presented to a complete analysis of the consequences of a time-perturbation to the scattering theory from the wave function matching perspective. An interesting result of such analysis is the demonstration of the nonequilibrium Green's funcions (NEGF) in the time-domain under a simple scheme, similarly to what is done for the NEGF formalism demonstrated for the stationary case in Chapter 2. We also show that the wave function at the scattering region has a similar dynamics to the Retarded Green's function equation of motion, being an alternative to a NEGF approach for time-dependent problems.

We start by describing a mesoscopic cavity S coupled to an effective lead T that contains an arbitrary number of terminals (see Fig. 2.2).

The time-dependent Schrödinger equation in the tight-binding representation of the system reads:

$$\begin{pmatrix} H_S(t) & V_{TS}^{\dagger}(t) & & \\ V_{TS}(t) & H_T & V_T^{\dagger} & \\ & V_T & H_T & \ddots \\ & & \ddots & \ddots \end{pmatrix} \begin{pmatrix} \psi_S(t) \\ \psi_0(t) \\ \psi_1(t) \\ \vdots \end{pmatrix} = i\hbar \frac{\partial}{\partial t} \begin{pmatrix} \psi_S(t) \\ \psi_0(t) \\ \psi_1(t) \\ \vdots \end{pmatrix}, \tag{5.7}$$

where $H_S(t)$, $H_{ST}(t)$ and $H_T(t)$ carry the time-perturbation present in the system, lead-system interface and leads region, respectively. Let us now find a solution to the set of equations (5.7). Far from the scattering region, we assume an asymtotic solution as $\lim_{n\to\infty} \psi_n \to \phi_n$. Therefore, we obtain the lead dynamical equation:

$$V_T \phi_{n-1}(t) + (H_T - i\hbar\partial_t)\phi_n(t) + V_T^{\dagger}\phi_{n+1}(t) = 0 \tag{5.8}$$

Because H_L is time-independent and the eigenproblem is translational invariant, the solution can b expressed by a stationary Block funcion:

$$\phi_{nE}(t) = \chi_E \lambda_E^n e^{-iEt/\hbar} \tag{5.9}$$

where χ_E is the lead unit-cell eigenfunction which is now dependent of the energy E as a variable parameter. The functions $\phi_{nE}(t)$ of Eq. (5.9 are substituted into Eq. 5.8 and the problem is then rearranged as a Generalized Eigenproblem (GEP) whose solution is described in chapter 2. One resorts on a set eigenvectors $\chi_{qE}^{\pm}$ and eigenvalues $\lambda_{qE}^{\pm}$ which are classified as outgoing $(+)$ and incoming modes $(-)$ according to the sign of $\arg(\lambda_E^{\pm})$ and following the propagation criteria $|\lambda_E^{\pm}| = 1$ [1]. Evanescent modes $|\lambda_E| \neq 1$ are not considered here, however such generalization is achievable.

As a boundary condition, we consider a single incoming mode q at energy E, which is related to the q-th column of the scattering matrix S_{pq} of a scattering process to the outgoing mode p. However, differently from the stationary problem, inelastic scattering processes are now allowed and require a more general form of scattering matrix $S_{pq}(E',E)$, accounting for the possible transitions to an outgoing mode p at energy E', as previously discussed. The wave-function $\psi_{nqE}(t)$ of the n-th unit-cell due to an incoming mode q of energy E at time t

[1] The association between the eigenvalues $\lambda_{qE}^{\pm}$ and the crystal momentum $k(E)$ allow us to write the lead eigenmodes as the usual form of propagating waves:

$$\phi_{nE}^{\pm}(t) = \chi_E^{\pm} e^{i[\pm k(E)na - Et/\hbar]} \tag{5.10}$$

reads:

$$\psi_{nqE}(t) = \chi^{-}_{qE}(\lambda^{-}_{qE})^n e^{-iEt/\hbar} + \sum_{p=1}^{N_p} \int \frac{dE'}{2\pi} \chi^{+}_{pE'}(\lambda^{+}_{pE'})^n S_{pq}(E',E) e^{-iE't/\hbar}. \tag{5.11}$$

Let us derive the equation of motion for the scattering function $\psi_{SqE}(t)$. We write the wave function of the $n-th$ slice in a general form, namely:

$$\psi_{nqE}(t) = \psi^{-}_{nqE}(t) + \psi^{+}_{nqE}(t). \tag{5.12}$$

We also define the wave function in the energy domain as the Fourier-transformation:

$$\psi^{\pm}_{nqE}(E') = \int dt e^{iE't} \psi^{\pm}_{nqE}(t), \tag{5.13}$$

where the subscript E denotes the energy of the incoming mode and E' denotes the energy parameter in the energy domain. Moreover, it is convenient to define the translation operator $F^{\pm}(E')$ in the energy domain as:

$$\psi^{\pm}_{n+1qE}(t) = \int \frac{dE'}{2\pi} F^{\pm}(E') \psi^{\pm}_{nqE}(E') e^{-iE't}, \tag{5.14}$$

where

$$F^{\pm}(E') = \sum_{p} \lambda^{\pm}_{pE'} \chi^{\pm}_{pE'} \left(\tilde{\chi}^{\pm}_{pE'}\right)^{\dagger}. \tag{5.15}$$

Due to the convolution theorem, Eq. (5.14) represents a convolution in the time-domain:

$$\psi^{\pm}_{n+1qE}(t) = \int dt' F^{\pm}(t-t') \psi^{\pm}_{nqE}(t'). \tag{5.16}$$

This set of definitions, Eq. 5.12 to Eq.5.16, are used below.

Close to the scattering region, we write the first two lines of the Schödinger equation as:

$$(H_S(t) - i\hbar\partial_t)\psi_{SqE}(t) + V^{\dagger}_{TS}(t)\psi_{0qE}(t) = 0, \tag{5.17}$$

$$V_{TS}(t)\psi_{Sq}(t) + (H_T - i\hbar\partial_t)\psi_{0qE}(t) + V^{\dagger}_{T}(t)\psi_{1qE}(t) = 0, \tag{5.18}$$

By applying sucessive Fourier-transformations to equation (5.18) and rearranging the terms freely in the energy domain, in analogy to the stationary case, we obtain:

$$V_{TS}(t)\psi_{Sq}(t) + \int \frac{dE'}{2\pi} \left[(H_T - E' + V^{\dagger}_{T} F_{+}(E'))\psi_{0qE}(E') + \Gamma(E')\psi^{-}_{0qE}(E')\right] e^{-iEt\hbar} = 0, \tag{5.19}$$

where we have used the equation:

$$\psi_{1qE}(E') = F_-(E')\psi^-_{0qE}(E') + F_+(E')\psi^+_{0qE}(E') \tag{5.20}$$

and defined the function $\Gamma(E') = V_T^\dagger(F_-(E') - F_+(E'))$. By comparing Eq. (5.19) with the stationary solution, we identify the surface retarded Green's function:

$$G_T(E) = (E' - H_T - V_T^\dagger F_+(E'))^{-1} \tag{5.21}$$

where we identify the free retarded Green's function $G_T(E')V_T = F_+(E')$ from the recursive property of the retarded Green's functions [38, 48]. As $G(E)$ describes a steady state, it is possible to write Green's functions in time-domain as $G(t-t')$, since there is a translational invariance of steady states in time. Thus, the retarted and advanced Green's functions transform as:

$$G_T^{R(A)}(t-t') = \int \frac{dE}{\pi} e^{-iE(t-t')} G_T^{R(A)}(E). \tag{5.22}$$

The complete Fourier-transform of Eq. (5.19) leads us to the following equation in energy domain:

$$\psi_{0qE}(E') = \int \frac{d\varepsilon}{2\pi} G_T(E')V_{SL}^\dagger(E'-\varepsilon)\psi_{SqE}(\varepsilon) - G_T(E')\Gamma(E')\psi^-_{0qE}(E'). \tag{5.23}$$

Substituting Eq. (5.23) into (5.17) and transforming back to the time domain, we finally obtain:

$$(H_S(t) - i\hbar\partial_t)\psi_{SqE}(t) + \int dt'\Sigma(t-t')\psi_{SqE}(t') + \int dt'dt''V_{ST}(t)G_T(t-t')\Gamma(t'-t'')\psi^-_{0qE}(t'') = 0 \tag{5.24}$$

where $\Sigma(t-t') = V_{ST}(t)G_T(t-t')V_{ST}^\dagger(t')$ is the embedding self-energy in the time-domain. The last term is the source $Q^-_{qE}(t)$, which gains a time-dependence from the coupling $V_{ST}(t)$. If $V_{ST}(t)$ and $H_S(t)$ have their time perturbation removed, we recover the set of NEGF equations given in Chapter 2.

Eq. (5.24) has a similarity to the retarted Green's function equation of motion, namely:

$$\left[i\hbar\frac{\partial}{\partial t} - H_S(t)\right] G(t,t') = \delta(t-t') + \int du\Sigma(t,u)G(u,t') \tag{5.25}$$

where the δ component can be interpreted as a source term emitted at $t' < t$ [8]. A more detailed discussion about the scattering wave-function equation of motion is presented in Ref. [38] (see also Ref. [123] for a review).

From the orthogonality of the lead eigenmodes, we can calculate the scattering matrix as:

$$S_{pq}(E',E) = \int dt' \left[\tilde{\chi}^{+}_{pE'}\right]^{\dagger} \psi^{+}_{0qE}(t') e^{iE't'/\hbar}. \tag{5.26}$$

Substituting this result into (5.24), we can obtain the Fisher-Lee relation generalized to the time-domain[38].

In the next section, we write the time-dependent Schrödinger equation of the scattering wave function in the real-space basis in the way it is present in T-Kwant and that are used to obtain the local operators that are the main tools used to examine the scattering time-dependent problems in this thesis.

5.2 The time-dependent scattering methods

In th previous section, we discussed the NEGF equations and the scattering formalism in the time domain. However, the numerical implementation of both methods, the NEGF and the scattering wave-function matching method, would demand a prohibitively expensive computational cost for sufficiently large systems. The T-Kwant package[2], build over the Kwant suit, has proposed an alternative scheme that has the advantage of being (i) faster than previous schemes[39, 40] and (ii) utilizing the Kwant state-of-the-art methods in the backend calculations. In the following sections, we briefly review such scheme and discuss the operators that are used in the application present in the following chapter.

5.2.1 The Schrödinger equation with a source

In this section, we write the dynamical Schrödinger equation in a convenient way that allows us to describe time-dependent perturbations on open systems in a simplified form. At the end, one obtains the Schrödinger equation with a source and a sink term[39].

We consider the wave function *Ansatz* of a linear time-dependent correction term to the stationary wave function solution:

$$\psi_{qE}(t) = e^{-iEt/\hbar}\left[\psi^{st}_{qE} + \bar{\psi}_{qE}(t)\right], \qquad \bar{\psi}_{qE}(t \leq 0) = 0. \tag{5.27}$$

The function ψ^{st}_{qE} is the stationary scattering wave function due to an incoming mode q at energy E. It is given by the solution of the unperturbed Hamiltonian $H_0\psi^{st}_{qE} = E\psi^{st}_{qE}$ and is defined in both scattering and leads region and obtained using, for instance, the methods

[2] Kwant extensions website: https://kwant-project.org/extensions (accessed November 30th, 2018).

described in chapter 2. Substituting ψ_{qE}^{st} into the Schrödinger equation (5.4), one writes:

$$i\hbar\frac{\partial}{\partial t}\bar{\psi}_{qE}(t) = [H(t) - E]\,\bar{\psi}_{qE}(t) + Q_{qE}(t), \tag{5.28}$$

where $Q_{qE}(t)$ is a source term of the form:

$$Q_{qE}(t) = [H(t) - H_0]\,\psi_{qE}^{st} \tag{5.29}$$

It should be noted that the difference $H(t) - H_0$ results in a term that is only nonzero where the perturbation takes place. As a result, Eq. (5.28) is an equation only for the time-dependent correction term $\bar{\psi}_{qE}(t)$ with inital conditions $\psi_{qE}(t \leq 0) = 0$ and is defined in a finite region.

At this point, the Schrödinger equation is defined over a finite region in space and has a time-perturbation that can be located in the central region and in the center-leads interface. However, $H(t)$ still describes an open-system where translational invariant leads are effectively coupled via self-energies. When a perturbation is included in such system, it is expected that, at long times, it propagates in an outward direction conflicting with the leads that are modeled under stationary boundary conditions. The form that T-Kwant solve this problem [39] is by artificially including a complex self-energy $i\Sigma$, namely:

$$i\hbar\frac{\partial}{\partial t}\bar{\psi}_{qE}(t) = [H(t) - E - i\Sigma]\,\bar{\psi}_{qE}(t) + Q_{qE}(t) \tag{5.30}$$

where Σ is a scalar potential that is nonzero only in the leads region[3]. In order to minimize reflections, the absorbing potential Σ increases adabatically within a finite width towards the leads direction. Ref.[39] presents an analytical study of the spurious reflections for particular choices of Σ.

Finally, Eq. (5.30) can be solved using standard numerical techniques for differential equations, such as the Runge-Kutta methods[40]. After obtaining $\bar{\psi}_{qE}(t)$, the complete solution $\psi_{qE}(t)$ can be calculated by following Eq. (5.27).

[3] In practice, additional leads units cells are included to the central region where the absorbing potential Σ is placed. This is justified by the fact that $\Sigma(n)$ breaks translational invariance, thus, contributing to the scattering. Therefore, it should be taken into account as an extention to the scattering region.

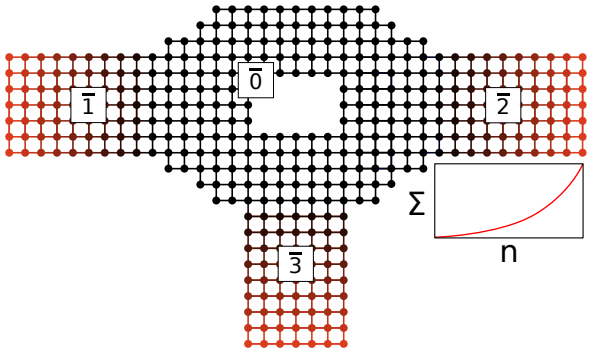

Fig. 5.1 Schematics of the absorbing potential intensity (red) for a system containing a central ring-shaped region $\bar{0}$ coupled to three leads $\bar{1},\bar{2},\bar{3}$. Inset: a typical curve $\Sigma(n)$, where n is the lead unit-cell. Adapted figure from Ref. [39].

5.2.2 The time-dependent local operators

If we try to directly solve the scattering eigenproblem in the time domain by using the strategy of the stationary eigenproblem described in Chapter 2, i.e. by partially projecting the eigenvectors over an energy-dependent eigenmode basis, we are faced with the problem of having to construct a four-dimensional scattering matrix $S_{pq}(E',E)$ with two continuous dependences in E and E', which is computationally inpractical. The way to proceed is to solve the Schrödinger differential equation with a source and a sink, Eq. (5.30), in a space-time basis and calculate the system scattering wave function $\psi_{qE}(t)$ for a certain initial conditions E and q. Once we have the wave function at hand, the related observables can be readly otained.

For instance, in the application of the following chapter, we are interested in the charge density $n_\alpha(i,t)$ relatedand local current $I_\alpha(i,j,t)$:

$$n_\alpha(i,t) = \sum_{q\in\alpha}\int \frac{dE}{2\pi} f_\alpha(E)|\psi_{qE}(i,t)|^2 \tag{5.31}$$

$$I_\alpha(i,j,t) = -2\mathrm{Im}\sum_{q\in\alpha}\int \frac{dE}{2\pi} f_\alpha(E)\psi^*_{qE}(i,t)H_{ij}(t)\psi_{qE}(j,t) \tag{5.32}$$

which are defined inside the scattering region (central region $\bar{0}$ of Fig.5.1). The function $\psi_{qE}(i,t)$ is the amplitude of the scattering wave function at the site i and $H_{ij}(t)$ is the hopping matrix between sites i and j. $f_\alpha(E)$ is the Fermi distribution of the lead α, in equilibrium with the electronic reservoir with chemical potential μ_α and temperature T, that contains the mode q at energy E. The thermal average integration covers the whole conduction band, but in practice is cut by f_α at the Fermi energy E_F. Generally, the lower energy modes cause slow perturbations that do not contribute to the physics and can be handled by a low

energy filtering "device". However, such device has to be developed specifically for the time-dependent problem being addressed. If correctly accounted, the energy integration range can be reduced to an effective window, which increases the speed of the method and allows for complex simulations. A particular filter is presented in the next chapter.

In one-dimension, the local current and charge density are related by a simple continuity equation $\frac{\partial J}{\partial x} = \frac{\partial \rho}{\partial t}$. In tight-binding approximation, it can be written as[4]:

$$\pm n_\alpha(i,t) = \int_0^t dt' I_\alpha(i, i \pm 1, t') \tag{5.33}$$

where the sign $\pm$ is determined by the current direction. The above equation is useful to determine the total amount of charge $Q = en$ passing through a cross-section in a certain time-interval [44].

There is an interesting and direct interpretation of the continuity equation, when the charge density varies in time and the current density has a compression or expansion component. When a finite perturbation is applied to a finite cavity, the perturbation relaxes to the stationary regime as $t \to \infty$. In a multiterminal setup, we can define:

$$N_\alpha = \sum_{i \in S_\alpha} n_\alpha(i, t \to \infty) \tag{5.34}$$

as the total number of particles that pass through S_α, a cross-sectioning point (1D), line (2D) or area (3D) defined next to the $\alpha-$lead. As a result, we obtain:

$$\sum_{\alpha=1}^{\Lambda} N_\alpha = 0. \tag{5.35}$$

It means that every charges that enters the system through a certain lead has to leave the system though any lead after a long time, demonstrating charge conservation. One can also observe that:

$$N_\alpha = \sum_\beta \int \frac{dE}{2\pi} f_\beta(E) N_\beta(E) \tag{5.36}$$

where $N_\beta(E)$ is the number of particles at energy E. Equation (5.36) is a generalization of the Landauer formula Eq. (4.20) in multiterminal setups to the time domain, as observed in Ref. [38][5].

[4] It should be mentioned that the current as defined in (5.32) carries a the stationary component. In practice, such contribution to the integral diverges and has to be subtracted manually.

[5] In case of a voltage pulse, the number $N_\beta(E)$ at the RHS of Eq. (5.36 can also be related to the voltage intensity $n = \frac{e}{h} \in V(t)dt$, as the RHS of the Landauer-Büttiker formula. e is the elementary charge.

5.2.3 Electron-electron interaction self-consistent algorithm

So far, we have discussed the one-body dynamical Schödinger equation. In this section, we present the main elements of the underlying theory to address electronic interactions in the time-dependent quantum transport using the scattering methods. The methods discussed here are part of the T-Kwant package, under the "manybody" suit and are detailed in the Refs. [47, 124]. To this end, we use the second-quantized basis of fermionic operators of particle creation $\hat{c}^{\dagger}_{i\sigma}$ and annihilation $\hat{c}_{j\sigma'}$ where:

$$\left\{\hat{c}_{i\sigma},\hat{c}^{\dagger}_{j\sigma'}\right\}=\delta_{ij}\delta_{\sigma\sigma'},\quad \left\{\hat{c}_{i\sigma},\hat{c}_{j\sigma'}\right\}=\left\{\hat{c}^{\dagger}_{i\sigma},\hat{c}^{\dagger}_{j\sigma'}\right\}=0 \tag{5.37}$$

where the spin structure $\sigma=\uparrow,\downarrow$ is explicitly considered.

In the above notation, we describe the time-dependent interacting Hamiltonian as:

$$\hat{H}(t)=\hat{H}_0+W(t)+\hat{H}_{int}. \tag{5.38}$$

The stationary Hamiltonian and the time-dependent perturbation become, respectively:

$$\hat{H}_0=\sum_{\langle i,j\rangle,\sigma}\gamma_{ij}\hat{c}^{\dagger}_{i\sigma}\hat{c}_{j\sigma}, \tag{5.39}$$

$$\hat{W}(t)=\sum_{\langle i\in S,j\in L\rangle,\sigma}W_{ij}(t)\hat{c}^{\dagger}_{i\sigma}\hat{c}_{j\sigma} \tag{5.40}$$

where γ_{ij} for $i\neq j$ denotes the nearest-neighbor hopping integrals[6] and $\hat{W}(t)$ describes a time-dependent perturbation at the system-lead interface. The interacting Hamiltonian is considered in the Hubbard form and reads:

$$\hat{H}_{int}=\sum_i U_i\left(\hat{c}^{\dagger}_{i\uparrow}\hat{c}_{i\uparrow}-n_0\right)\left(\hat{c}^{\dagger}_{i\downarrow}\hat{c}_{i\downarrow}-n_0\right) \tag{5.41}$$

where n_0 is the equilibrium occupation. The interacting term $\hat{H}_{int}$ is stationary and can, in principle, show a local dependence $U_i\rightarrow U(\mathbf{r}_i)$.

The many-body problem defined above can be slved within a mean-field approach[48]. We use the Hartree-Fock approximation. In this case, $\hat{H}_{int}$ transforms into a scalar potential that is a function of the mean of time-dependent fields, namely:

$$\hat{H}_{HF}(t)=\sum_i U_i\hat{c}^{\dagger}_i\hat{c}_i\left[\langle\hat{c}^{\dagger}_i(t)\hat{c}_i(t)\rangle-n_0\right] \tag{5.42}$$

[6]The notation for the hopping parameter in this section and in the following ones is γ and not t as previously done. This is due to the conflict with the time variable, named as t.

where the average of the number operator $\langle \hat{c}_i^\dagger(t)\hat{c}_i(t)\rangle$, written in the Heisenberg picture, is obtained from Eq. (5.31). The problem becomes effectively diagonal in spin σ. We, therefor, ignore the spin degree of freedom.

In the Hartree-Fock (HF) approximation, the particle moves freely under the influence of an external effective potential that depends on the charge density $n(i,t) = \langle \hat{c}_i^\dagger(t)\hat{c}_i(t)\rangle$. The onsite energy U_i is the energetic cost for doubly occupying the orbital i with electrons with opposite spins.

The calculation of $n(i,t)$ and the solution of the time-dependent Schrödinger equation with a scalar potential of the form (5.42) constitutes a set of self-consistent equations solved numerically using an adaptive scheme available in the T-KWANT package[39].

Chapter 6

Application: Proposal for a plasmon-plasmon collider to study Coulomb interactions

Coulomb interaction gives origin to striking features in the electronic dynamics in one-dimension[125–127]. It has been known that electrons confined to quasi-one-dimensional wires propagating with momentum conservation can behave as bosons[128]. In other words, the system degrees of freedom, basically consisting of collective excitation modes, can propagate with bosonic velocity, which is much faster than the fermionic velocity. In addition, the lack of coupling between the Coulomb field and the spin density causes spin-charge separation and fractional values of the elementary electronic charge, proportional to the bosonic velocity, are observed[126]. The bosonization process of a collection of fermions in 1D is known as a Luttinger liquid[129] and can only be detected through transient non-adiabatic effects after inducing local perturbations to 1D wires, such as voltage pulses.

In recent years, single-electron devices have been developed to improve the current understanding of the collective electronic excitations from different perspectives[124]. In particular, interferometers have been used to test quantum statistics of single particles, by sending two particles to a beam splitter and looking at arrival outputs. By changing the delay τ between the particles, the wave function interference can be measured and the particle nature is detected[120].

In this chapter, we propose a collider between two electronic states confined in quasi one-dimensional wires and generated by voltage pulses as a probe to study the Coulomb interaction. The model consists in sending two such states to a perpendicular collision guided by two crossing nanowires whose center is under an effective Coulomb mean field. By applying the pulses at the two inputs of the cross of wires and looking at the total

amount of charge released at the two outputs, we investigate the time-evolution of the pulses. Through local operators, such as current and local density, we compare the local quantities variations due to a relative time-delay τ between the pulses. We observe that the delay, which breaks the system symmetry, causes a current deviation that is maximal away from the synchronized collision, causing a dip around the center $\tau = 0$. An investigation in under progress to compare such results with previous studies of quantum interference in electron collision[130, 131].

6.1 Theoretical Background

In this section, we present a brief review of the Luttinger liquid theory of interating fermions in one dimenion. We present the general theory for uniform 1D chains and describe how the same result can be obtained in the case of a pulse propagation in an interacting wire, showing that the phenomenon can actually take place in the proposed model. Moreover, we describe the mesoscopic device were the collider can be realized.

6.1.1 The Luttinger liquid model for interacting fermions in 1D

Here, we present the physics of the Luttinger liquid starting from a model of 1D confined interacting fermions. We show that, under a few physics assumptions, one can derive collective excitations that behave as bosons.

Let us consider the Hamiltonian of electrons in a translational invariant 1D lattice within the nearest neighbor tight-binding approximation with a Hubbard interaction term[128]:

$$H = -\gamma \sum_{n,\sigma} \left(\psi^{\dagger}_{n,\sigma} \psi_{n+1,\sigma} + h.c. \right) + \varepsilon \sum_{n,\sigma} \psi^{\dagger}_{n\sigma} \psi_{n\sigma} + U \sum_{n} \rho_{n\uparrow} \rho_{n\downarrow} \tag{6.1}$$

where $\rho_{n\sigma} = \psi^{\dagger}_{n\sigma} \psi_{n\sigma}$ is the occupation number operator of electrons with spin σ at the site n. We note that the noninteracting Hamiltonian $U = 0$, which is diagonal in spin, commutes with the translation operator. Therefore, the free wave function can be written as $\psi_n = \psi_0 e^{ikna}$ with corresponding eigenenergy:

$$E(k) = \varepsilon - 2\gamma \cos ka. \tag{6.2}$$

At the Fermi surface of one-dimensional systems, the momentum is $k = \pm k_F$. We are interested in the problem in the vicinity of the Fermi level, where the dispersion relation can be linearized $E(k) \approx \hbar v_F k$. By considering $\varepsilon \to 2\gamma \cos k_F a$, the wave function around the

Fermi level can be written as the left and right moving components[110]:

$$\psi_{n\sigma} = e^{e^{ik_F na}}\psi^{+}_{n\sigma} + e^{e^{-ik_F na}}\psi^{-}_{n\sigma} \tag{6.3}$$

It is worth noting that the separation in direction components also separates the occupation number operator:

$$\rho_{n\sigma} = \rho^{+}_{n\sigma} + \rho^{-}_{n\sigma}. \tag{6.4}$$

We assumes that $\psi_{n\sigma}$ varies slowly over lengths comparable with the lattice parameter a. Therefore, the discrete derivative can be taken back from discretization, namely:

$$\psi^{\pm}_{n+1\sigma} = \psi^{\pm}_{n\sigma} + a\partial_x\psi^{\pm}_{n\sigma} + \mathscr{O}(a^2). \tag{6.5}$$

By substituting Eq. (6.5) into (6.1) and keeping only the linear terms in a, the free Hamiltonian becomes:

$$H_0 \approx -2at\gamma\sum_{n\sigma}\left\{\left[\psi^{+}_{n\sigma}\right]^{\dagger} i\partial_x\psi^{+}_{n\sigma} + \left[\psi^{-}_{n\sigma}\right]^{\dagger} i\partial_x\psi^{-}_{n\sigma}\right\}. \tag{6.6}$$

Taking the continuum limit $a \to 0$, the sum becomes an integral in space, namely, $a\sum_n \to \int_{-L/2}^{L/2} dx$. After a Fourier transformation, which gives $i\partial_x \to k$, the free Hamiltonian in momentum space is:

$$H_0 = -\hbar v_F\sum_{\sigma}\int kdk\left\{\left[\psi^{+}_{\sigma}(k)\right]^{\dagger}\psi^{+}_{\sigma}(k) + \left[\psi^{-}_{\sigma}(k)\right]^{\dagger}\psi^{-}_{\sigma}(k)\right\}. \tag{6.7}$$

where $v_F = \frac{1}{\hbar}\left.\frac{\partial E(k)}{k}\right|_{k_F} = 2a\gamma\hbar$ is the Fermi velocity. Eq. (6.7) describes a basis of left and right propagating modes of dispersion relation $E^{\pm}(k) = \pm\hbar v_F k$. However, in such basis, negative energy states are allowed and the description of right and left propagating modes is obscured. To circumvent this problem, the fermionic particle-hole operators are defined [129]:

$$\begin{aligned} \psi^{+}_{\sigma}(k) &= b_{k\sigma}, \quad \psi^{-}_{\sigma}(k) = c^{\dagger}_{k\sigma} \quad k \geq 0 \\ \psi^{+}_{\sigma}(k) &= c^{\dagger}_{k\sigma}, \quad \psi^{-}_{\sigma}(k) = b_{k\sigma} \quad k < 0. \end{aligned} \tag{6.8}$$

Substituting the operators (6.8) into the free Hamiltonian H_0, we obtain:

$$H_0 = \hbar v_F\sum_{\sigma}\int |k|dk\left\{b^{\dagger}_{k\sigma}b_{k\sigma} + c^{\dagger}_{k\sigma}c_{k\sigma}\right\} \tag{6.9}$$

Correspondingly, the Hubbard interacting Hamiltonian in momentum space is:

$$H_{int} = U \sum_{\sigma,s=\pm} \int dk \left\{ \rho^{s}_{\sigma}(k)\rho^{s}_{\bar{\sigma}}(-k) + \rho^{s}_{\sigma}(k)\rho^{-s}_{\bar{\sigma}}(-k) \right\} \tag{6.10}$$

where $\bar{\sigma} = -\sigma$ and:

$$\rho^{\pm}_{\sigma}(k) = \int dq \left[\psi^{\pm}_{\sigma}(k)\right]^{\dagger} \psi^{\pm}_{\sigma}(k) \tag{6.11}$$

is the density operator in momentum space, whose commutation relation reads[1]:

$$\left[\rho^{s}_{\sigma}(k), \rho^{s'}_{\sigma'}(k')\right] = -\delta_{\sigma,\sigma'}\delta_{s,s'}\delta(k-k') \tag{6.12}$$

Eq. (6.12) is a bosonic commutation relation.

The free Hamiltonian in the density operator basis becomes:

$$H_0 = \frac{v_F}{L} \sum_{s\sigma} \int dk \rho_{\sigma s}(k)\rho_{\sigma s}(-k) \tag{6.13}$$

Eqs. (6.13) and (6.10) constitute the complete description of the bosonization process of the Luttinger liquid. The diagonalization of the above Hamiltonian give us the bosonic velocity as the eigenvalues $E(k) = \hbar v_\rho k$, where:

$$v_\rho = v_F \sqrt{1 + \frac{aU}{2\pi\hbar v_F}}. \tag{6.14}$$

This suggests that these collective excitation given by $\rho^{s}_{\sigma}(k)$ have a velocity corresponding to the Fermi velocity v_F renormalized by a correction term proportional to the interaction intensity U.

We note that the velocity v_ρ could also be obtained from the model of a voltage pulse propagating in a 1D wire using the collisionless Boltzmann approach[76] where the relation between the Boltzmann distribution function and the charge density is given by:

$$\rho(\mathbf{r},t) = \sum_{\mathbf{k}} f(\mathbf{r},\mathbf{k},t). \tag{6.15}$$

In such model, the external forces of the Boltzmann equation are the Coulomb repulsion and the electric force due to the pulse potential $V(t)$.

[1] There is an omitted procedure here that is standard to remove divergence in momentum space caused by negative energy states. It is also responsible for defining a vacuum state in Dirac-like systems. See Ref. [132] for a detailed discussion.

The formalism introduced in this section can be extended to fermionic spin interactions, which lead to a renormalized spin velocity v_s[110]. As a result, one can demonstrate that the spin velocity differs from the charge density velocity $v_s \neq v_p$. This striking result has been achieved using time-dependent charge pulses in two-dimensional electron gas (2DEG) devices[125].

The 2DEG, formed at the interface of semiconductor heterostructures such as GaAs/AlGaAs, has been one of the most used systems to realize single-electron dynamics in solid states [119].

Fig. 6.1 describes a typical realization of a 2DEG. It shows the formation of a 2DEG at the junction of AlGaAs containing a wide gap, between the conduction and valence band, and a GaAs of a narrow gap. The junction between the two materials with such a difference of energy gaps causes a bend in both bands and, consequently a potential dip at the interface[8]. The resulting triangular well parallel to the junction interface (Fig. 6.1b) gives rise to quantized modes (Fig. 6.1c). Typically, E_F allows for a single occupied band corresponding to the ground state of the interface confining potential.

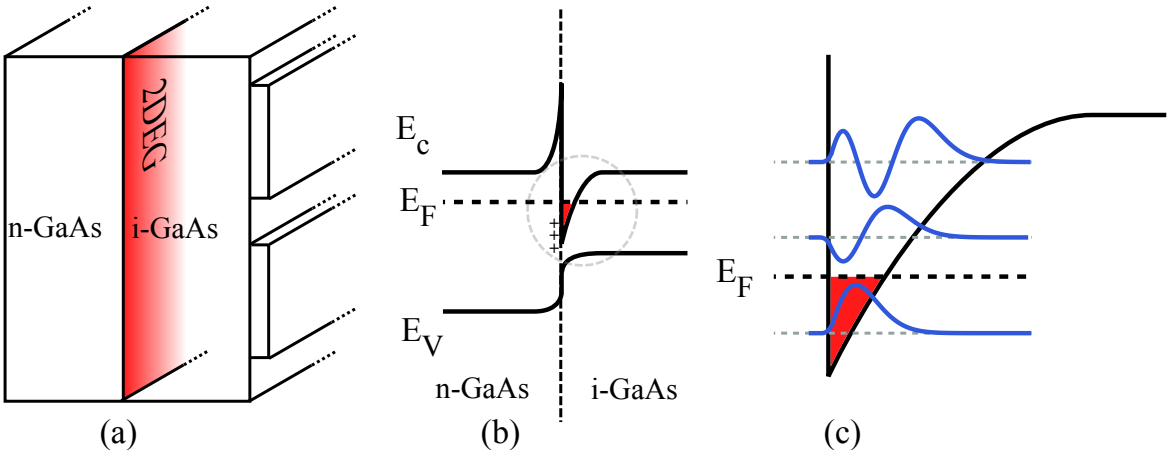

Fig. 6.1 (a) 2DEG formed a the interface of GaAs and GaAs. Metallic gates are represented by the blocks connected to the GaAs. (b) The contact between the two semiconductors generates an attractive potential at the right of the interface and a repulsive one at the left for a current of electrons, which causes confinement perpendicularly to the interface.(c) For a Fermi energy E_F close to the minimum of the attractive potential, only the ground state along this direction is allowed, characterizing the 2DEG system.

By introducing metallic gates to the system, one can further engineer the confining potential in the two-dimensional plane. Hence, one can make the electrons move along arbitrary geometries, such as 1D wires, quantum dots, cavities, etc. At the end, one obtains an experimental realization of a quasi one dimensional charge.

6.2 Motivations

This section is devoted to show the recent findings in Luttinger liquid realization through voltage pulses in 2DEG devices. A theoretical model was provided and demonstrated the plasmon velocity in numerical simulations[76]. Recently, an experimental reproduction of the liquid in a quasi one-dimensional wire was obtained [124], paving the way to several applications (see Ref. [119] and references therein). Therefore, a plasmon collider, consisting of two crossing quasi 1D wires, could be the step further to the understanding of the Coulomb interactions in such devices.

6.2.1 Theoretical evidence of plasmons in 1D wires

Despite the Luttinger liquid theory has been well-established [128], the experimental realization remained challenging for a while. The recent progress in transient nanoelectronic circuits has motivated the emergence of new models as proposals to the observation of liquid renormalized velocity.

An interesting theoretical model is discussed in Ref. [76], which consists in a quasi one-dimensional infinite wire in tight-binding approximation. Using an early stage version of the T-Kwant extension, the authors has been able to simulate a time-dependent voltage pulse of Gaussian shape propagating through the wire and to detect the pulse trajectory using local operators. By including electron-electron interaction in the central region of the wire, using the time-dependent Hartree-Fock approximation, the local operators were able to detect the increase in the velocity as predicted by the Luttinger liquid theory, Eq. (6.14) (see Fig. 6.2). The transient characteristic of the system was also observed through a decrease in the local current intensity.

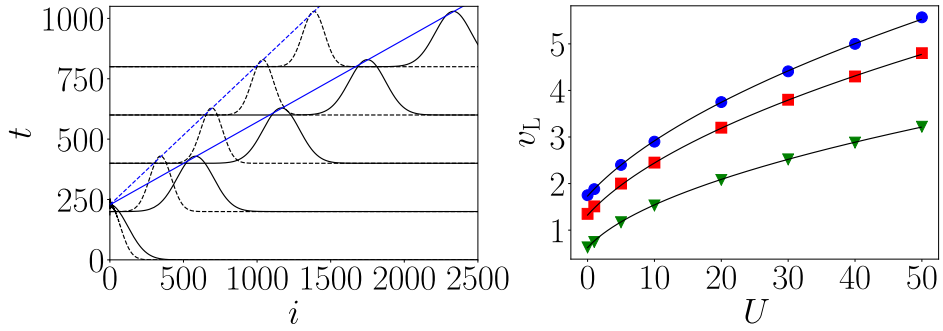

Fig. 6.2 Left panel: Charge density of the Gaussian shaped voltage pulse propagating through a 1D wire of length $L = 25000$ sites without (dashed line) and with (solid line) interaction. Figure from Ref. [47]. The slope of the line allows one to measure the propagating velocity $v = \frac{di}{dt}$. Right panel: the points are calculated propagating velocity as a function of the interaction intensity U of the simulations. The solid line is Eq. (6.14). Three different Fermi energies were considered and are represented by different symbols. Figure from Ref. [76].

6.2.2 Experimental evidence of plasmons in quasi-1D wires

In Ref. [124], a time-of-flight experiment using single-electron pulses was able to capture the plasmon velocity in quasi one-dimensional wire. By depositing metallic gates on top of a GaAs/AlGaAs heterostructure, a micrometer-scale wire could be tailored in a 2DEG device. Then, by applying a ultra-short voltage pulse to one of the contacts, several QPCs positioned along the wire could be able to measure the arrival time of the pulse at different places (see Fig. 6.3).

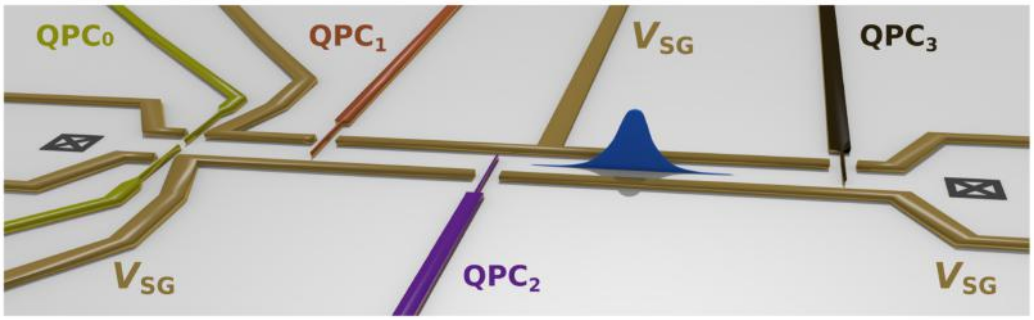

Fig. 6.3 Device used in Ref. [124] to detect the plasmon velocity in a quasi one wire. A voltage pulse is emitted from the left contact (box with a cross) and propagates to the right one. Different QPCs are used as fast switches to detect the passage of the pulse, except the QPC_0 which works as a channel filtering (see details in the text). Figure from Ref. [124].

The measurements of the arrival time at different positions allows one to calculate the pulse velocity. By changing the voltage on a side gate V_{SG}, the confinement is also changed and the arrival time of the pulse is shifted proportionally. Fig. 6.4 displays the pulse velocity

as a function of the side-gate potential obtained in Ref. [124]. It shows a comparison of the velocity measurements (symbols) with a parameter-free self-consistent numerical calculation (solid line) for a multi-channel Luttinger liquid [133]. The multi-channel theory was used in this case due to the experimental limitations, a pure one-dimensional wire could not be achieved. Nevertheless, a mode filtering QPC_0 was used to select the charge population of the energy channels of the wire, which allowed for a comparison of the result for different numbers of open channels (see detailed discussion in Ref. [124]).

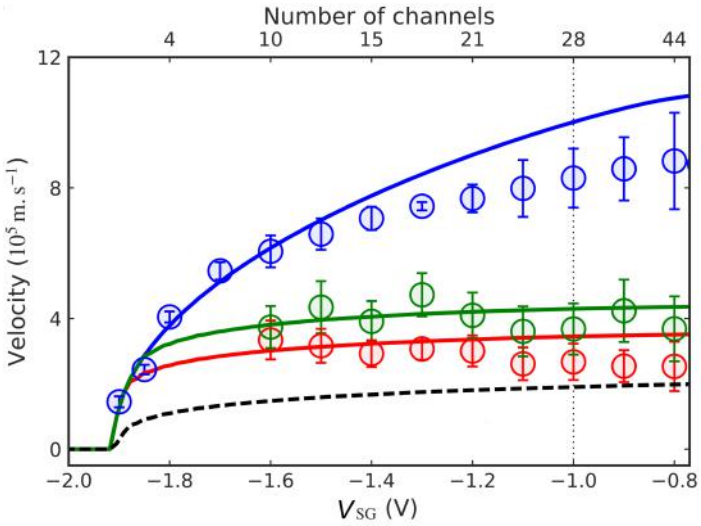

Fig. 6.4 Velocity of the voltage pulse as a function of a confinement potential V_{SG} in the wire. The symbols are experimental measurements of the velocity and the colors represent different number of open channels after the filtering QPC_0. The blue data correspond to the case where the filtering is turned off. The green and the red data are results for the two and one open channel, respectively. The curves are numerical results obtained from a multi-channel Luttinger liquid theory [133]. A dashed line represents the noninteracting case. Figure from Ref. [124].

6.3 The model

Here, we describe the model used to numerically calculate the perpendicular collision between two interacting voltage-pulses.

The system consist of two conducting quasi-one-dimensional wires of length L and width W in a cross geometry, see Fig. 6.5.

The Hamiltonian can be written in three parts:

$$\hat{H}(t) = \hat{H}_0 + \hat{H}_p(t) + \hat{H}_{int}(t), \tag{6.16}$$

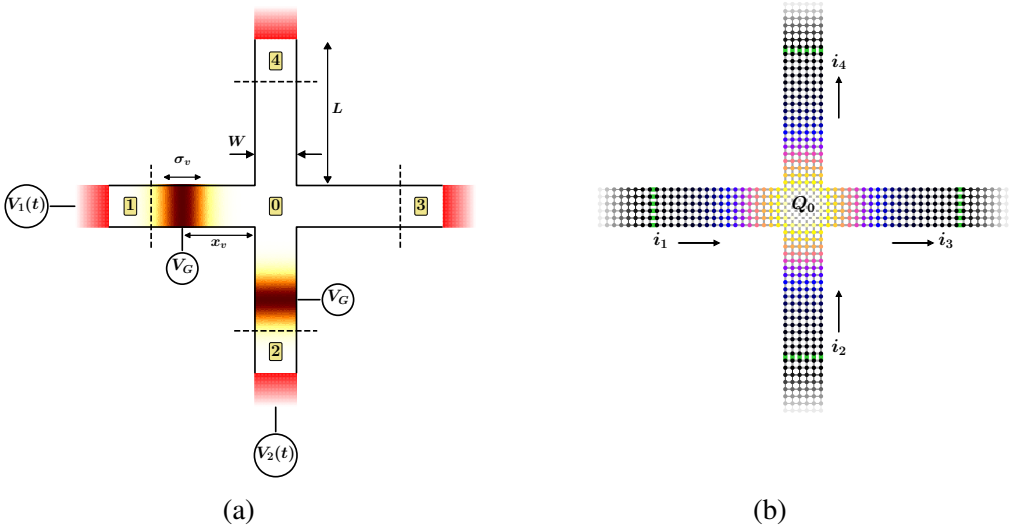

(a) (b)

Fig. 6.5 Sketch of the collider model: a crossing geometry of two quasi-one-dimensional wires. The numbered tags indicate the notation adopted in the text. Local currents are calculated at the dashed lines $1,2,3,4$ and the local density is calculated in the area 0 limited by the lines. The heat-map indicates the voltage intensity V_G of the QPC filtering. The parameters x_v and σ_v are position and width of the slope-shaped QPCs. Voltage pulses $V(t)$ are injected in the entries 1 and 2 and collected in the outputs 3 and 4. (b) Currents i_n at terminals $n = 1,2,3,4$ indicating the direction of pulse propagation. Charge conservation is verified when $\sum_n \int_0^t dt' i_n(t') = Q_0(t)$. Color-map of Fig. (b): intensity the interacting field U_i.

where $\hat{H}_0 = \sum_{\langle i,j\rangle\sigma} \gamma_{ij} \hat{c}^\dagger_{i\sigma} \hat{c}_{j\sigma}$ is the Hamiltonian of the unperturbed system in tight-binding approximation and γ is the nearest neighbor hopping parameter.

The time-dependent perturbation $\hat{H}_p(t) = \sum_{\langle i,j\rangle} W_p(t) \hat{c}^\dagger_i \hat{c}_j$ corresponds to two homogeneous voltage biases. Each one is a pulse of Gaussian shape in time $W_p(t) = eV_p e^{-4\log 2(t-t_0)^2/\sigma_v}$ of initial time t_0, width σ_v and amplitude V_p. The perturbations $W_p(t)$ and are applied at the system-lead interfaces 1 and 2 sufficiently far from the central region.

The interacting term $\hat{H}_{int}(t) \sum_i \mathbf{U}(\mathbf{r}_i) \hat{c}^\dagger_i \hat{c}_i \left(\langle \hat{c}^\dagger_i \hat{c}_i \rangle - n_0 \right)$ comprehends to a self-consistent Hartree potential of local dependence $U(\mathbf{r}_i)$ (see section 5.2.3). The time-dependent Schrödinger equation is solved numerically using the Tkwant package, discussed in the previous chapter, from where the time-evolved wave-function $\Psi_{\alpha,E}(i,t)$ due to a pulse injection in channel α at energy E is calculated.

We are interested in the observable quantities that can be expressed in terms of time-evolved wave-function. As described in section 5.2.2, the charge density and local current observables, respectively $n_\alpha(i,t)$ and $I_\alpha(i,j,t)$, demand a numerical integration in energy. Moreover, the collider demands the pulses to be at a sufficiently fast velocity to propagate

almost straightforwardly to the opposite output wires. To this end, we included QPCs with a slope shape to work as a mode filtering for the undesired energy intervals of the pulses, similarly to the one used in the experiment of Ref. [124]. Numerically, the QPC filtering is also an efficient way to remove the excitations around the bottom of the band that are extremely slowly and eventually get stuck in the scattering region, causing numerical divergences. Experimentally, such situation does not impose a considerable problem, as the contacts are at a sufficiently high Fermi energy and the contribution from the modes that get stuck are negligible [38]. As a result, the integration is performed only for the fastest modes, which increases the speed of the method.

6.4 Results and Discussions

The results can be separated in three main stages. Firstly, we perform a set of DC calculations using the Kwant package and justify the choices of the QPC filtering parameters. Secondly, calculations using the T-Kwant without interaction allow us to discuss the charge conservation in the system. Finally, we perform time-dependent collision within the interacting system using the T-Kwant package and present our main findings.

6.4.1 Building the collider: focusing of electron current in DC

We analyzed the DC characteristics of the system, by calculating the scattering matrix elements S_{mn} using the tools available in the Kwant package and discussed in chapter 2. The conductance from wire a to wire$b$ is calculated using the Landauer formula:

$$G_{\alpha\beta} = \frac{2e^2}{h} \sum_{n\in\alpha, m\in\beta} |S_{nm}|^2. \tag{6.17}$$

The calculated conductances from wire $\alpha = 1$ in a 4-terminal setup containing 10 sites in the transversal direction are displayed in Fig. 6.6 as a function of the QPC filtering voltage and for the Fermi energy $E_F = 1\gamma$. For this energy, there 6 conducting channels, which gives the maximum conductance of $12e^2/h$ observed in the figure. As the potential increases, we observe that both the conductance from wire 1 to wires 2 and 4 vanish. The only nonzero conductances are respectively G_{11}, which is proportional to the reflection probability, and G_{13}. A filtering at $V_G = 1.8\gamma$ is enough to obtain a transmission probability that is mainly G_{13}. In the time-resolved case, such result works as a guide to the time-dependent flow, as at long times, the system has to converge to a stationary configuration[44].

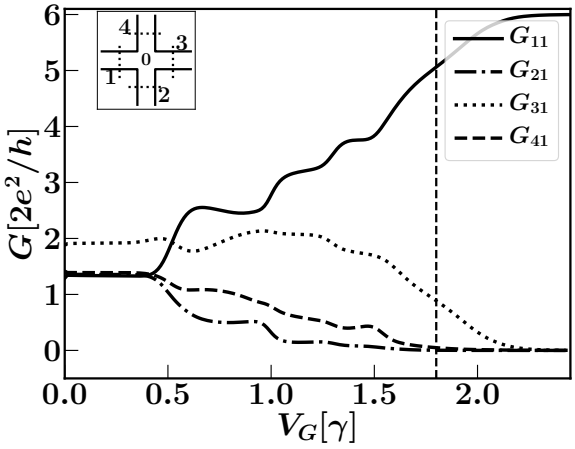

Fig. 6.6 Conductances from wire 1 to 2 (G_{12}), 3 (G_{13}) and 4 (G_{14}) and reflection (G_{11}) as a function of the QPC gate voltage V_G at the Fermi energy $E_F = 2.0\gamma$. The vertical dashed line indicates the chosen voltage value $V_G = 1.8\gamma$ used in the time dependent simulations.

The stationary local current for the ground state in wire 1 at Fermi energy 2γ and $V_G = 1.8\gamma$ is displayed in Fig. 6.7). The local current profile also exhibits almost straightforward propagation. A calculation of the local current at cross-sectioning lines close to the wires ending give us the percentage of about 96% of the current localized in the wire 3. We also observe that the presence of the QPC causes subtle oscillations in the transverse direction in the current and such perturbation should also be expected in the time-resolved case.

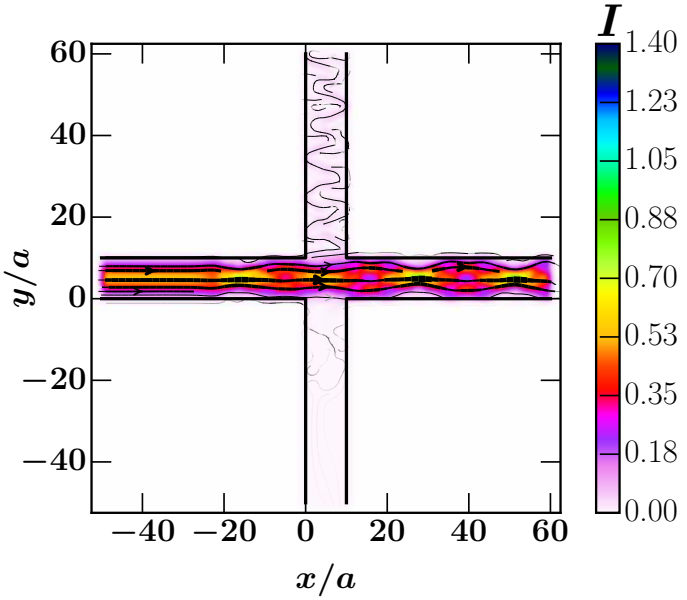

Fig. 6.7 Local current vector field due to a mode injection in lead 1 channel 1 at energy $E_F = 2.0\gamma$.

6.4.2 Verification of charge conservation

Let us now examine the time-dependent simulations of the pulse propagation without interaction. Such analysis is useful to verify for charge conservation.

We consider that the local currents $I_\alpha(i,i+1,t)$ are calculated from a cross sectioning line of sites in the wire α (see Fig. 6.5b). In the central region denoted by $\alpha = 0$, which is the region encompassed by the cross sectioning lines of α, only the local charge density $n_0(t)$ is calculated. From the local operators, we calculate the accumulated charge per time:

$$Q_\alpha^{(b)}(t) = \sum_{i\in\alpha} \int_0^{t'} dt' I_\alpha^{(b)}(i,i+1,t') \tag{6.18}$$

$$Q_0^{(b)}(t) = \sum_{i\in 0} n_0^{(b)}(i,t) \tag{6.19}$$

where $\alpha = 1,2,3,4$ stands for the wire and $b = 1,2,12$ is a label that represents a pulse injected in wire 1, 2 or in both 1 and 2, respectively.

We observe the trajectory of the voltage pulses injected into the system in all the cases $b = 1,2,12$. For a Fermi velocity of $v_F = 2a\gamma$ the pulse takes the time $\Delta t = (2L+W)/2a\gamma + 20/\gamma$ to cross the system completely. In units of the pulse width τ_p, the simulation time is let running until the maximum time of $t_{max} = 25\tau_p$ is reached, which is enough for any accumulated charge to be released from the system. Therefore, we verified that (figure not shown):

$$\sum_{\alpha=0}^{4} Q_\alpha^{(b)}(t) = 0, \qquad \sum_{\alpha=1}^{4} Q_\alpha^{(b)}(t\to\infty) = 0 \tag{6.20}$$

which is the expected result from charge conservation. While the left result is a consequence of the numerical precision of the Runge-Kutta integration, the right result is equivalent to Eq. 5.35, where $N_\alpha = Q_\alpha(t\to\infty)$. Using the quantities $Q_\alpha^{(b)}(t\to\infty)$, from now on just $Q_\alpha^{(b)}(\infty)$, we calculate the current deviations due to the presence of interaction.

6.4.3 The interacting collision between delayed pulses

Let us now discuss the results of the collision of the voltage pulses. Fig. 6.4.3 displays snapshots of the simulation that are obtained with $Q_0^{(b)}(t)$ calculated from the charge density operator. It shows a synchronized collision between the voltage pulses without (upper panels) and with (lower panels) interaction Time is displayed in units of the pulse duration τ_p. We note that, despite the effect is visualy subtle, a change in the density dsitribution along the time evolution can be observed.

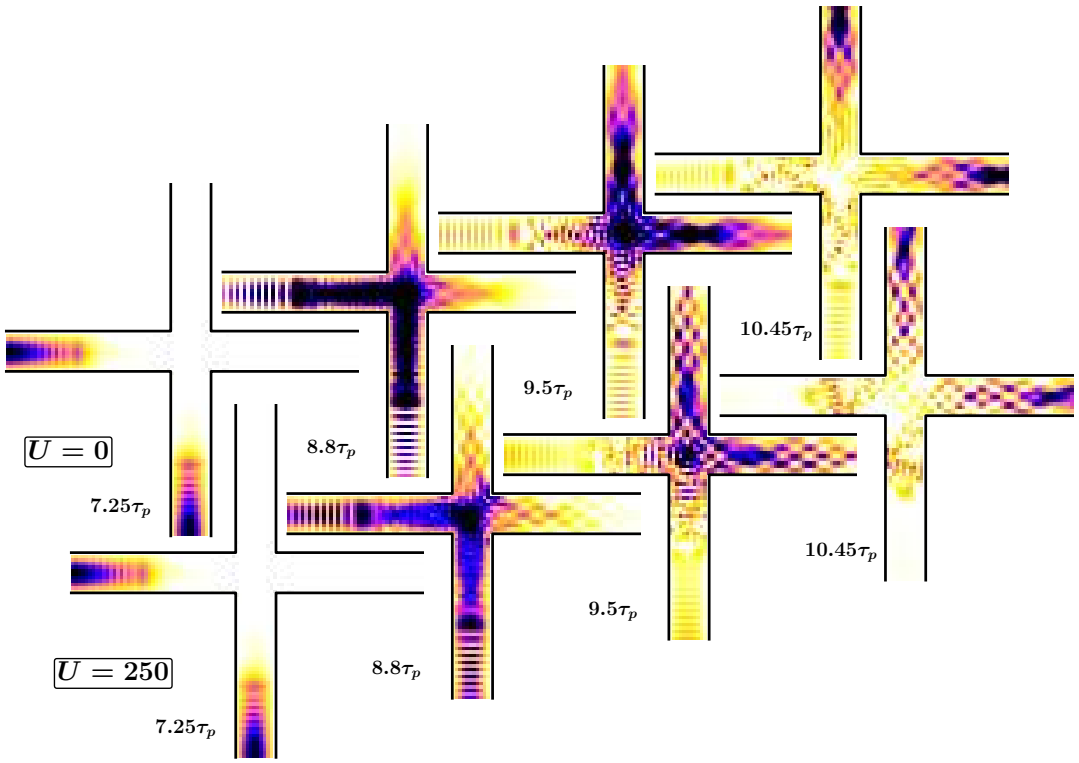

Fig. 6.8 Snapshots of the synchronized collision between the voltage pulses in the non-interacting (upper) and interacting case (lower) at different simulation times (from left to right).

To quantify the effect in detail, we examine the accumulated charges at long times $Q_\alpha^{(b)}(\infty)$ that release the system through the wires $\alpha = 3,4$ after the pulses propagation in a interacting system. The interaction intensity $U(\mathbf{r}_i)$ increases smoothly and reaches the maximal value at the central region of the cross (see Fig. 6.5b). It is modeled by a sum of smooth step-shaped functions:

$$U(x,y) = \frac{U}{4}\left[\tanh\left(\frac{x-x_L}{d_x}\right) - \tanh\left(\frac{x-x_R}{d_x}\right)\right]\left[\tanh\left(\frac{y-y_B}{d_y}\right) + \tanh\left(\frac{y-y_T}{d_y}\right)\right] \tag{6.21}$$

where x_L, x_R, y_B, y_T are the effective limits of the interacting region and $d_x = d_y = d$ defines the smoothness of the step.

We add a delay between the pulses $V_1(t-\tau_d) = V_2(t)$ of width τ_p injected in wires 1 and 2. Figure 6.9 shows the values of $Q_\alpha^{(b)}(\infty)$ through the wires 3 and 4 for different interaction intensities U as a function of the delay τ_d. Without interaction ($U = 0$), the charge in both wires are independent of the delay. As the interaction increases, one observes that (i) the

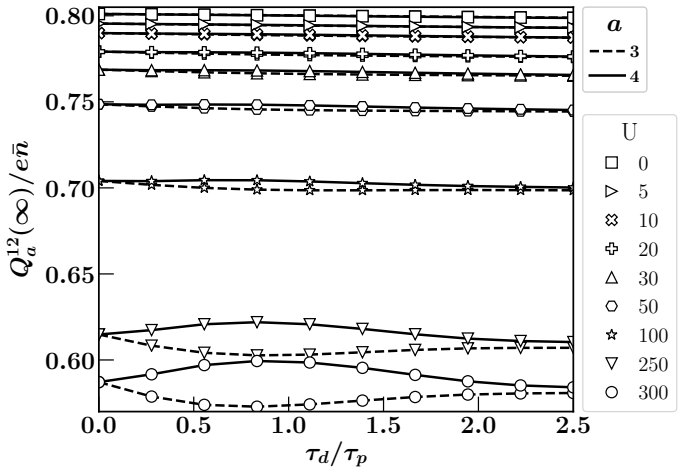

Fig. 6.9 Accumulated charge at long times (equivalent to the charges at $t \to \infty$) that passsed through the wires 3 (dashed) and 4 (solid) as a function of the delay time and for different interaction intensities.

charge flux is being deviated to the wire 4 and out the wire 3 as the delay is increased; (ii) the charge is decreasing proportionally to the interaction intensity.

About the charge deviation, we note that it is maximal at the time delay $\tau_d = \tau_p$, that is to say, when the first pulse has already passed over. After the maximum value is reached, the difference between the charges in the wires 3 and 4 starts to decrease until, at some point, the pulses become too far from each other to interact. This is an evidence that Coulomb interaction has been successfully probed in this model for a plasmon-plasmon collider.

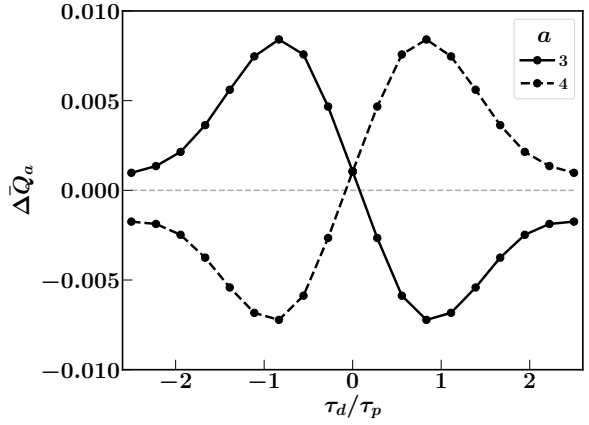

Fig. 6.10 Deviated charge according to Eq. (6.22) that passed through the wires 3 and 4.

In order to observe the detailed effects of Coulomb interaction in the deviated charge, we look at the accumulated charges in a different way: we observed the ratio between the

charges at the outputs by the inputs in the case $b = 12$ and subtract the respective ratio of the sum of the charges for the cases $b = 1, 2$, namely:

$$\Delta\bar{Q}_a = \frac{Q_a^{12}}{Q_1^{12} + Q_2^{12}} - \frac{Q_a^1 + Q_a^2}{Q_1^1 + Q_2^1 + Q_1^2 + Q_2^2}. \tag{6.22}$$

which should result in a more symmetric data. This quantity is also supposed to converge to zero at long delay times.

In Figure 6.10, we see that $\Delta\bar{Q}_a$ converges slowly to zero as $t \to \infty$. We also observe that the charge at wire 3 for positive values of delay equals the charge at wire 4 for the negative values as a result of the system symmetry.

We also note that there is a small positive amount of charge during the synchronous collision, which means that $Q_a^{12}(0) > Q_a^1(0) + Q_a^2(0)$, i.e., the interacting charges during the collision are increased in relation to the noninteracting ones. Also, the most effective collision-response has been observed after the first pulse has already passed over, which could be an evidence electron statistics[119].

6.5 Conclusions

In this chapter, we presented a proposal for a plasmon-plasmon collider in quasi one dimensional wires. To this end, we have reviewed the Luttinger liquid theory in one dimension. We have also discussed the Luttinger liquid realization in voltage pulses propagating in quasi 1D wires on top of a 2DEG and discussed experimental findings.

Our proposed model for a collider is based on a $4-$terminals setup and consists in sending two voltage pulses to a perpendicular collision guided by two crossing nanowires containing a few transversal sites. The first stage of this study is based of stationary results of current direction for particles propagating on a discrete square lattice. The second stage consist in checks for charge conservation. Finally, the center of the cross is then subjected to an effective Coulomb mean field modeled by a smooth step function that is nonzero at the center. We demonstrated that, by inducing voltage pulses with a relative time-delay τ, local operators allow us to quantify the total amount of charge deviated as a function of interaction intensity. We observed that the current deviation due to interactions is maximal away from the synchronized collision, causing a dip around the center $\tau = 0$.

Chapter 7

Final remarks

In this thesis, we study, implement, and use numerical methods to investigate the electronic quantum properties for a variety of systems. In particular, we use the Kwant package based on the wave function matching (WFM) method. We demonstrated its efficiency on the calculations of the scattering matrix and scattering wave function on constructing a sparse linear system which is an optimized situation for the sparse solvers.

We have reviewed the underlying theory of the (WFM) method applied to a tight-binding (finite element) Hamiltonian used to model the transport properties of mesoscopic systems. Our analysis revealed that such implementation of the WFM method is computationally far superior than previously expected [21]: (i) Kwant is practically insensitive to the coordination number of the lattice model and it (ii) has a linear scaling with the number of sites in the leads, representing a huge advantage over RGF. We numerically verify our predictions in a number of settings, by benchmarking the CPU time, memory usage and precision of the WFM versus the RGF method.

As a first application of the WFM method in Kwant, we discussed the problem of weak localization corrections in the magneto-conductance of a graphene nanoribbon, coupled to metallic leads. We consider two kinds of disorder, onsite and hopping integral disorder. The former has been shown to cause the crossover between the weak-localization and the weak anti-localization regime as a function of the correlation length of the disorder. The latter causes a suppression to the weak localization correction, as a evidence of the pseudomagnetic field effect generated by the strain.

Additionally, we discussed the effects of the application of an external in-plane magnetic field on the ripples of the model to probe effects of graphene deformations in the weak localization curve. We also study in-plane relaxation mechanisms in graphene considering the interaction with a substrate. The in-plane relaxation accounts for realistic deformations in graphene surfaces. We expect that the inclusion of in-plane deformations makes rippled

graphene samples to be affected by perpendicular magnetic field and also account for more precise pseudomagnetic field contributions. In some situations, the pseudomagnetic field could be overestimated in the absence of in-plane relaxations in highly sloped regions of the surface. This could be a drawback to the modeling of highly sensible quantities extracted from strained surfaces such as the weak localization. Finally, we study the dependence of the tail of the weak localization profile with the extent of a magnetic field that smoothly decays into the leads region as. This study is under progress.

Next, we numerically calculate the longitudinal and transverse resistances of disordered graphene sheet in the quantum Hall regime. By considering a realistic-sized graphene sample patterned in the Hall bar geometry, corresponding to a multi-terminal setting, we perform conductance matrix calculations, which is a difficult task for other numerical approaches. We considered two kinds of disorder, scalar and chiral, in the short-range and in the long-range limit, and discussed the corresponding effect in the resistivity and conductivity tensor. We observed that the long-range disorder effect is much smaller than the short-range ones, specially regarding the $n = 0$ LL in graphene. We also observed the complete localization $\sigma_{xx} = \sigma_{xy} = 0$ of the $n = 0$ level when only long-range hopping disorder is present, which is a different picture for the other types of disordered considered here. Such results contradicts theoretical predictions in the literature [95], where a transition to the standard QH regime was not observed. A subtle protuberance, which could be a sign of level-splitting is observed, but the effect is too small to be conclusive and an investigation is required.

By performing thermal averages in the conductance matrix, we observed the temperature dependence of the $\rho_{xx} \times \rho_{xy}$ diagrams for each type of disorder. We showed that while both the short-range and the long-range onsite disorder the longitudinal resistivity peak at $n = 0$ increase with temperature, the short-range hopping disorder decreases. In the long-range disorder case, we observed a divergence with temperature in the $n = 0$ LL. For the $n \neq 0$ case, the temperature dependence is equivalent for all observed disorder types.

In the second part of this thesis, we studied time-dependent methods of the scattering problem under the tight-binding approximation and develop an application. The methods are implemented in the T-Kwant package, the time-dependent extension of the Kwant package. We discussed an extension of the wave function matching formalism to the time-domain upon a time-dependent perturbation. Next, we reviewed the T-Kwant methods discussed in the literature and presented the main formalism behind the time-dependent interacting scattering problem using the time-dependent Hartree-Fock approximation, which is also available in the package.

The last chapter is devoted to a final application in this thesis, a proposal for a plasmon-plasmon collider in quasi one dimensional wires. We reviewed the Luttinger liquid theory in

one dimension and discussed the liquid realization in voltage pulses propagating in quasi 1D wires on top of a 2DEG. Te proposed model for a collider is based on a $4-$terminals setup and consists in sending two voltage pulses to a perpendicular collision guided by two crossing nanowires of small width. The center of the cross is subjected to an effective Coulomb mean field. We demonstrated that, by inducing voltage pulses with a relative time-delay τ between the pulses at two perpendicular inputs of the cross, through local operators, we quantified the total amount of charge deviated through Coulomb interactions. We observed that the current deviation due to interactions is maximal away from the synchronized collision, causing a dip around the center $\tau = 0$. Such scheme could be realized experimentally in 2DEG and the result could be compared to experiments of quantum interference of electronic collision.

References

[1] K. S. Novoselov, A. K. Geim, S. V. Morozov, D. Jiang, Y. Zhang, S. Dubonos, I. Grigorieva, A. Firsov, Electric Field Effect in Atomically Thin Carbon Films, Science 306 (2004) 666.

[2] H. Liu, A. T. Neal, Z. Zhu, Z. Luo, X. Xu, D. Tománek, P. D. Ye, Phosphorene: an unexplored 2d semiconductor with a high hole mobility, ACS Nano 8 (4) (2014) 4033–4041.

[3] Q. H. Wang, K. Kalantar-Zadeh, A. Kis, J. N. Coleman, M. S. Strano, Electronics and optoelectronics of two-dimensional transition metal dichalcogenides, Nature Nanotechnology 7 (11) (2012) 699.

[4] A. H. Castro Neto, F. Guinea, N. M. R. Peres, K. S. Novoselov, A. K. Geim, The electronic properties of graphene, Rev. Mod. Phys. 81 (March) (2009) 109.

[5] A. K. Geim, I. V. Grigorieva, Van der waals heterostructures, Nature 499 (7459) (2013) 419.

[6] S. Z. Butler, S. M. Hollen, L. Cao, Y. Cui, J. A. Gupta, H. R. Gutiérrez, T. F. Heinz, S. S. Hong, J. Huang, A. F. Ismach, et al., Progress, challenges, and opportunities in two-dimensional materials beyond graphene, ACS nano 7 (4) (2013) 2898–2926.

[7] M. Xu, T. Liang, M. Shi, H. Chen, Graphene-like two-dimensional materials, Chemical reviews 113 (5) (2013) 3766–3798.

[8] S. Datta, Electronic Transport in Mesoscopic Systems, Cambridge University Press, Cambridge, 1995.

[9] N. Ashcroft, N. Mermin, Solid State Physics, Saunders College, Philadelphia, 1976.

[10] L. Lima, A. Dusko, C. Lewenkopf, Efficient method for computing the electronic transport properties of a multiterminal system, Phys. Rev. B 97 (16) (2018) 165405.

[11] K. Kazymyrenko, X. Waintal, Knitting algorithm for calculating Green functions in quantum systems, Phys. Rev. B 77 (11) (2008) 115119.

[12] C. H. Lewenkopf, E. R. Mucciolo, The recursive Green's function method for graphene, J. Comput. Electron. 12 (2013) 203.

[13] P. A. Khomyakov, G. Brocks, V. Karpan, M. Zwierzycki, P. J. Kelly, Conductance calculations for quantum wires and interfaces: Mode matching and Green's functions, Phys. Rev. B 72 (3) (2005) 1–13.

[14] D. S. Fisher, P. A. Lee, Relation between conductivity and transmission matrix, Phys. Rev. B 23 (12) (1981) 6851–6854.

[15] A. Hernández, V. M. Apel, F. A. Pinheiro, C. H. Lewenkopf, Quantum electronic transport: Linear and nonlinear conductance from the Keldysh approach, Physica A 385 (1) (2007) 148–160.

[16] S. Sadasivam, M. K. Y. Chan, P. Darancet, Theory of thermal relaxation of electrons in semiconductors, Phys. Rev. Lett. 119 (2017) 136602.

[17] A. R. Rocha, V. M. Garcia-Suarez, S. W. Bailey, C. J. Lambert, J. Ferrer, S. Sanvito, Towards molecular spintronics, Nat. Mater. 4 (4) (2005) 335.

[18] A. Kuzmin, M. Luisier, O. Schenk, Fast methods for computing selected elements of the Green's function in massively parallel nanoelectronic device simulations, in: European Conference on Parallel Processing, Springer, 2013, pp. 533–544.

[19] J. Eckel, F. Heidrich-Meisner, S. Jakobs, M. Thorwart, M. Pletyukhov, R. Egger, Comparative study of theoretical methods for non-equilibrium quantum transport, New J. Phys. 12 (4) (2010) 043042.

[20] M. Brandbyge, J.-L. Mozos, P. Ordejón, J. Taylor, K. Stokbro, Density-functional method for nonequilibrium electron transport, Phys. Rev. B 65 (2002) 165401.

[21] C. W. Groth, M. Wimmer, A. R. Akhmerov, X. Waintal, Kwant: a software package for quantum transport, New J. Phys. 16 (6) (2014) 63065.

[22] Z. Fan, A. Uppstu, T. Siro, A. Harju, Efficient linear-scaling quantum transport calculations on graphics processing units and applications on electron transport in graphene, Comput. Phys. Commun. 185 (1) (2014) 28–39.

[23] S. Birner, T. Zibold, T. Andlauer, T. Kubis, M. Sabathil, A. Trellakis, P. Vogl, Nextnano: general purpose 3-d simulations, IEEE Trans. Electron. 54 (9) (2007) 2137–2142.

[24] A. Smogunov, A. Dal Corso, E. Tosatti, Ballistic conductance of magnetic Co and Ni nanowires with ultrasoft pseudopotentials, Phys. Rev. B 70 (2004) 045417.

[25] R. Korol, M. Kilgour, D. Segal, Probezt: Simulation of transport coefficients of molecular electronic junctions under environmental effects using büttiker's probes, Comput. Phys. Commun. 224 (2018) 396–404.

[26] D. Jacob, J. J. Palacios, Critical comparison of electrode models in density functional theory based quantum transport calculations, J. Chem. Phys. 134 (4) (2011) 044118.

[27] S. Li, W. Wu, E. Darve, A fast algorithm for sparse matrix computations related to inversion, Comput. Phys. Commun. 242 (2013) 915–945.

[28] F. Triozon, S. Roche, Efficient linear scaling method for computing the landauer-büttiker conductance, Eur. Phys. J. B 46 (3) (2005) 427–431.

[29] T. Ozaki, K. Nishio, H. Kino, Efficient implementation of the nonequilibrium Green function method for electronic transport calculations, Phys. Rev. B 81 (2010) 035116.

[30] S. Bruzzone, G. Iannaccone, N. Marzari, G. Fiori, An open-source multiscale framework for the simulation of nanoscale devices, IEEE Trans. Electron. 61 (1) (2014) 48–53.

[31] M.-H. Liu, K. Richter, Efficient quantum transport simulation for bulk graphene heterojunctions, Phys. Rev. B 86 (2012) 115455.

[32] N. Papior, N. Lorente, T. Frederiksen, A. García, M. Brandbyge, Improvements on non-equilibrium and transport Green function techniques: The next-generation transiesta, Comput. Phys. Commun. 212 (2017) 8–24.

[33] J. E. Fonseca, T. Kubis, M. Povolotskyi, B. Novakovic, A. Ajoy, G. Hegde, H. Ilatikhameneh, Z. Jiang, P. Sengupta, Y. Tan, G. Klimeck, Efficient and realistic device modeling from atomic detail to the nanoscale, J. Comput. Electron. 12 (4) (2013) 592–600.

[34] G. Kiršanskas, J. N. Pedersen, O. Karlström, M. Leijnse, A. Wacker, Qmeq 1.0: An open-source python package for calculations of transport through quantum dot devices, Comput. Phys. Commun. 221 (2017) 317–342.

[35] Z. Ren, R. Venugopal, S. Goasguen, S. Datta, M. S. Lundstrom, nanoMOS 2.5: A two-dimensional simulator for quantum transport in double-gate MOSFETs, IEEE Trans. Electron. 50 (9) (2003) 1914–1925.

[36] P. R. Amestoy, I. S. Duff, J.-Y. L'Excellent, J. Koster, A fully asynchronous multifrontal solver using distributed dynamic scheduling, SIAM J. Matrix Anal. Appl. 23 (1) (2001) 15–41.

[37] M. Wimmer, Quantum transport in nanostructures: From computational concepts to spintronics in graphene and magnetic tunnel junctions, Ph.D. thesis, University of Regensburg (2009).

[38] B. Gaury, J. Weston, M. Santin, M. Houzet, C. Groth, X. Waintal, Numerical simulations of time-resolved quantum electronics, Phys. Rep. 534 (1) (2014) 1–37.

[39] J. Weston, X. Waintal, Linear-scaling source-sink algorithm for simulating time-resolved quantum transport and superconductivity, Physical Review B 93 (13) (2016) 134506.

[40] J. Weston, X. Waintal, Towards realistic time-resolved simulations of quantum devices, Journal of Computational Electronics 15 (4) (2016) 1148–1157.

[41] J. Weston, Numerical methods for time-resolved quantum nanoelectronics, Springer, 2017.

[42] O. Shevtsov, X. Waintal, Numerical toolkit for electronic quantum transport at finite frequency, Physical Review B 87 (8) (2013) 085304.

[43] B. Rossignol, T. Kloss, P. Armagnat, X. Waintal, Toward flying qubit spectroscopy, Physical Review B 98 (20) (2018) 205302.

[44] B. Gaury, X. Waintal, Dynamical control of interference using voltage pulses in the quantum regime, Nature communications 5 (2014) 3844.

[45] T. Bautze, C. Süssmeier, S. Takada, C. Groth, T. Meunier, M. Yamamoto, S. Tarucha, X. Waintal, C. Bäuerle, Theoretical, numerical, and experimental study of a flying qubit electronic interferometer, Physical Review B 89 (12) (2014) 125432.

[46] B. Gaury, J. Weston, X. Waintal, The ac josephson effect without superconductivity, Nature communications 6 (2015) 6524.

[47] T. Kloss, J. Weston, X. Waintal, Transient and sharvin resistances of luttinger liquids, Physical Review B 97 (16) (2018) 165134.

[48] G. Stefanucci, R. Van Leeuwen, Nonequilibrium many-body theory of quantum systems: a modern introduction, Cambridge University Press, 2013.

[49] T. Ando, Quantum point contacts in magnetic fields, Phys. Rev. B 44 (1991) 8017–8027.

[50] P. A. Mello, N. Kumar, Quantum Transport in Mesoscopic Systems, Oxford University Press, Oxford, 2004.

[51] J. Taylor, H. Guo, J. Wang, Ab initio modeling of quantum transport properties of molecular electronic devices, Phys. Rev. B 63 (2001) 245407.

[52] S.-H. Ke, H. U. Baranger, W. Yang, Electron transport through molecules: Self-consistent and non-self-consistent approaches, Phys. Rev. B 70 (2004) 085410.

[53] D. J. Thouless, S. Kirkpatrick, Conductivity of the disordered linear chain, J. Phys. C: Solid State Phys. 14 (1981) 235–245.

[54] A. MacKinnon, The calculation of transport properties and density of states of disordered solids, Z. Phys. B 385 (4) (1985) 385.

[55] M. Wimmer, K. Richter, Optimal block-tridiagonalization of matrices for coherent charge transport, J. Comp. Phys. 228 (23) (2009) 8548 – 8565.

[56] S. Cauley, M. Luisier, V. Balakrishnan, G. Klimeck, C.-K. Koh, Distributed non-equilibrium Green's function algorithms for the simulation of nanoelectronic devices with scattering, J. Appl. Phys. 110 (4) (2011) 043713.

[57] H. U. Baranger, A. D. Stone, D. P. DiVincenzo, Resistance fluctuations in multiprobe microstructures: Length dependence and nonlocality, Phys. Rev. B 37 (11) (1988) 6521–6524.

[58] S. Rotter, J.-Z. Tang, L. Wirtz, J. Trost, J. Burgdörfer, Modular recursive green's function method for ballistic quantum transport, Phys. Rev. B 62 (2000) 1950–1960.

[59] F. Libisch, S. Rotter, J. Burgdörfer, Coherent transport through graphene nanoribbons in the presence of edge disorder, New J. Phys. 14 (12) (2012) 123006.

[60] S. R. Power, M. R. Thomsen, A.-P. Jauho, T. G. Pedersen, Electron trajectories and magnetotransport in nanopatterned graphene under commensurability conditions, Phys. Rev. B 96 (2017) 075425.

[61] C. Mahaux, H. A. Weidenmüller, Shell-model approach to nuclear reactions, North-Holland Pub. Co., Amsterdam, 1969.

[62] M. Di Ventra, Electrical Transport in Nanoscale Systems, Cambridge University Press, Cambridge, 2008.

[63] G. H. Golub, C. F. V. Loan, Matrix Computations, 3rd Edition, JHU Press, Baltimore, 1996.

[64] I. Rungger, S. Sanvito, Algorithm for the construction of self-energies for electronic transport calculations based on singularity elimination and singular value decomposition, Phys. Rev. B 78 (3) (2008) 035407.

[65] E. Anderson, Z. Bai, J. Dongarra, A. Greenbaum, A. McKenney, J. Du Croz, S. Hammarling, J. Demmel, C. Bischof, D. Sorensen, Lapack: A portable linear algebra library for high-performance computers, in: Proceedings of the 1990 ACM/IEEE Conference on Supercomputing, Supercomputing '90, IEEE Computer Society Press, Los Alamitos, CA, USA, 1990, pp. 2–11.

[66] E. Anderson, Z. Bai, C. Bischof, S. Blackford, J. Demmel, J. Dongarra, J. Du Croz, A. Greenbaum, S. Hammarling, A. McKenney, D. Sorensen, LAPACK Users' Guide, 3rd Edition, Society for Industrial and Applied Mathematics, Philadelphia, PA, 1999.

[67] M. Zwierzycki, P. A. Khomyakov, A. A. Starikov, K. Xia, M. Talanana, P. X. Xu, V. M. Karpan, I. Marushchenko, I. Turek, G. E. Bauer, G. Brocks, P. J. Kelly, Calculating scattering matrices by wave function matching, Phys. Status Solidi B 245 (4) (2008) 623–640.

[68] D. K. Ferry, S. M. Goodnick, Transport in Nanostructures, Cambridge University Press, Cambridge, 1997.

[69] A. Calzolari, N. Marzari, I. Souza, M. Buongiorno Nardelli, Ab initio transport properties of nanostructures from maximally localized wannier functions, Phys. Rev. B 69 (2004) 035108.

[70] L. R. F. Lima, C. H. Lewenkopf, Disorder-assisted transmission due to charge puddles in monolayer graphene: Transmission enhancement and local currents, Phys. Rev. B 93 (2016) 045404.

[71] N. J. G. Couto, D. Costanzo, S. Engels, D.-K. Ki, K. Watanabe, T. Taniguchi, C. Stampfer, F. Guinea, A. F. Morpurgo, Random Strain Fluctuations as Dominant Disorder Source for High-Quality On-Substrate Graphene Devices, Phys. Rev. X 4 (2014) 041019.

[72] R. Burgos, J. Warnes, L. R. Lima, C. Lewenkopf, Effects of a random gauge field on the conductivity of graphene sheets with disordered ripples, Physical Review B 91 (11) (2015) 115403.

[73] E. McCann, K. Kechedzhi, V. I. Fal'ko, H. Suzuura, T. Ando, B. Altshuler, Weak-localization magnetoresistance and valley symmetry in graphene, Physical Review Letters 97 (14) (2006) 146805.

[74] E. R. Mucciolo, C. H. Lewenkopf, Disorder and electronic transport in graphene, Journal of Physics: Condensed Matter 22 (27) (2010) 273201.

[75] A. P. Hinz, S. Kettemann, E. R. Mucciolo, Quantum corrections to thermopower and conductivity in graphene, Physical Review B 89 (7) (2014) 075411.

[76] J. Kłos, I. Zozoulenko, Effect of short-and long-range scattering on the conductivity of graphene: Boltzmann approach vs tight-binding calculations, Physical Review B 82 (8) (2010) 081414.

[77] T. Ihn, Semiconductor Nanostructures: Quantum states and electronic transport, Oxford University Press, 2010.

[78] H. Bruus, K. Flensberg, Many-body quantum theory in condensed matter physics: an introduction, Oxford university press, 2004.

[79] P. M. Ostrovsky, I. V. Gornyi, A. D. Mirlin, Electron transport in disordered graphene, Phys. Rev. B 74 (23) (2006) 235443.

[80] B. Altshuler, A. Aronov, Zero bias anomaly in tunnel resistance and electron-electron interaction, Solid State Communications 30 (3) (1979) 115–117.

[81] S. Hikami, A. I. Larkin, Y. Nagaoka, Spin-orbit interaction and magnetoresistance in the two dimensional random system, Progress of Theoretical Physics 63 (2) (1980) 707–710.

[82] D. Huertas-Hernando, F. Guinea, A. Brataas, Spin relaxation times in disordered graphene, The European Physical Journal Special Topics 148 (1) (2007) 177–181.

[83] A. Rycerz, J. Tworzydło, C. W. J. Beenakker, Anomalously large conductance fluctuations in weakly disordered graphene, EPL (Europhysics Letters) 79 (5) (2007) 57003.

[84] M. B. Lundeberg, J. A. Folk, Rippled graphene in an in-plane magnetic field: effects of a random vector potential, Physical review letters 105 (14) (2010) 146804.

[85] N. H. Shon, T. Ando, Quantum transport in two-dimensional graphite system, Journal of the Physical Society of Japan 67 (7) (1998) 2421–2429.

[86] V. M. Pereira, A. C. Neto, N. Peres, Tight-binding approach to uniaxial strain in graphene, Physical Review B 80 (4) (2009) 045401.

[87] F. Guinea, B. Horovitz, P. Le Doussal, Gauge field induced by ripples in graphene, Physical Review B 77 (20) (2008) 205421.

[88] H. Suzuura, T. Ando, Phonons and electron-phonon scattering in carbon nanotubes, Physical review B 65 (23) (2002) 235412.

[89] R. P. Feynman, R. B. Leighton, M. Sands, Lectures on physics, vol. iii (1965).

[90] D. Bahamon, Z. Qi, H. S. Park, V. M. Pereira, D. K. Campbell, Graphene kirigami as a platform for stretchable and tunable quantum dot arrays, Physical Review B 93 (23) (2016) 235408.

[91] H. Schomerus, Effective contact model for transport through weakly-doped graphene, Physical Review B 76 (4) (2007) 045433.

[92] Y. Zhang, Y.-W. Tan, H. L. Stormer, P. Kim, Experimental observation of the quantum hall effect and berry's phase in graphene, nature 438 (7065) (2005) 201.

[93] K. S. Novoselov, A. K. Geim, S. Morozov, D. Jiang, M. Katsnelson, I. Grigorieva, S. Dubonos, A. Firsov, Two-dimensional gas of massless dirac fermions in graphene, nature 438 (7065) (2005) 197.

[94] K. S. Novoselov, E. McCann, S. Morozov, V. I. Fal'ko, M. Katsnelson, U. Zeitler, D. Jiang, F. Schedin, A. Geim, Unconventional quantum hall effect and berry's phase of 2π in bilayer graphene, Nature physics 2 (3) (2006) 177.

[95] P. Ostrovsky, I. Gornyi, A. Mirlin, Theory of anomalous quantum hall effects in graphene, Physical Review B 77 (19) (2008) 195430.

[96] D. A. Abanin, K. S. Novoselov, U. Zeitler, P. A. Lee, A. K. Geim, L. S. Levitov, Dissipative quantum hall effect in graphene near the dirac point, Physical review letters 98 (19) (2007) 196806.

[97] Z. Jiang, Y. Zhang, H. Stormer, P. Kim, Quantum hall states near the charge-neutral dirac point in graphene, Physical Review Letters 99 (10) (2007) 106802.

[98] Y. Zhang, Z. Jiang, J. Small, M. Purewal, Y.-W. Tan, M. Fazlollahi, J. Chudow, J. Jaszczak, H. Stormer, P. Kim, Landau-level splitting in graphene in high magnetic fields, Physical review letters 96 (13) (2006) 136806.

[99] R. E. Prange, S. M. Girvin, The quantum hall effect, graduate texts in contemporary physics, Springer New York, 2nd ed. edn., doi 10 (1987) 978–1.

[100] T. Vojta, Quantum phase transitions in electronic systems, Annalen der Physik 9 (6) (2000) 403–440.

[101] F. Evers, A. D. Mirlin, Anderson transitions, Reviews of Modern Physics 80 (4) (2008) 1355.

[102] A. Pruisken, Universal singularities in the integral quantum hall effect, Physical review letters 61 (11) (1988) 1297.

[103] D. Thouless, Maximum metallic resistance in thin wires, Physical Review Letters 39 (18) (1977) 1167.

[104] B. Huckestein, Scaling theory of the integer quantum hall effect, Reviews of Modern Physics 67 (2) (1995) 357.

[105] H. Wei, D. Tsui, M. Paalanen, A. Pruisken, Scaling of the integral quantum hall effect, in: High magnetic fields in semiconductor Physics, Springer, 1987, pp. 11–15.

[106] K. Olsen, H. Limseth, C. Lütken, Universality of modular symmetries in two-dimensional magnetotransport, Physical Review B 97 (4) (2018) 045113.

[107] J. D. Jackson, Classical electrodynamics, 3rd Edition, Wiley, New York, NY, 1999.

[108] M. O. Goerbig, Electronic properties of graphene in a strong magnetic field, Rev. Mod. Phys. 83 (December) (2011) 1193.

[109] R. Shankar, Principles of quantum mechanics, Springer Science & Business Media, 2012.

[110] P. Phillips, Advanced solid state physics, Cambridge University Press, 2012.

[111] M. Koshino, T. Ando, Splitting of the quantum hall transition in disordered graphenes, Physical Review B 75 (3) (2007) 033412.

[112] T. Ando, Theory of electronic states and transport in carbon nanotubes, Journal of the Physical Society of Japan 74 (3) (2005) 777–817.

[113] B. Jeckelmann, B. Jeanneret, The quantum hall effect as an electrical resistance standard, Reports on Progress in Physics 64 (12) (2001) 1603.

[114] H. U. Baranger, A. D. Stone, Electrical linear-response theory in an arbitrary magnetic field: A new Fermi-surface formation, Phys. Rev. B 40 (1989) 8169–8193.

[115] O. Shevtsov, P. Carmier, C. Petitjean, C. Groth, D. Carpentier, X. Waintal, Graphene-based heterojunction between two topological insulators, Physical Review X 2 (3) (2012) 031004.

[116] K. S. Novoselov, Z. Jiang, Y. Zhang, S. Morozov, H. L. Stormer, U. Zeitler, J. Maan, G. Boebinger, P. Kim, A. K. Geim, Room-temperature quantum hall effect in graphene, Science 315 (5817) (2007) 1379–1379.

[117] A. Hernández, F. Pinheiro, C. Lewenkopf, E. Mucciolo, Adiabatic charge pumping through quantum dots in the coulomb blockade regime, Physical Review B 80 (11) (2009) 115311.

[118] K. Ando, Dynamical generation of spin currents, Semiconductor Science and Technology 29 (4) (2014) 043002.

[119] C. Bäuerle, D. C. Glattli, T. Meunier, F. Portier, P. Roche, P. Roulleau, S. Takada, X. Waintal, Coherent control of single electrons: a review of current progress, Reports on Progress in Physics 81 (5) (2018) 056503.

[120] E. Bocquillon, V. Freulon, J.-M. Berroir, P. Degiovanni, B. Plaçais, A. Cavanna, Y. Jin, G. Fève, Coherence and indistinguishability of single electrons emitted by independent sources, Science (2013) 1232572.

[121] C. Beenakker, H. van Houten, Quantum transport in semiconductor nanostructures, in: Solid State Physics, Vol. 44, Elsevier, 1991, pp. 1–228.

[122] H. Haug, A.-P. Jauho, Quantum kinetics in transport and optics of semiconductors, Vol. 2, Springer, 2008.

[123] M. V. Moskalets, Scattering matrix approach to non-stationary quantum transport, World Scientific, 2012.

[124] G. Roussely, E. Arrighi, G. Georgiou, S. Takada, M. Schalk, M. Urdampilleta, A. Ludwig, A. D. Wieck, P. Armagnat, T. Kloss, et al., Unveiling the bosonic nature of an ultrashort few-electron pulse, Nature communications 9.

[125] O. Auslaender, H. Steinberg, A. Yacoby, Y. Tserkovnyak, B. Halperin, K. Baldwin, L. Pfeiffer, K. West, Spin-charge separation and localization in one dimension, Science 308 (5718) (2005) 88–92.

[126] H. Steinberg, G. Barak, A. Yacoby, L. N. Pfeiffer, K. W. West, B. I. Halperin, K. Le Hur, Charge fractionalization in quantum wires, Nature Physics 4 (2) (2008) 116.

[127] V. V. Deshpande, M. Bockrath, L. I. Glazman, A. Yacoby, Electron liquids and solids in one dimension, Nature 464 (7286) (2010) 209.

[128] T. Giamarchi, Quantum physics in one dimension, volume 121 of international series of monographs on physics (2003).

[129] J. Luttinger, Jm luttinger, phys. rev. 119, 1153 (1960)., Phys. Rev. 119 (1960) 1153.

[130] R. Liu, B. Odom, Y. Yamamoto, S. Tarucha, Quantum interference in electron collision, Nature 391 (6664) (1998) 263.

[131] S. Ol'Khovskaya, J. Splettstoesser, M. Moskalets, M. Büttiker, Shot noise of a mesoscopic two-particle collider, Physical Review Letters 101 (16) (2008) 166802.

[132] W. Greiner, Quantum electrodynamics of strong fields, in: Hadrons and Heavy Ions, Springer, 1985, pp. 95–226.

[133] K. Matveev, L. Glazman, Coulomb blockade of tunneling into a quasi-one-dimensional wire, Physical review letters 70 (7) (1993) 990.